Stony Brook University

OFFICIAL COPY

The official electronic file of this thesis or dissertation is maintained by the University Libraries on behalf of The Graduate School at Stony Brook University.

© All Rights Reserved by Author.

Modeling and Experimental Study of Wafer Manufacturing and Machining Processes

A Dissertation Presented

by

Chunhui Chung

to

The Graduate School

in Partial Fulfillment of the

Requirements

for the Degree of

Doctor of Philosophy

in

Mechanical Engineering

Stony Brook University

August 2010

Copyright by

Chunhui Chung

2010

Stony Brook University

The Graduate School

Chunhui Chung

We, the dissertation committee for the above candidate for the
Doctor of Philosophy degree,
hereby recommend acceptance of this dissertation.

Dr. Imin Kao - Dissertation Advisor, Mechanical Engineering

Dr. Robert Kukta - Chairperson of Defense, Mechanical Engineering

Dr. Chad S. Korach, Mechanical Engineering

Dr. Lei Zuo, Mechanical Engineering

Dr. Teng-fong Wong, Geosciences

Dr. Michael Dudley, Materials Science and Engineering

This dissertation is accepted by the Graduate School

Lawrence Martin
Dean of the Graduate School

Abstract of the Dissertation

Modeling and Experimental Study of Wafer Manufacturing and Machining Processes

by

Chunhui Chung

Doctor of Philosophy

in

Mechanical Engineering

Stony Brook University

2010

To achieve the stringent requirements for the future specification of wafers, the progress in wafering processes such as slicing, lapping, grinding, and polishing is critical. The improvement of the existing technology and the innovation of advanced machining tools are necessary for the future wafer production. For example, study of vibration of a moving wire in slurry wiresaws and active control of such vibration can reduce kerf loss, and in turn reduce the cost of wafer manufacturing. Such study can also contribute to a better surface finish with less subsurface damages. Mixed abrasives in slurry can increase material removal rate in lapping to reduce time of machining and cost. In this dissertation, the research on the vibration of the wire in the slurry wiresaw system, mixed abrasive effect in lapping process, and wafer surface finishing by CNT brush are studied. Both free and forced vibration response of damped axially moving wire are derived by modal analysis and the Green's function, respectively. The eigensolutions, orthogonality, frequency of damped vibration, and frequency response with a point excitation are also obtained. Two different sizes of abrasives, F-400 and F-600 SiC, are mixed with different ratios in the slurry for lapping process. The results show that mixed abrasive grits can enhance the ma-

terial removal rate. However, the surface roughness becomes slightly worse. CNT brush is introduced as a new polishing tool. Preliminary experimental results are presented.

To my Parents

Table of Contents

List of Figures xi

List of Tables xvi

Acknowledgments xvii

1 Introduction 1

1.1 Wafer Manufacturing Processes and Surface Topography 2

1.1.1 Wafer manufacturing processes 2

1.1.2 Wafer geometry and surface characteristics 4

1.2 Literature Review and Challenges 5

1.2.1 Vibration response of axially moving wire in slurry wiresaw system 5

1.2.2 Mixed abrasive effect in lapping process 7

1.2.3 Wafer surface finishing by CNT brush 7

1.3 Outlines and Contribution of the Chapters 8

2 Free Vibration Response of Damped Axially Moving Wire 10

2.1 Introduction 10

2.2 Equation of Motion of Damped Axially Moving Wire 12

2.3 Solution of the Eigenvalue Problem of a Moving Wire in a Damped System 16

2.3.1 Eigenvalue problem 16

2.3.2 Adjoint eigenvalue problem 21
2.4 Orthogonal Relationship of the Eigenfunctions 22
2.4.1 Summary and comparison 24
2.5 Free Vibration Response 25
2.5.1 Analytical solution 26
2.5.2 Examples 27
2.6 Discussion 30
2.6.1 Comparison with special cases 30
2.7 Summary 32

3 Characteristics of Damped Axially Moving Wire of Slurry Wiresaw System 34

3.1 Introduction 34
3.2 Analysis of Damped Vibration 35
3.2.1 Damping ratio defined by frequency of vibration 35
3.2.2 Damping ratio defined by the complex eigenvalues 37
3.2.3 Comparison of ζ_ω and ζ_θ 38
3.2.4 Physical and apparent damping 41
3.3 Mode Shape and n^{th} Component of Response 45
3.3.1 Mode shape 45
3.3.2 The nth response as a function of the speed 45
3.4 Relevance to Slurry Wiresaw Systems 49
3.4.1 Reynolds number and drag force in wiresaw systems 49
3.4.2 Practical parameter study 52
3.4.3 Damping ratios 54
3.5 Summary 55

4 Green's Function and Forced Vibration Response of Damped Axially Moving Wire 59
4.1 Introduction 59
4.2 Green's Function 60
4.3 The Standard Form of Equations 64
4.4 Frequency Response with Point Excitation 68
4.4.1 Frequency response by the Green's function 68
4.4.2 Frequency response by the flexible influence function 69
4.5 Summary 72

5 Effect of Mixed Abrasive Grits in Lapping Process 73
5.1 Introduction 74
5.2 Experimental Setup 76
5.3 Results and Analysis 77
5.3.1 Material removal depth 77
5.3.2 Angular velocity of the jig 78
5.3.3 Surface roughness 80
5.3.4 Surface morphology 81
5.4 Surface Roughness Model for Mixed Abrasive Lapping[1] 81
5.5 Discussion 90
5.5.1 Loading versus material removal rate 91
5.5.2 Loading versus surface roughness 93
5.5.3 Material removal rate versus surface roughness 95
5.6 Summary 97

[1] This section is contributed by Professor Chad S. Korach [26] in the Department of Mechanical Engineering, State University of New York at Stony Brook.

6 Wafer Surface Polishing by Carbon Nanotube Brush 99
6.1 Ductile-Regime Machining 99
6.2 Experimental Setup 100
6.2.1 Fabrication of CNT brush 100
6.2.2 Experimental devices 100
6.3 Results of Experiments 102
6.3.1 Polished silicon wafer 102
6.3.2 Lapped silicon wafer 102
6.3.3 Lithium niobate 107
6.4 Discussions 107
6.5 Summary 110

7 Conclusions and Future Work 112
7.1 Vibration Response of the Wire in Slurry Wiresaw System 112
7.1.1 Conclusion 112
7.1.2 Future work 113
7.2 Effect of Mixed Abrasive Grits in Lapping Process 116
7.2.1 Conclusion 116
7.2.2 Future work 116
7.3 Wafer Surface Finishing by Carbon Nanotube Brush 117
7.3.1 Conclusion 117
7.3.2 Future work 117

Bibliography 118

Appendix

A Derivation of the Coefficients in Equations (2.46) and (2.47) in Free Vibration Response 127

B Closed-Form Solution of Equation (4.26) 130

C Nomenclature for Chapters 2, 3, and 4 131

D Nomenclature for Chapter 5 134

List of Figures

1.1 Folw chart of wafer manufacturing 3

1.2 Classification of topographical features based on their spatial wavelengths. The order of amplitude of each feature is also illustrated [1]. 4

1.3 Schematics of wiresaw slicing and definition of directions 6

2.1 Schematic of wiresaw system. The transverse and longitudinal directions are defined and shown. 13

2.2 Differential element of wire. 14

2.3 Free vibration response of a damped moving wire with $\eta = 1$ and $v = 0.3$. The components n is from 1 to 30, with an initial displacement shown at $(t = 0)$ 28

2.4 Free vibration response of a damped moving wire with $\eta = 1$ and $v = 0.3$. The components n is from 1 to 10, with an initial displacement shown at $(t = 0)$ 29

2.5 Free vibration response of undamped axially moving wire at $v = 0.3$ and $\eta = 0$. The component n is from 1 to 10. 31

2.6 Free vibration response of a stationary wire at $\eta = 1$. The component n is from 1 to 10. 33

3.1 Complex eigenvalue and the definition of damping ratio on the complex plane. The complex conjugate of the eigenvalue is not shown in the figure. . 38

3.2 Damping ratio ζ_ω and ζ_θ (solid and dashed curves) as a function of v for the first component of response ($u_1(x,t)$ with $n=1$). The damping factors are (a) $\eta=4$ and (b) $\eta=10$ 39
3.3 Apparent damping effect of free vibration response at $x = 0.5$(center of span) with $\eta = 1$, initial displacement $\sin \pi x$, and no initial velocity (that is, initially at rest). 40
3.4 damping ratio as a function of damping factor, η. 42
3.5 (a) Free vibration response of the entire wire span ($0 \le x \le 1$) with different damping factors $\eta = 0.5$ and $\eta = 2.0$. The nondimensionalized speed of wire v is kept at 0.3. The component n is from 1 to 10. (b) The continuous vibration responses at the middle of the wire ($x = 0.5$) are plotted for $\eta = 0.5$ and $\eta = 2.0$. As expected, the exponentially decaying envelop, $\mathrm{e}^{-\frac{\eta}{2}t}$, reduces faster with larger η value. The two responses have nearly identical frequencies of vibration. 43
3.6 (a) Free vibration response of the entire wire span ($0 \le x \le 1$) with different velocities $v = 0.1$ and $v = 0.7$. The nondimensionalized damping factor η is kept at 1. The component n is from 1 to 10. At $v = 0.1$, a full cycle is elasped from $t = 0 \sim 2$ seconds. On the other hand, only half cycle is elapsed for $v = 0.7$ during the same time period. (b) The reduction of amplitude of vibration for $v = 0.7$ is due to a slower frequency of vibration, as illustrated in (a). 44
3.7 Mode shapes of real (real line) and imaginary (dashed line) modes of first three modes. 46
3.8 The variation of first three components of response with initial displacement $\sin(\pi x)$, initial velocity 0, and damping factor $\eta = 1$. 50
3.9 The variation of first three components of response with initial displacement $\sin(2\pi x)$, initial velocity 0, and damping factor $\eta = 1$. 50

3.10 The variation of first three components of response with initial displacement $\sin(3\pi x)$, initial velocity 0, and damping factor $\eta = 1$. 51
3.11 Wire motion in slurry with transverse velocity, V_{tr} 52
3.12 Free vibration response with initial displacement $0.01 \sin \pi x$ and different damping factors $\eta = 1.728,\ 2\pi,$ and 28.57. The nondimensionalized velocity v is kept at 0.0306. The component n is from 1 to 10. The response at the middle of the wire becomes non-oscillatory when the damping factor $\eta \geq 2\pi$. 53
3.13 Damping ratios as functions of η_d with respective to the axially moving speed of wire in slurry wiresaw system. 55
3.14 Damping ratios as functions of η_d with respective to the tension of wire in slurry wiresaw system. 56
3.15 Damping ratios as functions of η_d with respective to the length of wire in slurry wiresaw system. 56
3.16 Damping ratios as functions of η_d with respective to the mass density of wire in slurry wiresaw system. 57

4.1 Plot of free vibration response in equation of a damped moving wire in equation (4.26) with $\eta = 1$ and $v = 0.3$. The initial displacement is $u(x, 0) = 0.01 \sin \pi x$, and the initial velocity is zero. 67
4.2 Schematic of wiresaw with point excitation 68
4.3 Absolute value of frequency response at $x = 0.25$ with point excitation at $a = 0.5$ and dimensionless velocity $v = 0.3$, which are obtained from (a) equation (4.28) and (b) equation (4.34). 70

5.1 Logitech PM5 lapping machine, employed to conduct experiments in this study. 76

5.2 Depth of the material removal with (a) 2.3-kg and (b) 4.1-kg loadings in lapping. 78
5.3 Angular velocity of jig with the (a) 2.3-kg and (b) 4.1-kg loadings during lapping. 79
5.4 Average RMS surface roughness after lapping. The unit is in micron. 80
5.5 Typical surface morphology of lapped wafer surface. The scale bar is $20\ \mu\mathrm{m}$. 82
5.6 Normalized linear distributions for FEPA F-400 and F-600 SiC powders, based on data in Table 5.1. The slope of the F-600 powder from the mean size to the maximum size is calculated as $-0.1\%/\mu\mathrm{m}$. The tail portion of the F-600 distribution from $15.8\mu m$ to the maximum is 7.3% of the total distribution volume. 85
5.7 Plot of individual roughness contributions from the F-400 and F-600 roughness models, as a function of the concentration factor k. For R_s^{400} , k is defined by k_{400}, though for R_s^{600}, k is defined by $(k_{max} - k_{600})$ to plot on the same axis. As abrasive concentration decreases (decrease in k) the roughness decreases for the models of both powders. F-400 is affected by the interaction of the F-600 abrasives beginning at a critical concentration $k^* = 0.4k_{max}$, and is the reason for the change in slope of the F-400 roughness curve at $k = 0.64 \times 10^{-6}$. 89
5.8 Comparison of material removal rate and RMS surface roughness at (a) 2.3-kg and (b) 4.1-kg loadings. 92
5.9 Plot of the mixed abrasive model and the experiemntally measured roughness as a function of F-400 particle concentration for (a) 2.3-kg and (b) 4.1-kg cases. 94

6.1 Fabrication of CNT brush by growing vertically aligned CNTs. 101
6.2 CNT brush compared to a penny 101
6.3 Manual operating single-axis platform 103

6.4 Modified AFM as machining device. 104
6.5 CNT forest deformation during machining. 105
6.6 Polished silicon wafer surface after CNT brushing, observed by an optical microscope. 105
6.7 Polished silicon wafer surface after CNT brushing, observed by an atomic force microscope. 106
6.8 Lapped silicon wafer surface after CNT brushing. 107
6.9 Lapped silicon wafer surface after CNT brushing, observed by SEM. 108
6.10 Lithium Niobate surface after CNT brushing, observed by an optical microscope. 108
6.11 The tool marks on the Lithium Niobate surface after CNT brushing, observed by AFM. 109
6.12 The original Lithium Niobate surface, observed by AFM. 109
6.13 Wrinkle on CNT forest after machining 111
6.14 Suspected Lithium Niobate chip on the surface of a CNT brush 111

7.1 Feedback control of distributed system with point sensing and point actuation [13] 115
7.2 Schematic of wire and free abrasives in slurry wiresaw system 115

List of Tables

5.1 FEPA Grading Chart of F-400 and F-600 SiC powders (μm) 77

5.2 Values of model parameters used to generate model results in Figure 5.9 . . 90

5.3 The average material removal rate (μm/min) under differing loadings and mixing ratios 91

5.4 The average RMS surface roughness (μm) under differing loadings and mixing ratios 93

5.5 The ratio between the material removal rate and the RMS surface roughness (unit: 1/min) 95

5.6 The increases of material removal rate (MRR) and RMS surface roughness from pure F-600 and F-400 to $1:1$ mixed abrasive slurries 96

Acknowledgements

Pursuing Ph.D. is an adventure in my life. It is my pleasure to have so many people with me in this journey. First and foremost, I would like to thank my advisor, Professor Imin Kao, for his guidance and support of my study. He introduced me into the study of wafer manufacturing. This dissertation will not be so fruitful without him. I am grateful to all my committee members, Professor Robert Kukta, Professor Chad S. Korach, Professor Lei Zuo, Professor Teng-fong Wong and Professor Michael Dudley. They provided thoughtful comments and suggestions which enriched my research. I would like to show my special appreciation to Professor Chad S. Korach. With his help in tribology, we collaborated on the study of experimental study and modeling of lapping using abrasive grits with mixed sizes.

I would like to thank Professor Shou-Hung Chang in National Taiwan University (NTU), Taiwan. With his help, I was able to conduct experiments using carbon nanotube brush in his laboratory at NTU. He provided the facilities to produce carbon nanotube forest and expertise to discuss the experimental results. I also want to thank all the students in his laboratory for their help.

My colleagues, Dylan Tsai, Kunbo Zhang, Roosevelt Moreno, Craig Capria, Jun Nishiyama, Xiaohai Zhu, and Glenn Melendez in Manufacturing Automation Laboratory (MAL) are very important for me. We went through all the typical difficulties that graduate students face in both class and research. In addition, I make a lot of friends in Stony Brook University. It is a wonderful experience for personal growth.

My family always supports me. I would like to thank my dear wife, Tsai-Pin Kuo, for her patience. It was not easy for the long-distance relationship in the first few years. Even after we got married, living abroad was another big challenge for her. Her unfaltering support for all these years, when I have to dedicate myself in research and study, has been a source of strength and encouragement.

Last but not least, my parents are the ones I want to show my most appreciation. My father, Chao-Yun Chung, always dreamed of attending my commencement when he was in hospital. Unfortunately, he could not make it. I know that he was always proud of my achievements, and I believe that he would be as usual at this time. My mother, Chun-Mei Lei, is a resolute and patient woman. She supported the family and my study after my father passed away. There are no words to express my thanks to her.

Chapter 1

Introduction

Wafering is an essential front-end manufacturing process in semiconductor and photovoltaic electronics industry. The wafer substrates affect the performance of the microelectronics fabrication, such as the production of IC chips and solar cells. Therefore, the quality of wafer substrates is extremely important. Defects and surface unevenness are undesirable and should be reduced to minimum. Another challenge in wafer production is the reduction of the manufacturing cost to afford the development and spread of the electronic and computer associated products. In order to reach these goals, advance in the wafer manufacturing process plays an important role. Additional innovation of machining tools enhances the development of the industry. The case in point is the development of modern slurry wiresaw [48, 49], which replaces inner diameter saws for large wafer slicing. Another example is the double-side grinding [55], which is adopted to remove the waviness of sliced wafers more effectively. Therefore, any improvement of the machining processes could result in more progress of the semiconductor industry.

Following Moore's law, the International Technology Roadmap of Semiconductors (ITRS) projects that the 450 mm wafer will be in production in 2012 [46] to keep the trend of cost reduction. A lot of analyses and discussions start to focus on this next generation wafer size [19, 28, 37, 79, 87, 96]. With the agreement of Intel, Samsung Electronics, and TSMC for the 450 mm wafer manufacturing transition [43], the advance of wafer size is inevitable. In addition, the 2008 update ITRS roadmap proposed the requirements of Site

Flatness (SFQR) for the area of $26 \times 8\text{mm}^2$ from 68 nm in 2007 to 36 nm in 2012 [33, 47]. The trend of wafer production is larger but flatter, which is an enormous challenge.

To achieve the requirements for the future specification of wafers, the progress in wafering processes such as slicing, lapping, grinding, and polishing is urgent. The improvement of the existing technology and the innovation of advanced machining tools are necessary for the future wafer production. In this dissertation, the research on the vibration of the wire in the slurry wiresaw system, mixed abrasive effect in lapping process, and wafer surface finishing by CNT brush will be presented. The corresponding influence on the wafering process will also be discussed.

1.1 Wafer Manufacturing Processes and Surface Topography

1.1.1 Wafer manufacturing processes

The semiconductor wafer manufacturing processes can be divided into: (1) Crystal growth, (2) Wafer Shaping, (3) Wafer Flattening, and (4) Cleaning, as shown in Figure 1.1. Wafer slicing is the first post-growth process in wafer shaping. In slicing, the slurry wiresaw has replaced the inner diameter saws (ID saws) for larger wafer, especially in producing the current 300 mm standard silicon wafers. It has the advantages such as ability to cut large ingot, higher throughput and lower kerf loss than the ID saw. Researchers have studied the machining behavior of slurry wiresaw such as the free abrasive machining process (FAM) [54, 63, 107], hydrodynamic effect [4, 64], slurry actions [44, 45, 89], and vibration response of the wire in slurry wiresaw system [97, 111]. However, the machining mechanism of slurry wiresaw remains a topic of active research investigation. After slicing, the next step is to flatten the wafer surface topography and to remove the subsurface damage. The machining processes used in this step are lapping, grinding, etching, and polishing. According to different process design and the emergence of new technology, the flow of

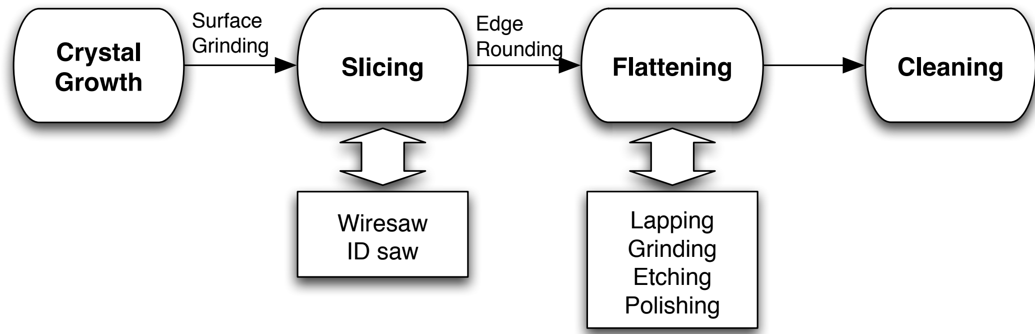

Figure 1.1: Folw chart of wafer manufacturing

the entire machining processes may be changed [55, 77].

The manufacturing processes for solar wafers is simpler than the semiconductor wafers. The as-sliced solar wafers are cleaned right after slicing, then sent to the cell manufacturer [33]. There is no flattening process. Therefore, the slicing process dominates the surface quality and evenness of solar wafers. Furthermore, the solar wafers, about 220 μm thick [33, 66], are much thinner than semiconductor wafer. The breakage of wafers during slicing and handling is one significant concern of the yield.

Lapping and slurry wiresawing processes belong to the free abrasive machining (FAM) process [22]. The major mechanism of free abrasive machining is rolling-indenting [48, 54, 107]. Most research shows that the major contribution of the material removal in lapping is indentation cracking [11, 12, 16, 52]. However, the real situation is more complicated [15, 38]. On the other hand, ID sawing, bounded abrasive wire sawing and grinding are bounded abrasive machining (BAM) processes. The machining mechanism is ploughing and shearing as those in metal machining processes. The ploughing process of brittle material is typically accompanied by microcracks along the machining path. Therefore, FAM processes are more suitable for machining than BAM processes.

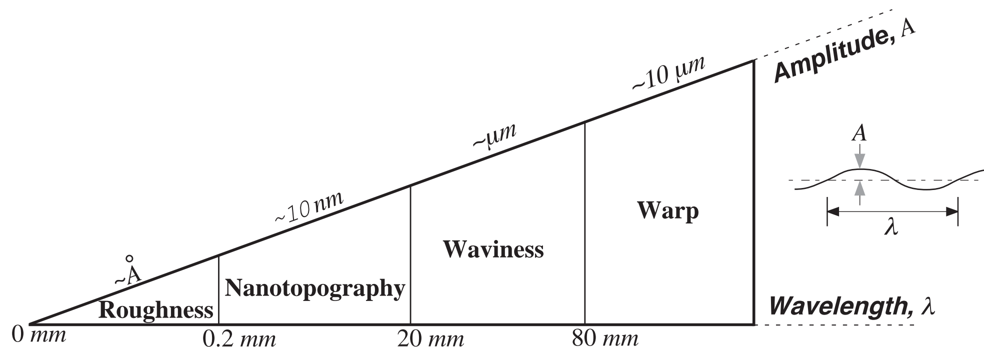

Figure 1.2: Classification of topographical features based on their spatial wavelengths. The order of amplitude of each feature is also illustrated [1].

1.1.2 Wafer geometry and surface characteristics

Wafer surface topology and geometry are important in characterizing wafer surfaces in wafer production. Due to the usage of popular capacitive probes in the wafer surface measurement, several parameters are often employed to characterize wafer surfaces. They are: (i) warp, (ii) total thickness variation (TTV), (iii) surface roughness, and (iv) waviness. The measurements of these parameters can be found in [39] or other references.

Figure 1.2 illustrates the nano-topographical features on wafer surfaces, with classification of topographical features based on their spatial wavelengths. Warp is the unevenness of wafer which has wavelength over $80\ \mathrm{mm}$, and with an amplitude of unevenness in the order of $10\ \mu\mathrm{m}$ or larger. Most research attributed the reason of warp to thermal expansion of the ingot and wire guides during slicing [2, 3, 6, 101]. Warp can also be caused by materials defect at the crystal growth stage and the ingot fixity during slicing [68]. Waviness also describes the unevenness of sliced wafers, but at a smaller scale than warp. It has a wavelength from $20\ \mathrm{mm}$ to $80\ \mathrm{mm}$, with a typical amplitude on the order of microns.

Waviness is a common characteristic of wiresaw-sliced wafer. The mechanism which results in waviness is still not well known. Both warp and waviness have to be removed in the flattening process. The requirement of site flatness (SFQR) after polishing is under $70\ \mathrm{nm}$ for $300\ \mathrm{mm}$ silicon wafer in 2006 [76]. Another important parameter is the total thickness variation, which is a good indication of the global planarization. TTV is the

difference between the maximum and minimum thicknesses of the wafer. The requirement for TTV is under $1\ \mu\mathrm{m}$ for $300\ \mathrm{mm}$ silicon wafers in 2006 [76].

1.2 Literature Review and Challenges

1.2.1 Vibration response of axially moving wire in slurry wiresaw system

The challenges of wafer manufacturing are always related to cost reduction. In order to achieve this goal, the diameter of wafer becomes larger and larger to increase the area of usage for IC fabrication. The thickness also becomes thinner to save material. Slurry wiresaw is the major slicing tool for both semiconductor and solar wafers today, and is expected to slice the next generation of 450 mm silicon wafers. However, the corresponding disadvantages such as warp and waviness still need to be overcomed. In addition, it is a challenge to further reduce kerf loss, although wiresaw already surpasses conventional ID saw in that. The vibration response of the wire in a slurry wiresaw system is a reason for kerf loss, as well as the surface roughness and the subsurface damage of wafers. Figure 1.3 defines the directions of wire motion. Although the oscillation of the wire in transverse direction can enhance the slicing efficiency [89], the motion in lateral direction can affect the surface quality and subsurface damage. Research shows that the amplitude of vibration response of the wire in wiresaw system under no-slurry and no-workpiece conditions can be up to 50 $\mu\mathrm{m}$ [62]. Nevertheless, the closed-form solution of the vibration response of the axially moving wire immersed in fluid is still elusive.

The vibration of a moving wire in wiresaw belongs to the axially moving continua. Because of the various applications such as thread line, power transmission belts, magnetic tapes, $\ldots$ etc., this field of study has received attention in the last decades to understand the properties and impacts of vibration of wire in such systems. A recent thorough review of research on this topic was done by Chen [18].

The closed-form solution of a stationary wire is well-known and can be solved by

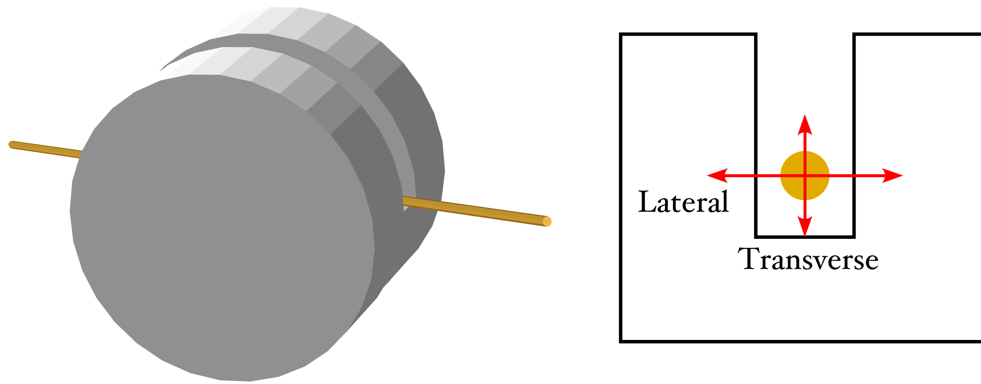

Figure 1.3: Schematics of wiresaw slicing and definition of directions

modal analysis [42, 61]. Wickert and Mote [99] first solved the general solution of an axially moving string by applying the modal analysis method for discrete linear gyroscopic systems [59, 60]. Yang and Tan [106] proposed a transform method by using Green's function [13, 83, 88]. Tan and Ying [92] applied the method with wave propagation function to obtain the solution of an axially moving string with general boundary conditions. In the same year, Renshaw [82] provided another decoupling concept and unified the modal analysis method for discrete and continuous systems. Their studies can also be applied to understand the vibration response of the wire in wiresaw system.

The moving wire of the modern slurry wiresaw immersed in abrasive slurry results in damping during the manufacturing operation with free abrasive machining [48]. To further understand the characteristics and render more relevant modeling and analysis, consideration of damping is necessary. The model of damped axially moving wire system was first proposed by Huang and Mote [40]. Wei and Kao [97] obtained numerical results of damped model under external harmonic excitation to study slurry wiresaw systems. Because of the hydrodynamic thin film formed between the wire and substrate surface, Zhu and Kao included the hydrodynamic effect into the consideration of vibration analysis [111]. However, the closed-form solution of the damped axially moving wire system remains unsolved. In order to advance the modeling and analysis of the slurry wiresaw manufacturing process, such closed-form solution is essential.

1.2.2 Mixed abrasive effect in lapping process

Lapping has been for a long time a standard wafer machining process after slicing. It belongs to the free abrasive machining (FAM) process which is the same as slurry wiresaw slicing process [22]. This is one of the reasons why the lapping machining process is not easy to model. Most research emphasized the major contribution of the material removal on the cracking model [11, 12, 16, 52]. However, the real situation may be more complicated [15, 38]. The most comprehensive modeling was done by Chang *et al.* [15]. In their model, four mechanisms were considered: two-body ductile, two-body brittle, three-body ductile, and three-body brittle machining.

Many research emphasized the importance of abrasive size distribution in modeling. Nonetheless, few studied the change of the distribution of the abrasive grit sizes. Bhagavat *et al.* [7, 8] are probably the first and the only ones to study such topic. Their results showed that the mixed abrasives (for example, mixing F-400 and F-600 SiC) had higher material removal rate than the single-sized abrasives (for example, only F-400 SiC abrasives). However, their experiments discussed one mixing ratio of the abrasives, and the concentration of slurry of mixed abrasive is different form that of the single-sized abrasives slurry. To understand the influence of the change of abrasive distribution in lapping process, experiments with different abrasive distributions and fixed slurry concentration are necessary.

1.2.3 Wafer surface finishing by CNT brush

In wafer production, the subsurface damage is always present under the machining processes such as slicing, lapping, and grinding. To achieve the requirements of surface planarization and to remove these subsurface damage introduced by the previous machining processes, polishing is last step to finish the wafer surface in the standard wafer manufacturing processes. However, research shows that these brittle materials could be machined like ductile materials under some conditions which is called Ductile-Regime Machining [72].

In this case, the subsurface damage would not happen during the machining processes. Ductile-Regime Machining on the brittle material has already been studied for over ten years [9] and has fruitful results, which will be discuss in Chapter 6. However, a feasible solution for the industry is still absent.

Carbon Nanotubes (CNTs), is one of the most popular materials under study since last century. CNT has a lot of excellent properties in electronics and mechanics, with potential applications in many fields [29]. However, it is unusual to utilize it as machine tool. This idea first came out of machining of copper by CNT forest [41]. The results show the improvement in the surface roughness. Nonetheless, the feasibility of machining brittle materials by CNT brush remains a challenge. Because brittle materials are usually harder, the strength of CNT brush becomes very important. Besides, Ductile-Regime Machining is a very precise machining process. The control of depth of cut and machining velocity may influence the outcomes.

1.3 Outlines and Contribution of the Chapters

In this dissertation, an introduction and literature review are provided in Chapter 1. Following that are five chapters addressing three topics in wafer manufacturing. The vibration response of damped axially moving wire in slurry wiresaw will be presented in Chapters 2, 3, and 4. In Chapter 2, the closed-from solution of the free vibration response of damped axially moving wire is provided. The classical modal analysis was utilized to derive and obtain this solution. The corresponding eigenvalues, eigenfunctions, and orthogonal relationship are also presented. In Chapter 3, the characteristics of damped axially moving wire will be analyzed based on the solution in Chapter 2. The damping ratio and damping index are defined in this chapter. The mode shapes and apparent damping effect are also discussed. A parameter study of real slurry wiresaw system is presented. In order to derive the forced vibration response, the Green's function is derived and presented in Chapter 4. With the solution of the Green's function of damped axially moving wire, the

frequency response with a point excitation can be obtained. The results of mixed abrasive effect experiments are presented in Chapter 5, as well as the modeling and analysis of surface roughness. Preliminary study of CNT brushing will be presented in Chapter 6. The conclusions of this dissertation are presented in Chapter 7 with future research.

Chapter 2

Free Vibration Response of Damped Axially Moving Wire

Modern slurry wiresaw has been utilized in wafer manufacturing to slice ingot into wafers since the 1990s. It is important to understand and analyze vibration of the axially moving wire in a slurry wiresaw equipment in order to improve the performance and reduce the kerf loss. However, the closed-form solution of axially moving wire with damping, under the context of wire moving in slurry, is still elusive. In this chapter, the classical modal analysis is applied to derive the analytical solution and to obtain the free vibration response of damped axially moving wire. The corresponding eigenvalues, eigenfunctions, and orthogonal relationship are also presented. The orthogonality relationship is very important in the derivation of analytical equations of free vibration response with damping. The orthogonality property and closed-form solution of free vibration response with damping are the main contribution of this chapter. In addition, the analytical modal analysis, with damping factor removed, shows agreement with those in existing research literature of moving wire without damping.

2.1 Introduction

Wiresaw is a century-old technology, used to slab stones for construction since the 19th century. Nonetheless, wiresaw has been brought into focus of research today when it is employed for wafer production in modern manufacturing with more stringent requirements

of surface finish and quality. The modern slurry wiresaws have numerous advantages such as the ability to slice large ingots of different materials, low kerf loss, and high yield [48]. Various research has been conducted to study the slicing process of modern slurry wiresaw technology [22]. The vibration analysis of the moving wire of slurry wiresaws has important implication in the outcomes of the surface roughness of sliced wafers and kerf loss which are very important issues in wafer slicing using modern slurry wiresaw.

The vibration of a moving wire in wiresaw belongs to the axially moving continua [23, 24]. Because of the various applications such as band saw, power transmission belts, magnetic tapes, . . . etc., this field of study has received attention in the last decades to understand the properties and impacts of vibration of axially moving continua in such systems. A recent thorough review of research on this topic was done by Chen [18].

Similar to a stationary wire, the axially moving wire can be modeled as a linear system by small amplitude assumption. Wickert and Mote [99] first obtained the general solution of axially moving string by converting the system into a canonical form and applying the modal analysis method for discrete linear gyroscopic systems [59, 60]. Yang and Tan [106] presented a transform method by using the Laplace Transform and Green's function. Later, Tan and Ying [92] applied the method with wave propagation function to obtain the solution of axially moving string with general boundary conditions. In the same year, Renshaw [82] proposed another decoupling concept and unified the modal analysis method for discrete and continuous systems. Other research has focused on the elastic foundation [71, 78, 93, 94, 98] or stationary load system which constrains the wire between the boundaries [17]. In addition, the variable length and tension of the wire have been studied for the application of elevators [112, 113]. Their studies can also be applied to understand the vibration response of the wire in wiresaw system.

The moving wire in modern wiresaw with abrasive slurry has appreciable damping effect due to the manufacturing operation with free abrasive machining [23, 24, 48]. To further understand the characteristics and render more relevant modeling and analysis,

consideration of damping in wiresawing process is necessary. The model of damped axially moving wire system was first proposed by Huang and Mote [40]. Wei and Kao [97] obtained numerical results of damped model under external harmonic excitation to study slurry wiresaw system. Because of the hydrodynamic thin film formed between the wire and substrate surface, Zhu and Kao included the hydrodynamic effect into consideration of vibration analysis [111]. However, the closed-form solution of the damped axially moving wire system remains elusive. In order to advance the modeling and analysis of the slurry wiresaw manufacturing process, such closed-form solution is essential.

In this chapter, the classical method to solve the partial differential equation was utilized with the adjoint equation to solve the equation of motion. The main contribution of this chapter is the derivation of the orthogonal relationship and consequently the free vibration response of an axially moving wire with damping. In Section 2.2, the equation of motion of damped axially moving wire is derived based on extended Hamilton's principle. In Section 2.3, the eigensolutions are presented. In Section 2.4, modal analysis of the damped axially moving wire is studied to obtain the orthogonal relationship. Based on the the results in the previous sections, the solution of free vibration response is presented in Section 2.5. General discussion is provided in Sections 2.6, followed by the summary of this chapter in Section 2.7

2.2 Equation of Motion of Damped Axially Moving Wire

An axially moving wire with transverse vibration is shown in Figure 2.1. The parameters are defined in the following:

- Spatial variable is X, which has the domain $0 < X < L$, where L is the length of the wire.

- Temporal variable is the time T, with $T \geq 0$.

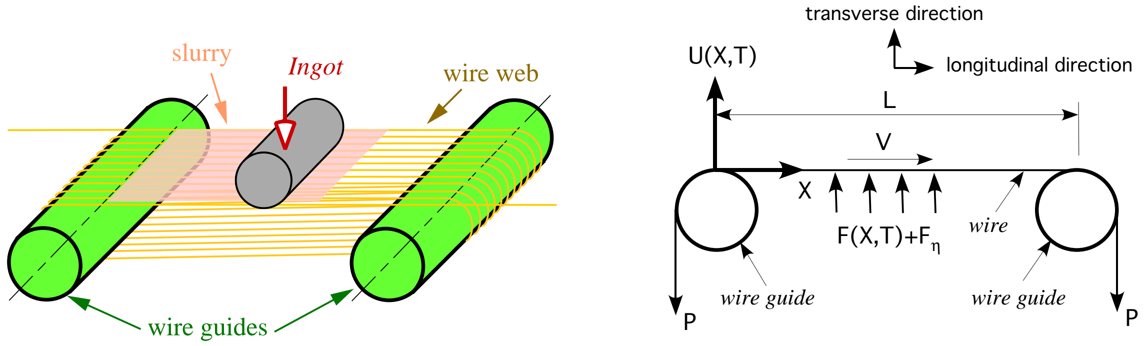

Figure 2.1: Schematic of wiresaw system. The transverse and longitudinal directions are defined and shown.

- The transverse displacement is $U(X,T)$, as shown in Figure 2.1, with fixed boundary conditions. Therefore, $U(X,T)$ is zero at $X = 0$ and $X = L$.
- The mass per unit length of wire is denoted by $\rho(X)$.
- The tension of the wire is denoted by $P(X)$.
- The wire speed is denoted by V, which is a constant.
- The external force per unit length is $F(X,T)$.
- The damping force per unit length is $F_\eta(X,T) = -\eta_d(VU_X + U_T)$, which is the viscous damping force with $(VU_X + U_T)$ being the transverse velocity [1] .

In the context of a moving wire in wiresaw, the ranges of parameters are $V = 10 \sim 15\,\mathrm{m\,s^{-1}}$ and $P = 25 \sim 35\,\mathrm{N}$. The viscous damping force, F_η, is caused by the abrasive slurry in which the moving wire is immersed. The viscosity of typical abrasive slurry was presented in [48] in the range of $200 \sim 1000\,\mathrm{cP}$.

Equation of motion is essential for the study of vibration. The equation of motion of damped axially moving wire has been presented in literature [40, 97]. In this section, the

[1] The viscous damping force is assumed to be the product of the component of the transverse velocity and the viscous damping factor, η_d, of the abrasive slurry. The transverse velocity, $(VU_X + U_T)$, is the component of velocity along the transverse direction shown in Figure 2.1.

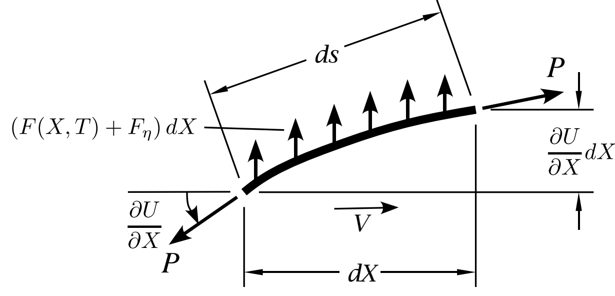

Figure 2.2: Differential element of wire.

equation of motion is derived based on the extended Hamilton's principle, which can be expressed in the form [61]

$$\int_{T_1}^{T_2} \left(\delta E_T - \delta E_V + \overline{\delta W}_{nc}\right) dT = 0, \quad \delta U(X,T) = 0 \text{ at } T = T_1, T_2 \tag{2.1}$$

where

$$E_T = \frac{1}{2}\int_0^L \rho(X)\left[V^2 + \left(\frac{\partial U(X,T)}{\partial T} + V\frac{\partial U(X,T)}{\partial X}\right)^2\right] dX \tag{2.2}$$

is the kinetic energy. The potential energy is due to the tension in the wire. It can be expressed as

$$E_V = \int_0^L P(X)\,(ds - dX) \tag{2.3}$$

where ds is the elongated length of the differential element dX as shown in Figure 2.2. With the assumption of $\partial U/\partial X \ll 1$, we can write

$$ds = \left[(dX)^2 + \left(\frac{\partial U}{\partial X}dX\right)^2\right]^{1/2} = \left[1 + \left(\frac{\partial U}{\partial X}\right)^2\right]^{1/2} dX \cong \left[1 + \frac{1}{2}\left(\frac{\partial U}{\partial X}\right)^2\right] dX \tag{2.4}$$

Substituting equation (2.4) into equation (2.3), we obtain

$$E_V = \frac{1}{2}\int_0^L P(X)\left(\frac{\partial U}{\partial X}\right)^2 dX \tag{2.5}$$

Moreover, the virtual work due to the nonconservative distributed external force and damping force is

$$\overline{\delta W}_{nc} = \int_0^L (F(X,T) + F_\eta)\,\delta U\,dX \tag{2.6}$$

From equation (2.2), the variation in the kinetic energy is obtained as

$$\delta E_T = \int_0^L \rho(X)\left[\frac{\partial U}{\partial T}\,\delta\!\left(\frac{\partial U}{\partial T}\right) + V\frac{\partial U}{\partial X}\,\delta\!\left(\frac{\partial U}{\partial T}\right) + V\frac{\partial U}{\partial T}\,\delta\!\left(\frac{\partial U}{\partial X}\right) + V^2\frac{\partial U}{\partial X}\,\delta\!\left(\frac{\partial U}{\partial X}\right)\right] dX \tag{2.7}$$

Similarly, the variation in the potential energy is obtained form equation (2.5)

$$\delta E_V = \int_0^L P(X)\frac{\partial U}{\partial X}\,\delta\left(\frac{\partial U}{\partial X}\right)dX \tag{2.8}$$

Integrating equation (2.7) with respect to time, and assuming that the integration is interchangeable, we obtain

$$\begin{aligned}
&\int_{T_1}^{T_2}\delta E_T dT\\
&= \int_{T_1}^{T_2}\int_0^L \rho(X)\left[\frac{\partial U}{\partial T}\,\delta\left(\frac{\partial U}{\partial T}\right)+V\frac{\partial U}{\partial X}\,\delta\left(\frac{\partial U}{\partial T}\right)+V\frac{\partial U}{\partial T}\,\delta\left(\frac{\partial U}{\partial X}\right)+\right.\\
&\quad \left.V^2\frac{\partial U}{\partial X}\,\delta\left(\frac{\partial U}{\partial X}\right)\right]dX\,dT\\
&= \int_{T_1}^{T_2}\int_0^L \rho(X)\left[\frac{\partial U}{\partial T}\frac{\partial \delta U}{\partial T}+V\frac{\partial U}{\partial X}\frac{\partial \delta U}{\partial T}+V\frac{\partial U}{\partial T}\frac{\partial \delta U}{\partial X}+V^2\frac{\partial U}{\partial X}\frac{\partial \delta U}{\partial X}\right]dX\,dT\\
&= \int_0^L\int_{T_1}^{T_2}\rho(X)\left[\frac{\partial U}{\partial T}+V\frac{\partial U}{\partial X}\right]\frac{\partial \delta U}{\partial T}dT\,dX+\\
&\quad \int_{T_1}^{T_2}\int_0^L \rho(X)\left[V\frac{\partial U}{\partial T}+V^2\frac{\partial U}{\partial X}\right]\frac{\partial \delta U}{\partial X}dX\,dT\\
&= \int_0^L\left\{\rho(X)\left(\frac{\partial U}{\partial T}+V\frac{\partial U}{\partial X}\right)\delta U\Big|_{T_1}^{T_2}-\int_{T_1}^{T_2}\rho(X)\frac{\partial}{\partial T}\left[\frac{\partial U}{\partial T}+V\frac{\partial U}{\partial X}\right]\delta U\,dT\right\}dX+\\
&\quad \int_{T_1}^{T_2}\left\{\rho(X)\left(V\frac{\partial U}{\partial T}+V^2\frac{\partial U}{\partial X}\right)\delta U\Big|_0^L-\int_0^L\frac{\partial}{\partial X}\left[\rho(X)\left(V\frac{\partial U}{\partial T}+V^2\frac{\partial U}{\partial X}\right)\right]\delta U\,dX\right\}dT\\
&= \int_{T_1}^{T_2}\left\langle-\int_0^L\left\{\rho(X)\frac{\partial}{\partial T}\left[\frac{\partial U}{\partial T}+V\frac{\partial U}{\partial X}\right]+\frac{\partial}{\partial X}\left[\rho(X)\left(V\frac{\partial U}{\partial T}+V^2\frac{\partial U}{\partial X}\right)\right]\right\}\delta U\,dX+\right.\\
&\quad \left.\rho(X)\left(V\frac{\partial U}{\partial T}+V^2\frac{\partial U}{\partial X}\right)\delta U\Big|_0^L\right\rangle dT
\end{aligned} \tag{2.9}$$

Use integration by parts with respect to X and rewrite equation (2.8) to obtain

$$\begin{aligned}
\delta E_V &= \int_0^L P(X)\frac{\partial U}{\partial X}\,\delta\left(\frac{\partial U}{\partial X}\right)dX\\
&= \int_0^L P(X)\frac{\partial U}{\partial X}\frac{\partial \delta U}{\partial X}dX\\
&= P(x)\frac{\partial U}{\partial X}\delta U\Big|_0^L-\int_0^L\frac{\partial}{\partial X}\left[P(X)\frac{\partial U}{\partial X}\right]\delta U\,dX
\end{aligned} \tag{2.10}$$

Substituting equations (2.6), (2.9) and (2.10) into equation (2.1), we can obtain

$$\int_{T_1}^{T_2} \left\langle -\int_0^L \left\{ \rho(X)\frac{\partial}{\partial T}\left[\frac{\partial U}{\partial T} + V\frac{\partial U}{\partial X}\right] + \frac{\partial}{\partial X}\left[\rho(X)\left(V\frac{\partial U}{\partial T} + V^2\frac{\partial U}{\partial X}\right)\right] \right.\right.$$
$$\left. - \frac{\partial}{\partial X}\left[P(X)\frac{\partial U}{\partial X}\right] - F(X,T) - F_\eta \right\} \delta U dX$$
$$\left. + \left[\rho(X)\left(V\frac{\partial U}{\partial T} + V^2\frac{\partial U}{\partial X}\right) - P(x)\frac{\partial U}{\partial X}\right]\delta U\Big|_0^L \right\rangle dT = 0 \tag{2.11}$$

Since the mass per unit length $\rho(X)$ and the tension of the wire $P(X)$ are assumed to be constants in this study, the equation of motion of the damped axially moving wire is obtained as

$$\rho\left(\frac{\partial^2 U}{\partial T^2} + 2V\frac{\partial^2 U}{\partial X \partial T} + V^2\frac{\partial^2 U}{\partial X^2}\right) - P(X)\frac{\partial^2 U}{\partial X^2} = F(X,T) + F_\eta \tag{2.12}$$

where $F_\eta = -\eta_d(U_T + VU_X)$. The boundary conditions are $U(X,T) = 0$ at $X = 0$ and $X = L$.

2.3 Solution of the Eigenvalue Problem of a Moving Wire in a Damped System

In this section, the solution of the eigenvalue problem associated with a damped axially moving wire is presented first. After that, the adjoint eigenvalue problem is also solved.

2.3.1 Eigenvalue problem

Modal analysis was first applied to obtain the closed-form solution for vibration of axially moving continua in [99] and has become a popular method to solve this kind of problems. The eigensolution of damped axially moving wire has been presented in [95]. The analytical solution of the eigenvalue problem presented in this section results in the same solution as that in [95] when the corresponding parameters are correlated. However, the derivation of orthogonality and the resulting analytical solution of the free vibration response have not been presented before. In this section, a systematic solution of the

eigenproblem is provided to support the derivation of the orthogonality and free vibration response in the later sections.

The equation of motion can be non-dimensionalized by introducing the following definitions of parameters

$$x = X/L \qquad u = U/L \qquad t = T\sqrt{\frac{P}{\rho L^2}} \qquad f = FL/P \qquad v = V\sqrt{\frac{\rho}{P}} \qquad \eta = \frac{\eta_d L}{\sqrt{P\rho}} \tag{2.13}$$

Thus, the non-dimensionalized equation of motion of the damped axially moving wire can be obtained from equation (2.12) in the following

$$u_{tt} + 2vu_{xt} - (1 - v^2)u_{xx} + \eta v u_x + \eta u_t = f \tag{2.14}$$

or expressed in the form of differential operators as

$$\mathrm{M}u_{tt} + (\mathrm{C} + \mathrm{G})\, u_t + (\mathrm{K} + \mathrm{H})\, u = f \tag{2.15}$$

where $\mathrm{M} = I$, $\mathrm{C} = \eta$, $\mathrm{G} = 2v\frac{\partial}{\partial x}$, $\mathrm{K} = -(1 - v^2)\frac{\partial^2}{\partial x^2}$, and $\mathrm{H} = \eta v \frac{\partial}{\partial x}$. The boundary conditions become $u(0, t) = u(1, t) = 0$. The differential operators M, C, and K are self-adjoint operators, while G and H are not. The adjoint operators have the following properties $\mathrm{G}^* = -\mathrm{G}$, and $\mathrm{H}^* = -\mathrm{H}$ according to the boundary conditions.

To obtain the eigenvalues and eigenfunctions of this system, we first consider a homogeneous differential equation with no external excitation (i.e., $f = 0$). Assume a solution of the form of

$$u(x, t) = \psi(x)\, \mathrm{e}^{\lambda t} \tag{2.16}$$

where $\psi(x)$ is eigenfunction and λ is eigenvalue. Substitute equation (2.16) into equation (2.15) to obtain

$$\lambda^2 \mathrm{M}\psi(x) + \lambda\, (\mathrm{C} + \mathrm{G})\, \psi(x) + (\mathrm{K} + \mathrm{H})\, \psi(x) = 0 \tag{2.17}$$

which can also be rewritten as

$$(1 - v^2)\frac{\partial^2 \psi(x)}{\partial x^2} - (2v\lambda + v\eta)\frac{\partial \psi(x)}{\partial x} - (\lambda^2 + \eta\lambda)\psi(x) = 0$$

Equation (2.17) does not represent a self-adjoint system and can not be converted into Sturm-Liouville problem [36]. Therefore, the eigenfunctions of equation (2.17) do not have the same orthogonal property associated with the vibration of a stationary wire. This poses a challenge on the study of the vibration of axially moving wire. To solve equation (2.17), we further assume

$$\psi(x) = \mathrm{e}^{\kappa x} \tag{2.18}$$

Substituting equation (2.18) into equation (2.17) and removing the common term, $\mathrm{e}^{\kappa x}$, equation (2.17) can be rewritten as

$$(1 - v^2)\kappa^2 - (2v\lambda + v\eta)\kappa - (\lambda^2 + \eta\lambda) = 0$$

The roots of this quadratic equation are

$$\kappa_{1,2} = \frac{v(2\lambda + \eta) \pm \sqrt{4\lambda^2 + 4\eta\lambda + v^2\eta^2}}{2(1 - v^2)} = \alpha \pm \beta \tag{2.19}$$

where $\alpha = \frac{v(2\lambda+\eta)}{2(1-v^2)}$ and $\beta = \frac{\sqrt{4\lambda^2+4\eta\lambda+v^2\eta^2}}{2(1-v^2)}$. Therefore, the solution of the eigenfunction is

$$\psi(x) = \mathrm{e}^{\alpha x}\left(A_1\mathrm{e}^{\beta x} + A_2\mathrm{e}^{-\beta x}\right) \tag{2.20}$$

where A_1 and A_2 are arbitrary constants. Because the boundary conditions are $u(x,t) = 0$ at $x = 0$ and $x = 1$, the corresponding boundary conditions for $\psi(x)$ are $\psi(0) = \psi(1) = 0$. Substituting $\psi(0) = 0$ into equation (2.20) to obtain $A_1 + A_2 = 0$. Therefore, $A_1 = -A_2 = A$. Equation (2.20) becomes

$$\psi(x) = A\,\mathrm{e}^{\alpha x}\left(\mathrm{e}^{\beta x} - \mathrm{e}^{-\beta x}\right) \tag{2.21}$$

Using the other boundary condition $\psi(1) = 0$, we have $\mathrm{e}^{\alpha}\left(\mathrm{e}^{\beta} - \mathrm{e}^{-\beta}\right) = 0$. Because e^{α} can not be zero for non-trivial solution, so $\mathrm{e}^{\beta} - \mathrm{e}^{-\beta} = 0$. Therefore,

$$\beta_n = in\pi, \qquad n = 0, \pm 1, \pm 2, \ldots \tag{2.22}$$

In order to solve the eigenvalues, we substitute the definition of β in equation (2.22) into equation (2.19) to obtain

$$\beta_n = \frac{\sqrt{4\lambda_n^2 + 4\lambda_n\eta + v^2\eta^2}}{2(1 - v^2)} = \mathrm{i}n\pi$$

The eigenvalues λ_n are

$$\lambda_n = \frac{-\eta \pm \sqrt{\left[\eta^2 - 4n^2\pi^2(1-v^2)\right](1-v^2)}}{2}$$

which can be written separately as

$$\lambda_{1n} = \frac{-\eta + \sqrt{\left[\eta^2 - 4n^2\pi^2(1-v^2)\right](1-v^2)}}{2} = -\frac{\eta}{2} + \mathrm{i}\omega_{1n} \tag{2.23}$$

$$\lambda_{2n} = \frac{-\eta - \sqrt{\left[\eta^2 - 4n^2\pi^2(1-v^2)\right](1-v^2)}}{2} = -\frac{\eta}{2} + \mathrm{i}\omega_{2n} \tag{2.24}$$

where $\omega_{1n} = -\omega_{2n} = \omega_{d,n}$ is the damped vibration frequency associated with λ_n as follows

$$\omega_{d,n} = \frac{\sqrt{\left[4n^2\pi^2(1-v^2) - \eta^2\right](1-v^2)}}{2} \tag{2.25}$$

The corresponding α_{1n} and α_{2n} in equation (2.19) are

$$\alpha_{1n} = \frac{v\sqrt{\left[\eta^2 - 4n^2\pi^2(1-v^2)\right](1-v^2)}}{2(1-v^2)} = \frac{\mathrm{i}v\omega_{1n}}{1-v^2}$$

$$\alpha_{2n} = \frac{-v\sqrt{\left[\eta^2 - 4n^2\pi^2(1-v^2)\right](1-v^2)}}{2(1-v^2)} = \frac{\mathrm{i}v\omega_{2n}}{1-v^2} = -\alpha_{1n}$$

According to equation (2.21), the eigenfunctions associated with λ_{1n} and λ_{2n} are

$$\begin{aligned} \psi_{1n}(x) &= \mathrm{e}^{\alpha_{1n}x}\sin n\pi x = \mathrm{e}^{\frac{\mathrm{i}v\omega_{1n}}{1-v^2}x}\sin n\pi x \\ \psi_{2n}(x) &= \mathrm{e}^{\alpha_{2n}x}\sin n\pi x = \mathrm{e}^{\frac{\mathrm{i}v\omega_{2n}}{1-v^2}x}\sin n\pi x \end{aligned} \tag{2.26}$$

Applying the solution of the eigenvalues, λ_{1n} and λ_{2n}, and the eigenfunctions, ψ_{1n} and ψ_{2n}, the free vibration response can be obtained by substituting the solutions into equa-

tion (2.16), as follows

$$\begin{aligned}
u(x,t) &= \sum_{n=-\infty}^{\infty}\left[B_{1n}\psi_{1n}(x)\,\mathrm{e}^{\lambda_{1n}t}+B_{2n}\psi_{2n}(x)\,\mathrm{e}^{\lambda_{2n}t}\right]\\
&= \sum_{n=-\infty}^{\infty}\left[B_{1n}\left(\mathrm{e}^{\alpha_{1n}x}\,\sin n\pi x\right)\mathrm{e}^{\lambda_{1n}t}+B_{2n}\left(\mathrm{e}^{\alpha_{2n}x}\,\sin n\pi x\right)\mathrm{e}^{\lambda_{2n}t}\right]\\
&= \sum_{n=-\infty}^{-1}\left[B_{1n}\left(\mathrm{e}^{\alpha_{1n}x}\,\sin n\pi x\right)\mathrm{e}^{\lambda_{1n}t}+B_{2n}\left(\mathrm{e}^{\alpha_{2n}x}\,\sin n\pi x\right)\mathrm{e}^{\lambda_{2n}t}\right]+\\
&\quad \sum_{n=1}^{\infty}\left[B_{1n}\left(\mathrm{e}^{\alpha_{1n}x}\,\sin n\pi x\right)\mathrm{e}^{\lambda_{1n}t}+B_{2n}\left(\mathrm{e}^{\alpha_{2n}x}\,\sin n\pi x\right)\mathrm{e}^{\lambda_{2n}t}\right]\\
&= \sum_{n=1}^{\infty}\left[B_{-1n}\left(\mathrm{e}^{\alpha_{-1n}x}\,\sin(-n\pi x)\right)\mathrm{e}^{\lambda_{-1n}t}+B_{-2n}\left(\mathrm{e}^{\alpha_{-2n}x}\,\sin(-n\pi x)\right)\mathrm{e}^{\lambda_{-2n}t}\right]+\\
&\quad \sum_{n=1}^{\infty}\left[B_{1n}\left(\mathrm{e}^{\alpha_{1n}x}\,\sin n\pi x\right)\mathrm{e}^{\lambda_{1n}t}+B_{2n}\left(\mathrm{e}^{\alpha_{2n}x}\,\sin n\pi x\right)\mathrm{e}^{\lambda_{2n}t}\right]
\end{aligned}$$

where B_{1n} and B_{2n} are coefficients. Because $\lambda_{-1n}=\lambda_{1n}$, $\lambda_{-2n}=\lambda_{2n}$, $\alpha_{-1n}=\alpha_{1n}$, and $\alpha_{-2n}=\alpha_{2n}$, the response $u(x,t)$ can be simplified as

$$\begin{aligned}
u(x,t) &= \sum_{n=1}^{\infty}\left[D_{1n}\left(\mathrm{e}^{\alpha_{1n}x}\,\sin n\pi x\right)\mathrm{e}^{\lambda_{1n}t}+D_{2n}\left(\mathrm{e}^{\alpha_{2n}x}\,\sin n\pi x\right)\mathrm{e}^{\lambda_{2n}t}\right]\\
&= \sum_{n=1}^{\infty}\left[D_{1n}\psi_{1n}(x)\,\mathrm{e}^{\lambda_{1n}t}+D_{2n}\psi_{2n}(x)\,\mathrm{e}^{\lambda_{2n}t}\right]\\
&= \sum_{n=1}^{\infty}u_n(x,t) \qquad (2.27)
\end{aligned}$$

where $D_{1n}=B_{1n}-B_{-1n}$ and $D_{2n}=B_{2n}-B_{-2n}$ are the coefficients. The term $u_n(x,t)$ represents the nth component of the free vibration response which is expected to be a real function, not complex, in order to represent the free vibration response in the physical system. In some literatures, $u_n(x,t)$ is called as "mode." However, "mode" is normally specified for the spatial function (eigenfunction) in most of the vibration literature. In order to avoid the confusion of terminology, we choose to call $u_n(x,t)$ "the nth component of response" of $u(x,t)$.

The stability of damped axially moving string was discussed in [95]. However, the discussion did not consider the situation when $v=1$, and claimed that asymptotic stability

of the motion was confirmed for all transport speeds and viscous damping factors. In reality, based on the solution presented here, the eigenfunctions will become divergent and make the system unstable when the velocity approaches the critical speed, corresponding to the nondimensionalized parameter $v = 1$. As suggested in [97], operating a moving wire near or at the critical speed, if that were possible, would cause instability of the system.

2.3.2 Adjoint eigenvalue problem

For a differential operator, $\mathcal{D}$, there is an adjoint differential operator $\mathcal{D}^*$ that will satisfy[2]

$$< \mathcal{D}[g], h >=< g, \mathcal{D}^*[h] >$$

where g and h are functions [42]. If $\mathcal{D}^* = \mathcal{D}$, the differential operator is self-adjoint. The adjoint eigenvalue problem of equation (2.15) is [82]

$$\lambda^{*2}\mathrm{M}^*\psi^*(x) + \lambda^*\left(\mathrm{C}^* + \mathrm{G}^*\right)\psi^*(x) + \left(\mathrm{K}^* + \mathrm{H}^*\right)\psi^*(x) = 0 \tag{2.28}$$

Using the same steps presented in Section 2.3.1 to solve the eigenvalue problem of equation (2.28), the corresponding adjoint eigenvalues and eigenfunctions are

$$\begin{gathered}
\lambda_{1n}^* = \lambda_{1n} = -\frac{\eta}{2} + \mathrm{i}\omega_{1n} \qquad \lambda_{2n}^* = \lambda_{2n} = -\frac{\eta}{2} + \mathrm{i}\omega_{2n} = -\frac{\eta}{2} - \mathrm{i}\omega_{1n} \\
\psi_{1n}^*(x) = \mathrm{e}^{-\frac{\mathrm{i}v\omega_{1n}}{1-v^2}x}\sin n\pi x \quad \text{for} \quad \psi_{1n}(x) = \mathrm{e}^{\frac{\mathrm{i}v\omega_{1n}}{1-v^2}x}\sin n\pi x \\
\psi_{2n}^*(x) = \mathrm{e}^{-\frac{\mathrm{i}v\omega_{2n}}{1-v^2}x}\sin n\pi x \quad \text{for} \quad \psi_{2n}(x) = \mathrm{e}^{\frac{\mathrm{i}v\omega_{2n}}{1-v^2}x}\sin n\pi x
\end{gathered} \tag{2.29}$$

The adjoint eigenvalue problem shares the same eigenvalues with the original eigenvalue problem. When ω_{1n} and ω_{2n} are real, the eigenvalues are complex conjugates, so are the eigenfunctions. Here, we choose the eigenvalues and their adjoint eigenvalues to be the same[3] ; that is, $\lambda_{1n} = \lambda_{1n}^*$ and $\lambda_{2n} = \lambda_{2n}^*$. As a result, the pairs of the eigenfunctions and their corresponding adjoint eigenfunctions, (ψ_{1n}, ψ_{1n}^*) and (ψ_{2n}, ψ_{2n}^*), are complex

[2] The definition of the bracket operation, or inner product, is $< \mathcal{D}[g], h >= \int \mathcal{D}[g] \cdot \bar{h} dx$, where $\bar{h}$ is the complex conjugate of h [42].

[3] Note that the definitions and solutions of eigenvalues (λ_{1n}, λ_{2n}, λ_{1n}^*, λ_{2n}^*) and eigenfunctions (ψ_{1n}, ψ_{2n}, ψ_{1n}^*, ψ_{2n}^*) are different from those in [53]. Consequently, the relationships of complex conjugates are also different.

conjugate pairs. This definition makes it easier for us to develop the orthogonal relationship of damped axially moving wire, which will be discussed in the next section.

2.4 Orthogonal Relationship of the Eigenfunctions

The orthogonality is critical to determine the coefficients of the free vibration response in Section 2.5. One cannot obtain the analytical solution without the orthogonally property, which gives rise to the asymmetric motion of the axially moving wire. This is a new contribution. The closed-form analytical solution of free vibration, as a result of the orthogonality property, can be employed to discriminate the modes that play more significant role in free vibration under prescribed initial conditions. This is also validated by the results. One of the contributions of this study is the derivation and presentation of the orthogonal relationship for damped axially moving wire system. In this section, the orthogonality property will be derived using the relationship between the eigensolutions and their corresponding adjoint eigensolutions discussed in the previous section.

Substituting the eigensolutions and adjoint eigensolutions into equations (2.17) and (2.28), we obtain

$$\lambda_n^2 \mathrm{M}\left[\psi_n(x)\right] + \lambda_n \left(\mathrm{C}+\mathrm{G}\right)\left[\psi_n(x)\right] + \left(\mathrm{K}+\mathrm{H}\right)\left[\psi_n(x)\right] = 0 \tag{2.30}$$

$$\lambda_m^2 \mathrm{M}^*\left[\psi_m^*(x)\right] + \lambda_m \left(\mathrm{C}^*+\mathrm{G}^*\right)\left[\psi_m^*(x)\right] + \left(\mathrm{K}^*+\mathrm{H}^*\right)\left[\psi_m^*(x)\right] = 0 \tag{2.31}$$

Multiply equation (2.30) by $\psi_m^*(x)$ and equation (2.31) by $\psi_n(x)$, and integrate both equations from 0 to 1 to obtain

$$\begin{aligned}&\lambda_n^2 \int_0^1 \psi_m^* \mathrm{M}\left[\psi_n\right] dx + \lambda_n \int_0^1 \psi_m^* \mathrm{C}\left[\psi_n\right] dx + \lambda_n \int_0^1 \psi_m^* \mathrm{G}\left[\psi_n\right] dx + \\ &\int_0^1 \psi_m^* \mathrm{K}\left[\psi_n\right] dx + \int_0^1 \psi_m^* \mathrm{H}\left[\psi_n\right] dx = 0\end{aligned} \tag{2.32}$$

$$\begin{aligned}&\lambda_m^2 \int_0^1 \psi_n \mathrm{M}^*\left[\psi_m^*\right] dx + \lambda_m \int_0^1 \psi_n \mathrm{C}^*\left[\psi_m^*\right] dx + \lambda_m \int_0^1 \psi_n \mathrm{G}^*\left[\psi_m^*\right] dx + \\ &\int_0^1 \psi_n \mathrm{K}^*\left[\psi_m^*\right] dx + \int_0^1 \psi_n \mathrm{H}^*\left[\psi_m^*\right] dx = 0\end{aligned} \tag{2.33}$$

According to the relationship of differential operators and adjoint differential operators, we have

$$\int_0^1 \psi_m^* \mathcal{D}[\psi_n]\, dx = \int_0^1 \psi_n \mathcal{D}^*[\psi_m^*]\, dx \tag{2.34}$$

where $\mathcal{D}$ and $\mathcal{D}^*$ are the differential and adjoint differential operators, respectively. Therefore, equation (2.33) can be written as

$$\begin{aligned}&\lambda_m^2 \int_0^1 \psi_m^* \mathrm{M}[\psi_n]\, dx + \lambda_m \int_0^1 \psi_m^* \mathrm{C}[\psi_n]\, dx + \lambda_m \int_0^1 \psi_m^* \mathrm{G}[\psi_n]\, dx + \\ &\int_0^1 \psi_m^* \mathrm{K}[\psi_n]\, dx + \int_0^1 \psi_m^* \mathrm{H}[\psi_n]\, dx = 0\end{aligned} \tag{2.35}$$

In order to simplify the expressions, the notation M_{mn} is used to represent $\int_0^1 \psi_m^* \mathrm{M}[\psi_n]\, dx$ and so are the others. Equations (2.32) and (2.35) can be represented as

$$(-\frac{\eta}{2} + \mathrm{i}\omega_n)^2 M_{mn} + (-\frac{\eta}{2} + \mathrm{i}\omega_n)(C_{mn} + G_{mn}) + (K_{mn} + H_{mn}) = 0 \tag{2.36}$$

$$(-\frac{\eta}{2} + \mathrm{i}\omega_m)^2 M_{mn} + (-\frac{\eta}{2} + \mathrm{i}\omega_m)(C_{mn} + G_{mn}) + (K_{mn} + H_{mn}) = 0 \tag{2.37}$$

where $(-\frac{\eta}{2} + \mathrm{i}\omega_n) = \lambda_n$ and $(-\frac{\eta}{2} + \mathrm{i}\omega_m) = \lambda_m$. Recall that $\mathrm{G} = 2v\frac{\partial}{\partial x}$ and $\mathrm{H} = \eta v \frac{\partial}{\partial x}$. The relationship between G_{mn} and H_{mn} is

$$H_{mn} = \frac{\eta}{2} G_{mn} \tag{2.38}$$

Substituting equation (2.38) into equations (2.36) and (2.37), we obtain

$$(-\frac{\eta}{2} + \mathrm{i}\omega_n)^2 M_{mn} + (-\frac{\eta}{2} + \mathrm{i}\omega_n) C_{mn} + K_{mn} + \mathrm{i}\omega_n G_{mn} = 0 \tag{2.39}$$

$$(-\frac{\eta}{2} + \mathrm{i}\omega_m)^2 M_{mn} + (-\frac{\eta}{2} + \mathrm{i}\omega_m) C_{mn} + K_{mn} + \mathrm{i}\omega_m G_{mn} = 0 \tag{2.40}$$

Subtracting equation (2.40) multiplied by ω_n from equation (2.39) multiplied by ω_m, we obtain

$$(\omega_m - \omega_n)\left[\left(\frac{\eta^2}{4} + \omega_n\omega_m\right) M_{mn} - \frac{\eta}{2} C_{mn} + K_{mn}\right] = 0 \tag{2.41}$$

The term in the bracket in equation (2.41) has to be zero when $\omega_m \neq \omega_n$. The orthogonal relationship of damped axially moving wire is thus obtained as

$$\left(\frac{\eta^2}{4} + \omega_n\omega_m\right) M_{mn} - \frac{\eta}{2} C_{mn} + K_{mn} = \delta_{mn} R \tag{2.42}$$

where λ_n includes λ_{1n} and λ_{2n}, $\psi_n(x)$ includes $\psi_{1n}(x)$ and $\psi_{2n}(x)$, and $\psi_n^*(x)$ includes $\psi_{1n}^*(x)$ and $\psi_{2n}^*(x)$. When $m = n$, R can be obtained as

$$R = \left(\frac{\eta^2}{4} + \omega_n^2\right) \int_0^1 \psi_n^* \mathrm{M}\left[\psi_n\right] dx - \frac{\eta}{2} \int_0^1 \psi_n^* \mathrm{C}\left[\psi_n\right] dx + \int_0^1 \psi_n^* \mathrm{K}\left[\psi_n\right] dx \tag{2.43}$$

Substituting eigenfunctions, adjoint eigenfunctions, and damped frequencies in equations (2.26), (2.29), and (2.25) into equation (2.43), the solution of R can be obtained as follows

$$R = n^2\pi^2(1 - v^2) - \frac{\eta^2}{4} \tag{2.44}$$

Equation (2.42) can be converted into the inner product form of

$$\left(\frac{\eta^2}{4} + \omega_n\omega_m\right) < \mathrm{M}\psi_n, \bar{\psi}_m^* > -\frac{\eta}{2} < \mathrm{C}\psi_n, \bar{\psi}_m^* > + < \mathrm{K}\psi_n, \bar{\psi}_m^* >= \delta_{mn} R \tag{2.45}$$

When $\eta = 0$, the orthogonal relationship (2.45) is identical to that in [82, 99]. When ψ_m and ψ_m^* are complex conjugate, ψ_m can replace $\bar{\psi}_m^*$ in equation (2.45). However, $< \mathrm{M}\psi_n, \bar{\psi}_m^* > \neq < \mathrm{M}\psi_n, \psi_m >$ when the eigenfunction and adjoint eigenfunction are real functions. This is because the complex conjugate of a real eigenfunction is still the same eigenfunction, not the corresponding adjoint eigenfunction. To apply equation (2.45) generally, $\bar{\psi}_m^*$ should not be changed. In order to make the derivation easier, the integration form of the orthogonal relationship will be used in the rest of this chapter.

2.4.1 Summary and comparison

The orthogonal relationship of eigenfunctions derived in the preceding section indicates that the orthogonality is dependent upon the self-adjoint differential operators, damping factor, and the frequencies of vibration (the imaginary parts of the eigenvalues). The eigenvalues, eigenfunctions and orthogonal relationship derived in previous section are

summarized in the following:

$$
\begin{aligned}
\lambda_{1n} &= \frac{-\eta + \sqrt{\left[\eta^2 - 4n^2\pi^2(1-v^2)\right](1-v^2)}}{2} \\
\lambda_{2n} &= \frac{-\eta - \sqrt{\left[\eta^2 - 4n^2\pi^2(1-v^2)\right](1-v^2)}}{2} \\
\psi_{1n}(x) &= \mathrm{e}^{\frac{\mathrm{i}v\sqrt{\left[4n^2\pi^2(1-v^2)-\eta^2\right](1-v^2)}}{2(1-v^2)}} \sin n\pi x \\
\psi_{2n}(x) &= \mathrm{e}^{\frac{-\mathrm{i}v\sqrt{\left[4n^2\pi^2(1-v^2)-\eta^2\right](1-v^2)}}{2(1-v^2)}} \sin n\pi x
\end{aligned}
$$

$$
\left(\frac{\eta^2}{4} + \omega_n\omega_m\right) M_{mn} - \frac{\eta}{2} C_{mn} + K_{mn} = \delta_{mn} R
$$

If the damping factor η is removed from the eigenvalues and eigenfunctions, these equations will become exactly the same as those in Wickert and Mote's results before being normalized for undamped system [99], which are

$$
\begin{aligned}
\lambda_{1n} &= \mathrm{i}n\pi(1-v^2) \\
\lambda_{2n} &= -\mathrm{i}n\pi(1-v^2) \\
\psi_{1n}(x) &= \mathrm{e}^{\mathrm{i}vn\pi x} \sin n\pi x \\
\psi_{2n}(x) &= \mathrm{e}^{-\mathrm{i}vn\pi x} \sin n\pi x
\end{aligned}
$$

Furthermore, the orthogonal relationship of the undamped system will be identical to that in the previous research [82]. If the damping factor is removed, the orthogonal relationship for an undamped system is

$$
\omega_n\omega_m M_{mn} + K_{mn} = \delta_{mn} R
$$

where $\mathrm{i}\omega_n = \lambda_n$ because the eigenvalues are purely imaginary.

2.5 Free Vibration Response

The orthogonal relationship derived in Section 2.4 is the foundation for the formation of free vibration response for damped axially moving wire. In this section, the free vibration response of damped axially moving wire will be presented.

2.5.1 Analytical solution

As other distributed systems, the free vibration response of damped axially moving wire can be obtained according to the orthogonality and initial conditions. Recall equation (2.27)

$$u(x,t) = \sum_{n=1}^{\infty} \left[D_{1n}\psi_{1n}(x)\mathrm{e}^{\lambda_{1n}t} + D_{2n}\psi_{2n}(x)\mathrm{e}^{\lambda_{2n}t} \right]$$

If the initial displacement of the wire is $a(x)$ and the initial velocity is $b(x)$, the coefficients D_{1n} and D_{2n} are obtained by the following equations (see Appendix A).

$$\begin{aligned} D_{1n} = & \left(\frac{\eta^2}{4}\int_0^1 \psi_{1n}^* \mathrm{M}\left[a(x)\right] dx - \mathrm{i}\omega_{1n} \left(\int_0^1 \psi_{1n}^* \mathrm{M}\left[b(x)\right] dx + \frac{\eta}{2}\int_0^1 \psi_{1n}^* \mathrm{M}\left[a(x)\right] dx \right) \right. \\ & \left. - \frac{\eta}{2}\int_0^1 \psi_{1n}^* \mathrm{C}\left[a(x)\right] dx + \int_0^1 \psi_{1n}^* \mathrm{K}\left[a(x)\right] dx \right) \Big/ R \end{aligned} \tag{2.46}$$

$$\begin{aligned} D_{2n} = & \left(\frac{\eta^2}{4}\int_0^1 \psi_{2n}^* \mathrm{M}\left[a(x)\right] dx - \mathrm{i}\omega_{2n} \left(\int_0^1 \psi_{2n}^* \mathrm{M}\left[b(x)\right] dx + \frac{\eta}{2}\int_0^1 \psi_{2n}^* \mathrm{M}\left[a(x)\right] dx \right) \right. \\ & \left. - \frac{\eta}{2}\int_0^1 \psi_{2n}^* \mathrm{C}\left[a(x)\right] dx + \int_0^1 \psi_{2n}^* \mathrm{K}\left[a(x)\right] dx \right) \Big/ R \end{aligned} \tag{2.47}$$

where $R = n^2\pi^2\left(1 - v^2\right) - \frac{\eta^2}{4}$ is defined in Section 2.4. One comment is worth noting here. When the initial position $a(x)$ is not second differentiable, $a(x)$ and the adjoint eigenfunctions in the terms $\int_0^1 \psi_{1n}^* \mathrm{K}\left[a(x)\right] dx$ and $\int_0^1 \psi_{2n}^* \mathrm{K}\left[a(x)\right] dx$ should be interchanged to avoid a trivial solution. Equations (2.46) and (2.47) can be rewritten as

$$\begin{aligned} D_{1n} = & \left(\frac{\eta^2}{4}\int_0^1 a(x) \mathrm{M}\left[\psi_{1n}^*\right] dx - \mathrm{i}\omega_{1n} \left(\int_0^1 b(x) \mathrm{M}\left[\psi_{1n}^*\right] dx + \frac{\eta}{2}\int_0^1 a(x) \mathrm{M}\left[\psi_{1n}^*\right] dx \right) \right. \\ & \left. - \frac{\eta}{2}\int_0^1 a(x) \mathrm{C}\left[\psi_{1n}^*\right] dx + \int_0^1 a(x) \mathrm{K}\left[\psi_{1n}^*\right] dx \right) \Big/ R \end{aligned} \tag{2.48}$$

$$\begin{aligned} D_{2n} = & \left(\frac{\eta^2}{4}\int_0^1 a(x) \mathrm{M}\left[\psi_{2n}^*\right] dx - \mathrm{i}\omega_{2n} \left(\int_0^1 b(x) \mathrm{M}\left[\psi_{2n}^*\right] dx + \frac{\eta}{2}\int_0^1 a(x) \mathrm{M}\left[\psi_{2n}^*\right] dx \right) \right. \\ & \left. - \frac{\eta}{2}\int_0^1 a(x) \mathrm{C}\left[\psi_{2n}^*\right] dx + \int_0^1 a(x) \mathrm{K}\left[\psi_{2n}^*\right] dx \right) \Big/ R \end{aligned} \tag{2.49}$$

2.5.2 Examples

Examples are given in this section to apply the solution derived in Section 2.5.1. Example 1 involves a damped axial moving wire of a wiresaw system with an initial displacement of $a(x) = 0.02x$ when $0 \leq x < 0.5$ and $a(x) = 0.02(1-x)$ when $0.5 \leq x \leq 1$, and an initial transverse velocity of $b(x) = 0$. The damping factor is $\eta = 1$ with a speed of $v = 0.3$. The vibration response can be obtained by equations (2.27), (2.48), and (2.49).

Figure 2.3 shows the free vibration response of the wire under the prescribed initial conditions. Due to the fact that the given $a(x)$ function is not second differentiable, equations (2.48), and (2.49) should be applied, instead of (2.46) and (2.47). The component n is taken from 1 to 30 in equation (2.27) after several simulation to ensure that the results can represent those of n from 1 to ∞, without undue computational cost.

Example 2 pertains to the free vibration response of damped axially moving wire with an initial displacement of $a(x) = 0.01 \sin \pi x$, and no initial transverse velocity as illustrated in Figure 2.4. The damping factor is $\eta = 1$ with a speed of $v = 0.3$. Because the function of initial displacement is second differentiable, either equations (2.46) and (2.47) or equations (2.48) and (2.49) can be utilized to obtain the coefficients of the response, $u(x,t)$.

The vibration responses of axially moving wire are asymmetric in both examples. In contrast to the symmetric vibration response of a stationary wire, the speed of the moving wire affects the net speed of wave propagation, as discussed in [92, 93]. Therefore, the speeds of wave propagation to the right and to the left are not the same for a moving wire, resulting in asymmetric vibration responses. However, when each wave bounced at the boundaries ($x = 0$ or 1), the speeds of wave propagation are swapped. This can be seen clearly with animation of motions, moving along the 8 plots of responses. These results in the waveform shown in Figures 2.3 and 2.4.

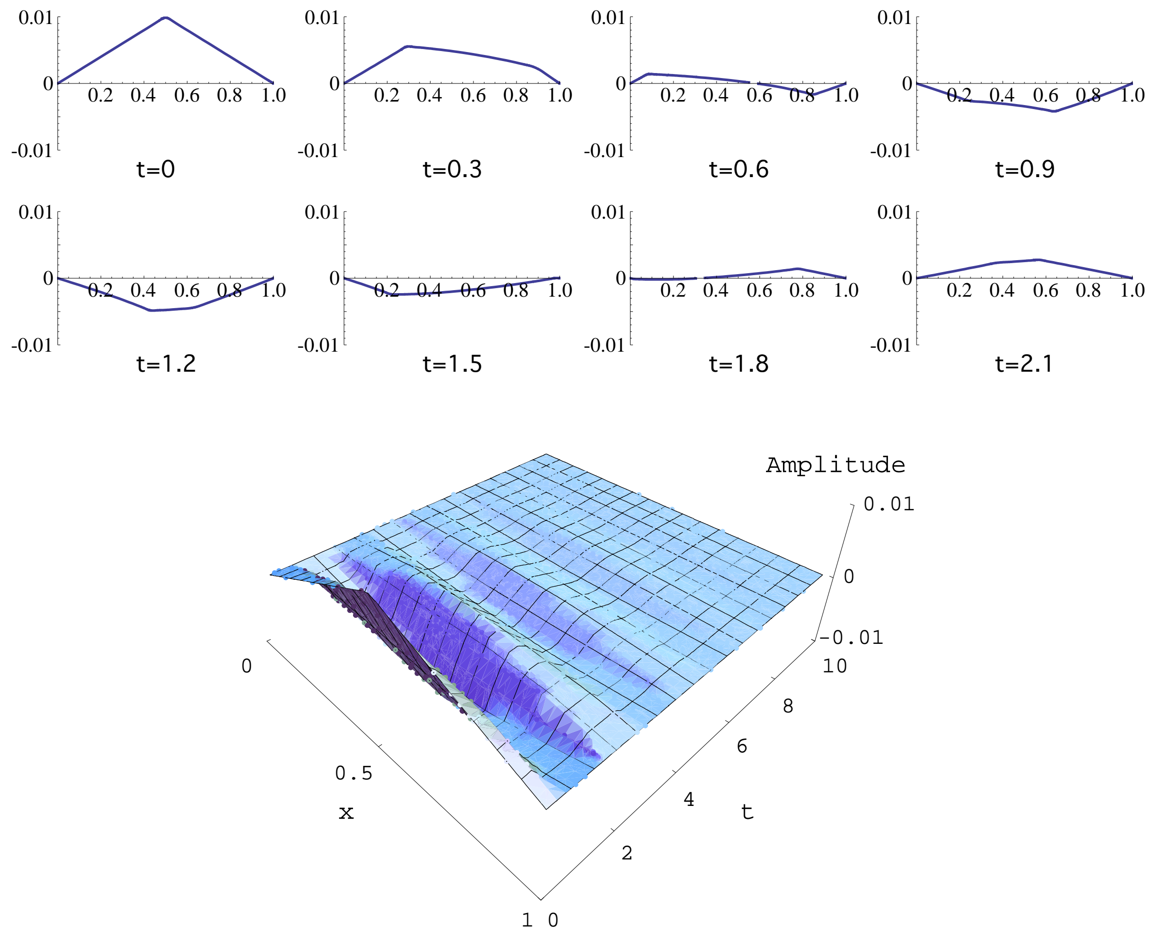

Figure 2.3: Free vibration response of a damped moving wire with $\eta = 1$ and $v = 0.3$. The components n is from 1 to 30, with an initial displacement shown at ($t = 0$)

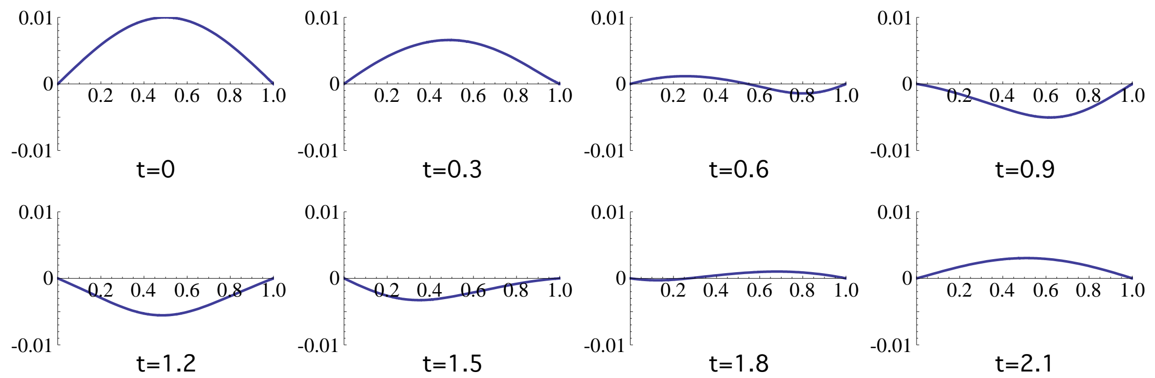

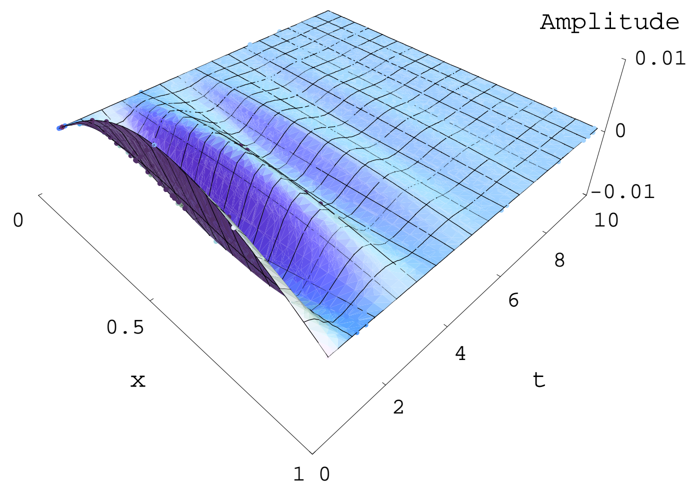

Figure 2.4: Free vibration response of a damped moving wire with $\eta = 1$ and $v = 0.3$. The components n is from 1 to 10, with an initial displacement shown at $(t = 0)$

2.6 Discussion

The analytical form of the free vibration response is obtained in Section 2.5, and illustrated with examples. In this section, the free vibration responses of undamped axially moving wire and damped stationary wire are compared with the solution obtained in Section 2.5 by assuming $\eta = 0$ and $v = 0$, respectively.

2.6.1 Comparison with special cases

Case 1: Undamped axially moving wire

By assuming $\eta = 0$, the damped system will degenerate into an undamped system. The solution of the degenerated system, such as the eigenvalues, eigenfunctions, orthogonal relationship, and coefficients of free vibration response, will be the same as those of the undamped system presented in [82, 99]. Figure 2.5 is the free vibration response of an undamped system under the same initial conditions as those of the Example 2 in Section 2.5.2.

When $\eta = 0$, the eigenvalues become $\lambda_{1n} = \mathrm{i}n\pi(1 - v^2)$ and $\lambda_{2n} = -\mathrm{i}n\pi(1 - v^2)$. The corresponding eigenfunctions are

$$\begin{aligned} \psi_{1n}(x) &= \mathrm{e}^{\mathrm{i}n\pi vx} \sin n\pi x \\ \psi_{2n}(x) &= \mathrm{e}^{-\mathrm{i}n\pi vx} \sin n\pi x \end{aligned}$$

which are identical to the solutions derived by Wickert and Mote [99].

Case 2: Damped stationary wire

If we set $v = 0$ in the damped axially moving wire system discussed earlier, the system becomes a damped stationary wire system, with the differential operators $\mathrm{G} = \mathrm{H} = 0$. Therefore, the equation of motion of damped stationary wire system is self-adjoint which can be solved without considering the adjoint eigenproblem. The eigenvalues and

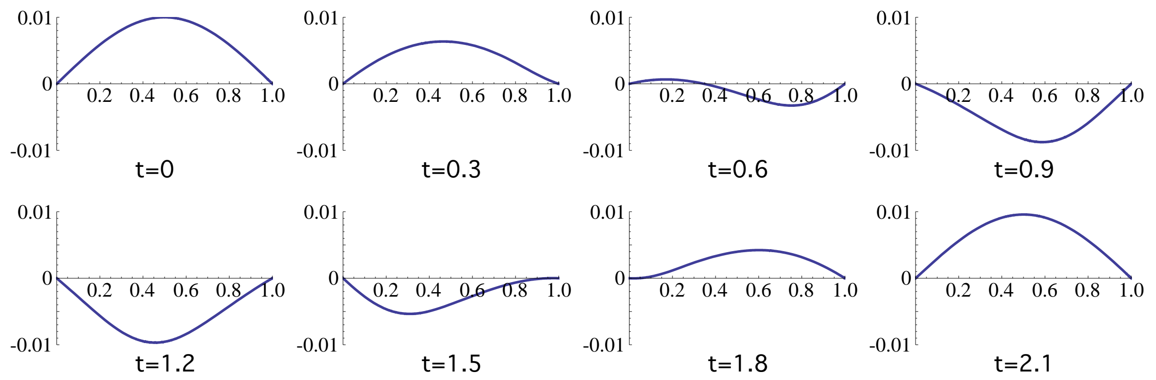

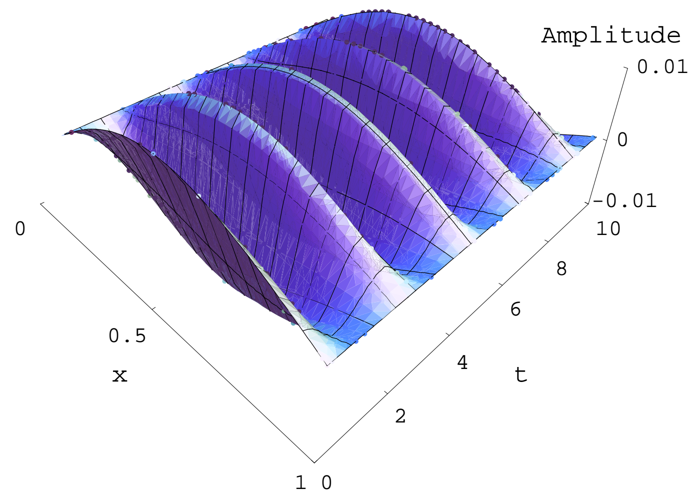

Figure 2.5: Free vibration response of undamped axially moving wire at $v = 0.3$ and $\eta = 0$. The component n is from 1 to 10.

eigenfunctions for such system are

$$\begin{aligned}
\lambda_{1n} &= \frac{-\eta + \mathrm{i}\sqrt{(4n^2\pi^2 - \eta^2)}}{2} \\
\lambda_{2n} &= \frac{-\eta - \mathrm{i}\sqrt{(4n^2\pi^2 - \eta^2)}}{2} \\
\psi_{1n}(x) &= \psi_{2n}(x) = \sin n\pi x
\end{aligned} \tag{2.50}$$

Figure 2.6 shows the simulation of damped stationary wire under the same initial conditions as those of the Example 2 in Section 2.5.2 with $v = 0$ and $\eta = 1$.

2.7 Summary

In this chapter, the closed-form solution of the free vibration response of damped axially moving wire immersed in the slurry is first presented. The complementary eigenvalues, eigenfunctions, resonant frequencies, and orthogonality are also provided. These functions show the consistent with the undamped axially moving wire and damped stationary wire by assuming $\eta = 0$ and $v = 0$, respectively. In Chapter 3, this damped vibration response will be analyzed based on the solutions derived in this chapter.

Because the equation of motion is non-self-adjoint, the orthogonal relationship includes eigenfunctions, differential operators, resonant frequencies, and damping factor. Therefore, the decoupling of forced vibration response using such orthogonal relationship will be a challenge. In Chapter 4, the closed-form solution of the forced vibration response of damped axially moving wire will be obtained by an alternative method using Green's Function.

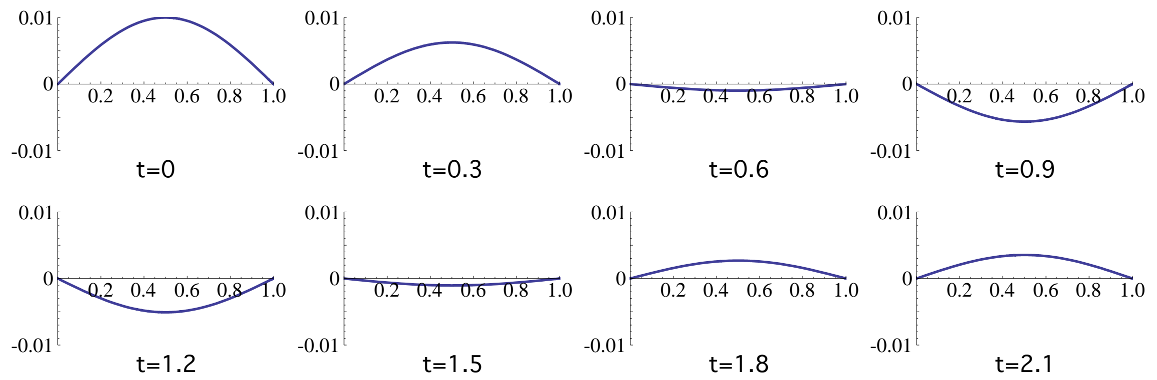

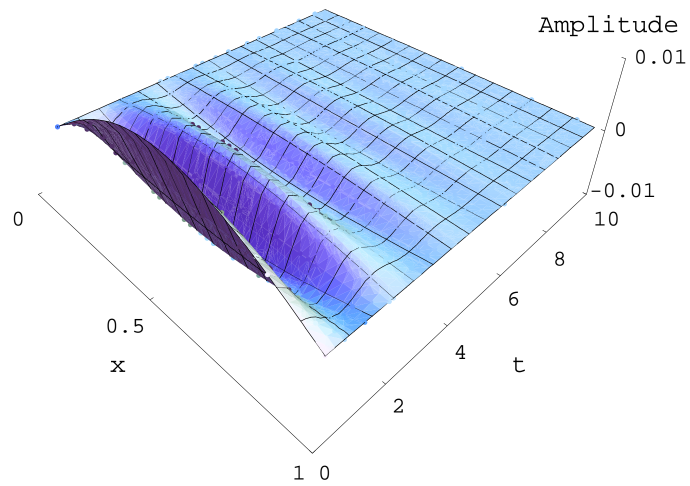

Figure 2.6: Free vibration response of a stationary wire at $\eta = 1$. The component n is from 1 to 10.

Chapter 3

Characteristics of Damped Axially Moving Wire of Slurry Wiresaw System

3.1 Introduction

The closed-form solution of the free vibration response of damped axially moving wire was presented in Chapter 2. In this chapter, the damped vibration response will be analyzed according to the solutions. Two damping ratios will be defined. Since the free vibration response is a combination of infinite sets of solutions, it is not possible for the system to be completely critically-damped or over-damped because of the existence of under-damped modes at higher order. Therefore, a damped index, s, is introduced to help in understanding the behavior of such system.

When physical damping is increased (for example, by using a more viscous carrier fluid in slurry), all components are more damped accordingly. However, in addition to the physical damping, the apparent damping caused by the increase of wire speed will also damp out the response because of the reduction of resonant frequencies. These two parameters, physical damping and apparent damping, control the behavior of an axially moving wire. This is a new finding in vibration analysis of moving wire that, to our best knowledge, has not been reported previously. In addition, the shift of the components of response due to the increase of speed on the first several components of responses will be

presented and discussed in this chapter. The results also show that the increase in speed will excite components of response except the dominating one.

The damping ratios and damping index will be presented in Section 3.2, in which the apparent damping is also discussed. Section 3.3 shows that the mode shapes change with the increase of velocity. The specific relevance to wiresawing process is provided in Section 3.4. The parameter study of damping ratios in wiresaw systems is also provided. A summary of this chapter is given in Section 3.5.

3.2 Analysis of Damped Vibration

In discrete or lumped-parametered systems, damping ratio is an important index to describe the decaying behavior of damped vibration. However, the damping ratio of damped axially moving wire has not been discussed. Based on the analytical solution obtained in Chapter 2, the damping ratio will be defined in this section. The results show that the damping ratio is a function of both axial speed of wire and damping factor, and the increase of speed accompanies the "apparent damping effect."

In a typical second-order one-degree-of-freedom system, the system is called critically damped when the damping ratio $\zeta = 1$, in which the oscillation no longer exists. Therefore, it is intuitive that the frequency of vibration will be zero when the system is critically damped, and the damping ratio, ζ_ω, will be defined. In addition, there is an alternative method to define the damping ratio which is often used in the control theory and one degree-of-freedom vibration system. In this case, the damping ratio, ζ_θ will be defined by the eigenvalues in the complex plane. The details will be illustrated in the following sections.

3.2.1 Damping ratio defined by frequency of vibration

Research has showed that the vibration response will be divergent or unstable when $v \geq 1$ [65, 99]. Therefore, we only consider the case when $v < 1$. The frequency of

damped vibration of a axially moving wire is $\omega_{d,n}$ from equation (2.25).

$$\omega_{d,n} = \frac{\sqrt{\left[4n^2\pi^2(1-v^2) - \eta^2\right](1-v^2)}}{2}$$

When $v < 1$, if λ_{1n} and λ_{2n} are complex conjugate, say $\lambda_n = -\frac{\eta}{2} \pm \mathrm{i}\omega_{d,n}$, the system displays critically damped behavior with double roots when $\omega_{d,n} = 0$: that is,

$$4n^2\pi^2(1-v^2) = \eta^2, \quad n = 1, 2, \ldots$$

or

$$\frac{\eta}{2n\pi}\sqrt{\frac{1}{1-v^2}} = 1$$

Thus, we can define the damping ratio as

$$\zeta_\omega = \frac{\eta}{2n\pi}\sqrt{\frac{1}{1-v^2}}, \quad n = 1, 2, \ldots \tag{3.1}$$

Equation (3.1) defines a damping ratio which is proportional to η but inversely proportional to $\sqrt{1-v^2}$. When $\zeta_\omega = 1$, it corresponds to the case with $\lambda_n = -\frac{\eta}{2}$. When $\zeta_\omega < 1$, it corresponds to the behavior of a underdamped system.

It is obvious from equation (3.1) that the damping ratio, ζ_ω, of damped axially moving wire is dependent on the component number, n, of the free vibration response. The damping ratio, ζ_ω, has to be calculated for each nth component of response to understand the overall vibration response of the damped axially moving wire system. The situation is similar to the multi-dof second-order lumped system. By modal analysis, the multi-dof system can be decoupled into eigenspace. For each decoupled equation, there is a corresponding damping ratio.

In order to depict the damped behaviors of each nth component quickly, a new index, s, is introduced by definding $s = n\zeta_\omega$. From equation (3.1), s can be derived as

$$s = \frac{\eta}{2\pi}\sqrt{\frac{1}{1-v^2}} \quad \text{when} \quad v < 1 \tag{3.2}$$

where s is a function of only η and v. According to the index, s, the damped n^{th} component of response can be described as follows:

(i) When $n < s$, the nth component of response is overdamped.

(ii) When $n = s$, the nth component of response is critical damped.

(iii) When $n > s$, the nth component response is underdamped.

When $v < 1$, as n goes from 1 to ∞, there are finite number of nth components of response which are overdamped and critically damped, with higher-order components kept as underdamped. Since vibration response is a combination of infinite number of components from $n = 1, \ldots, \infty$, the system with $v < 1$ will always display underdamped modes of vibration, regardless of the associated amplitudes of such underdamped vibration modes.

For example, if $s = 2.5$, the first and second components of response, $u_1(x, t)$ and $u_2(x, t)$, are overdamped, and the other higher-order components of response are underdamped.

3.2.2 Damping ratio defined by the complex eigenvalues

When eigenvalues are complex with $\lambda = -\sigma \pm \mathrm{i}\omega$, the response is an exponentially decaying harmonic response with the exponentially decaying envelop defined by $\mathrm{e}^{-\sigma t}$. The damping ratio is defined by the ratio between the real and imaginary parts of the eigenvalue: that is, $\zeta = \cos\theta = \frac{\sigma}{\sqrt{\sigma^2+\omega^2}}$.

Similarly, the solutions of λ_{1n} and λ_{2n} presented here have a corresponding damping ratio defined by the real and imaginary parts of the eigenvalues on complex plane as shown in Figure 3.1. As indicated in Figure 3.1, θ is the angle between negative real axis and the vector from origin to the eigenvalue. The damping ratio is defined as

$$\begin{aligned}
\zeta_\theta &= \cos\theta \\
&= \frac{\frac{\eta}{2}}{\sqrt{\left(\frac{\eta}{2}\right)^2 + \left(\frac{\sqrt{[4n^2\pi^2(1-v^2)-\eta^2](1-v^2)}}{2}\right)^2}} \\
&= \frac{\eta}{\sqrt{4n^2\pi^2\left(1-v^2\right)^2 + \eta^2 v^2}} \qquad (3.3)
\end{aligned}$$

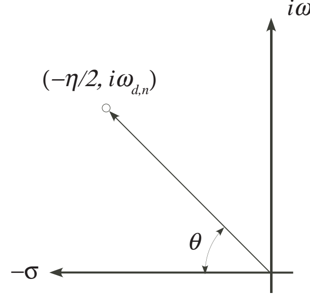

Figure 3.1: Complex eigenvalue and the definition of damping ratio on the complex plane. The complex conjugate of the eigenvalue is not shown in the figure.

The definition of ζ_θ in equation (3.3) is different from ζ_ω. For the situation of stationary wire, $\zeta_\omega = \zeta_\theta$ at $v = 0$. However, when v approaches 1, ζ_ω approaches ∞; whereas ζ_θ approaches 1, implying that the system is close to critically damped. According to equation (2.25), $\omega_{d,n} = 0$ at $v = 1$. Therefore, ζ_θ is preferred to determine the damping ratio of damped axially moving wire. Nevertheless, the damping index, s, derived from ζ_ω is still an efficient tool to evaluate the damped behavior, which will be discussed in the following sections.

3.2.3 Comparison of ζ_ω and ζ_θ

Two damping ratios ζ_ω and ζ_θ are defined based on different observations of the solution of the complex eigenvalues and vibration response. In this subsection, they will be discussed as functions of v and η separately.

Damping ratio as a function of velocity:

Figures 3.2 illustrates the damping ratios as a function of the non-dimensionalized speed v, and offers comparison between the two definitions of damping ratios. In Figure 3.2(a), the system is underdamped when $v = 0$. With the increase of v, both ζ_ω and ζ_θ increase and intersect at $\zeta_\omega = \zeta_\theta = 1$. The corresponding speed can be solved from both equations (3.1) and (3.3), which yield the same result in the following equation:

$$v_{cr} = \sqrt{1 - \frac{\eta^2}{4n^2\pi^2}}, \qquad \text{when } \zeta_\omega = \zeta_\theta = 1 \tag{3.4}$$

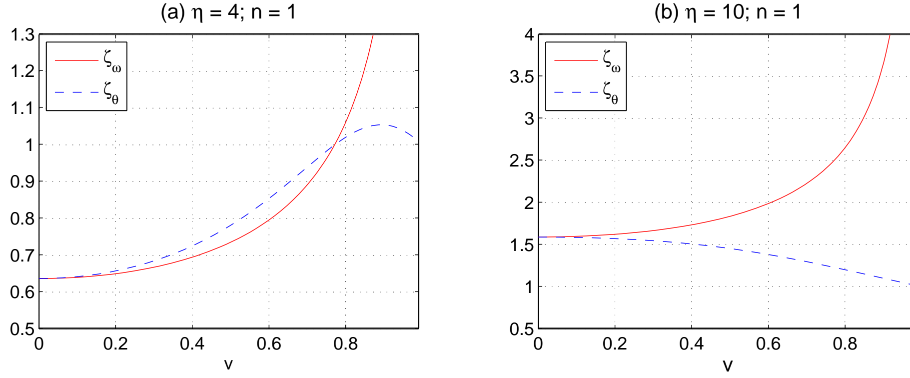

Figure 3.2: Damping ratio ζ_ω and ζ_θ (solid and dashed curves) as a function of v for the first component of response ($u_1(x,t)$ with $n = 1$). The damping factors are (a) $\eta = 4$ and (b) $\eta = 10$

Based on equation (3.4), when $v > \sqrt{1 - \frac{\eta^2}{4n^2\pi^2}}$, both ζ_ω and ζ_θ are greater than 1, implying an overdamped system. Therefore, when the nth component of response is overdamped, either ζ_ω or ζ_θ will be greater than 1. As a result, the overdamped components of response predicted by the damping index, s, still work with damping ratio ζ_θ. However, ζ_θ drops to 1 while $\zeta_\omega \to \infty$ as $v \to 1$.

In this case, there is an apparent increase of damping in free vibration response with increasing speed and constant damping factor η. We call this effect the "apparent damping effect." Figure 3.3 shows an example.

In Figure 3.2(b), the system is overdamped at $v = 0$. When v increases, ζ_ω goes to infinity while ζ_θ drops to 1 as the case in underdamped system. The two damping ratios are always over 1 when v is from 0 to 1. Therefore, this system is always overdamped.

Damping ratio as a function of damping factor:

Figure 3.4 shows the damping ratios as functions of damping factor. It is obviously that ζ_ω is linear with the damping factor, which is also shown in equation (3.1). Meanwhile, ζ_θ will approach η/v when the damping factor keep increasing. As discussed in the previous subsection, ζ_ω and ζ_θ intersect at 1. The critical damping factor will be

$$\eta_{cr} = 2n\pi\sqrt{1 - v^2}, \qquad \text{when } \zeta_\omega = \zeta_\theta = 1 \tag{3.5}$$

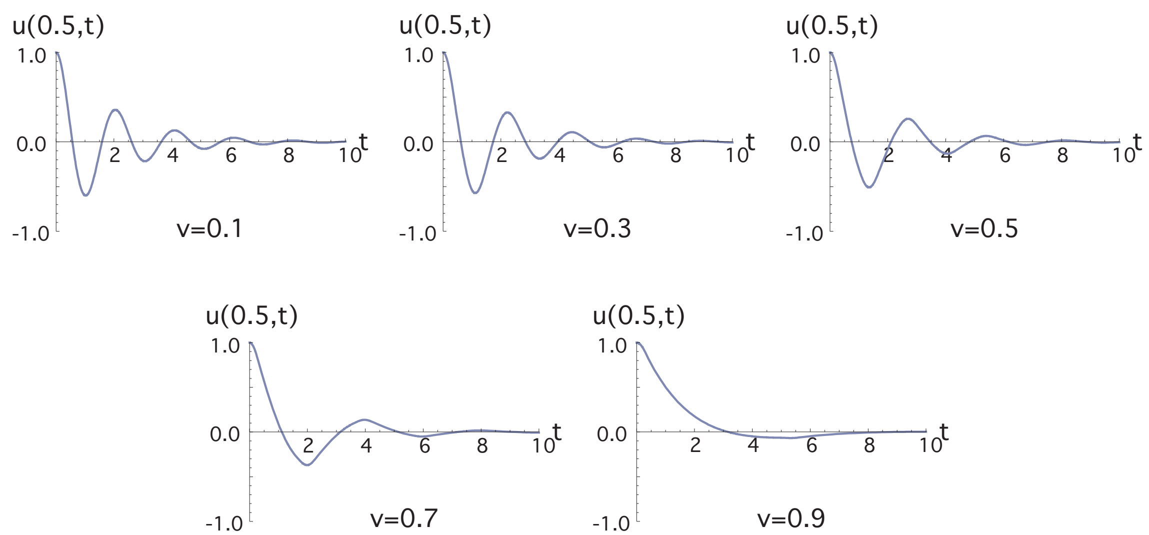

Figure 3.3: Apparent damping effect of free vibration response at $x = 0.5$(center of span) with $\eta = 1$, initial displacement $\sin \pi x$, and no initial velocity (that is, initially at rest).

Therefore, the critical damping factor will decrease when the velocity increases as shown in equation (3.5).

3.2.4 Physical and apparent damping

The free vibration responses of an axially moving wire with different damping factors η under the same wire speed $v = 0.3$ are plotted in Figure 3.5 for comparison. In Figure 3.5(a), the vibration responses of the entire wire span ($0 \leq x \leq 1$) with different damping factors, $\eta = 0.5$ and $\eta = 2.0$, are plotted with discrete time. The vibration responses as a function of time in the middle of the wire at $x = 0.5$ are plotted in Figure 3.5(b). Both Figures 3.5(a) and 3.5(b) show more amplitude reduction with larger damping factor η, as expected. According to the eigenvalues obtained in the previous section, the vibration decaying rate is $\mathrm{e}^{-\frac{\eta}{2}t}$. The two frequencies of vibration, ω_d, for $\eta = 0.5$ and 2.0 are nearly the same.

The free vibration responses in Figure 3.6 are plotted with different wire speeds v under the same damping factor $\eta = 1$. Figure 3.6(a) shows the vibration response of the entire wire span ($0 \leq x \leq 1$) at discrete time. Figure 3.6(b) illustrates the motion in the middle of the wire at $x = 0.5$. It can be observed from the responses in Figure 3.6(a) that a full cycle is elapsed when $v = 0.1$ from $t = 0$ to 2. Within the same time period, however, only half cycle is elapsed for $v = 0.7$. Therefore, the amplitude of oscillation is also reduced with the increase of speed v within a cycle, as shown in Figure 3.6(b). However, such decrease in each cycle of vibration is not a result of reduction of the exponentially decaying envelop because η is kept the same. Instead, the reduction of amplitudes of vibration per each cycle is due to the reduction in frequency, as shown in Figure 3.6(b). Equation (2.25) expresses the frequency of vibration as a function of the wire speed. At $v = 0.7$ and 0.1, the frequencies of their first components are $\omega_{d,1} = 1.562$ and 3.070, respectively. At a lower frequency of vibration for $v = 0.7$ shown with the dashed line in Figure 3.6(b), the amplitude of the first valley at $t \approx 2$ is smaller than that of $v = 0.1$ at $t \approx 1$.

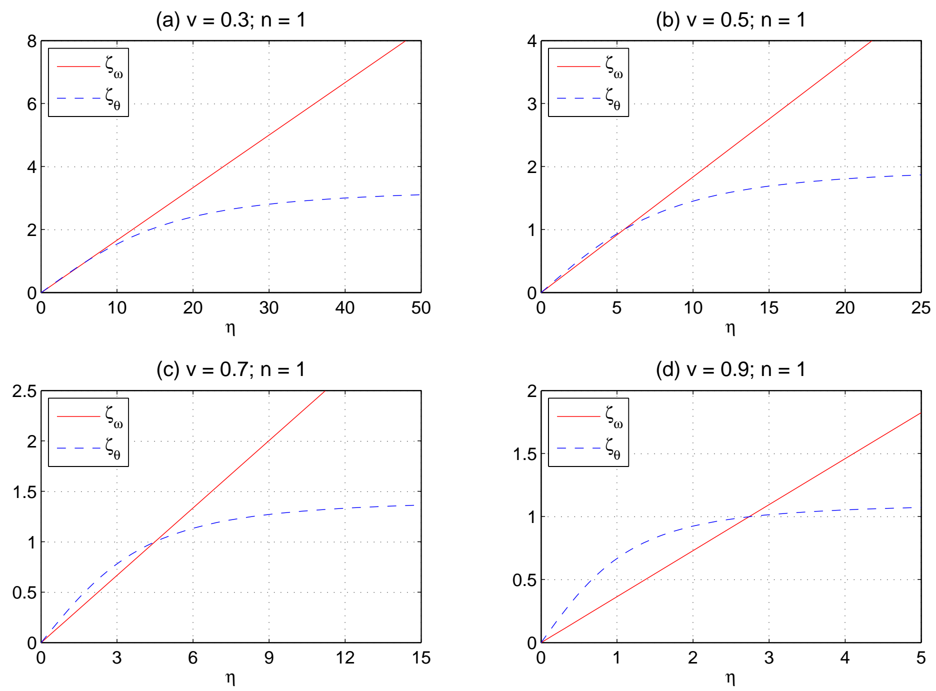

Figure 3.4: damping ratio as a function of damping factor, η.

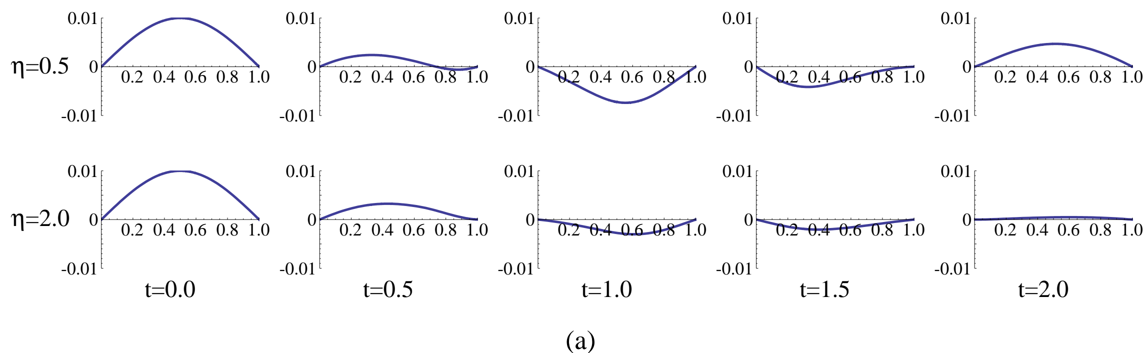

(a)

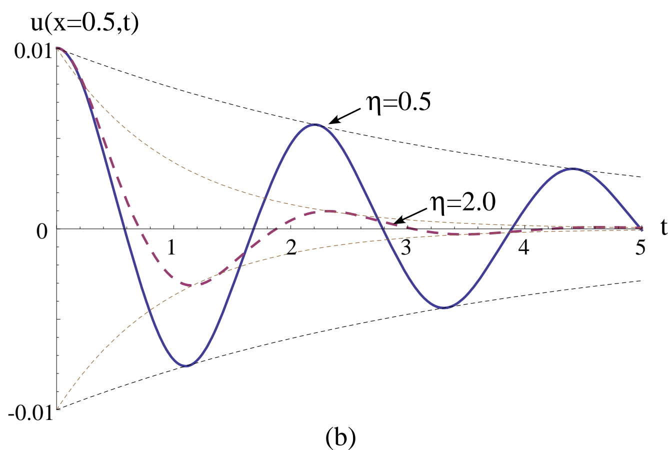

(b)

Figure 3.5: (a) Free vibration response of the entire wire span ($0 \leq x \leq 1$) with different damping factors $\eta = 0.5$ and $\eta = 2.0$. The nondimensionalized speed of wire v is kept at 0.3. The component n is from 1 to 10. (b) The continuous vibration responses at the middle of the wire ($x = 0.5$) are plotted for $\eta = 0.5$ and $\eta = 2.0$. As expected, the exponentially decaying envelop, $\mathrm{e}^{-\frac{\eta}{2}t}$, reduces faster with larger η value. The two responses have nearly identical frequencies of vibration.

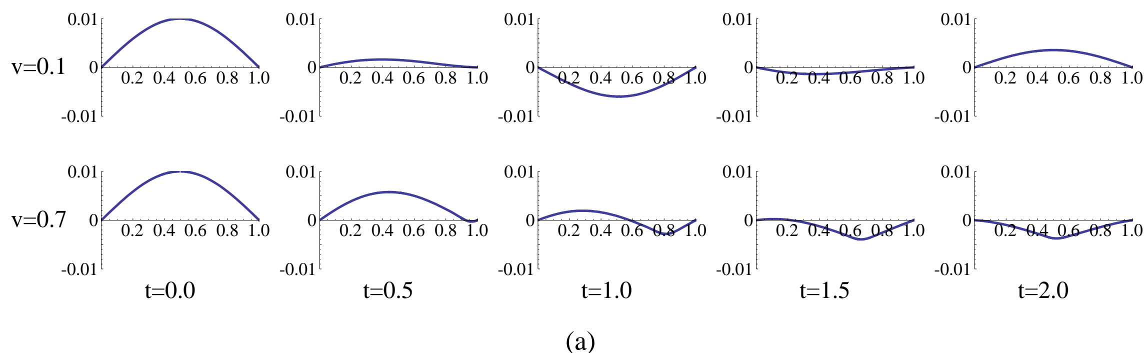

(a)

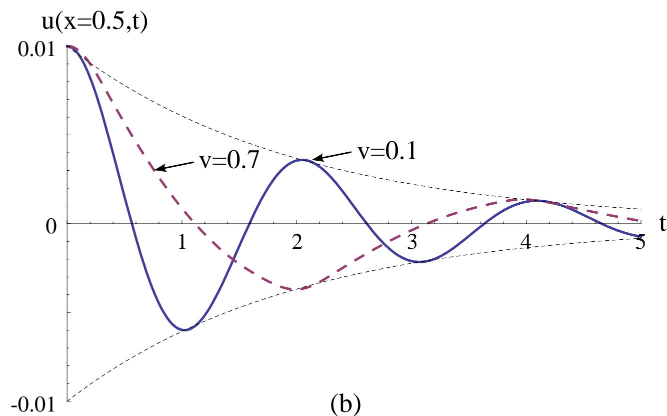

(b)

Figure 3.6: (a) Free vibration response of the entire wire span ($0 \leq x \leq 1$) with different velocities $v = 0.1$ and $v = 0.7$. The nondimensionalized damping factor η is kept at 1. The component n is from 1 to 10. At $v = 0.1$, a full cycle is elasped from $t = 0 \sim 2$ seconds. On the other hand, only half cycle is elapsed for $v = 0.7$ during the same time period. (b) The reduction of amplitude of vibration for $v = 0.7$ is due to a slower frequency of vibration, as illustrated in (a).

3.3 Mode Shape and n^{th} Component of Response

In gyroscopic systems, the eigenfunctions or eigenvectors are complex functions or vectors. Either the real parts or the imaginary parts of eigenfunctions will affect the free vibration response. However, the vibration response should not be complex in reality, which means that the imaginary parts of the vibration response of the solution will cancel each other. In this section, the mode shape and the nth component of response are studied with the increase of wire speed. The results also show the imaginary parts are disappearing in the components of response.

3.3.1 Mode shape

The eigenfunctions of damped axially moving wire were solved as complex functions in the previous chapter. The real modes of the eigenfunctions are

$$\psi_{real}(x) = \cos\frac{v\omega x}{1-v^2}\sin n\pi x \qquad n = 1, 2, 3, \ldots \tag{3.6}$$

and the imaginary modes are

$$\psi_{imag}(x) = \sin\frac{v\omega x}{1-v^2}\sin n\pi x \qquad n = 1, 2, 3, \ldots \tag{3.7}$$

where

$$\omega = \omega_{d,n} = \frac{\sqrt{\left(4n^2\pi^2\left(1-v^2\right)-\eta^2\right)\left(1-v^2\right)}}{2}$$

Figure 3.7 illustrates how the real and imaginary modes change with the increase of wire speed, v. It shows that only real modes exist at $v = 0$. This explains that the stationary wire only has real modes, $\sin n\pi x$. With the increase of wire speed, the imaginary modes are excited and affect the vibration response.

3.3.2 The nth response as a function of the speed

In this subsection, we discuss the nth component of response as a function of speed. Unlike the stationary system, the solutions of axially moving system change with the axial

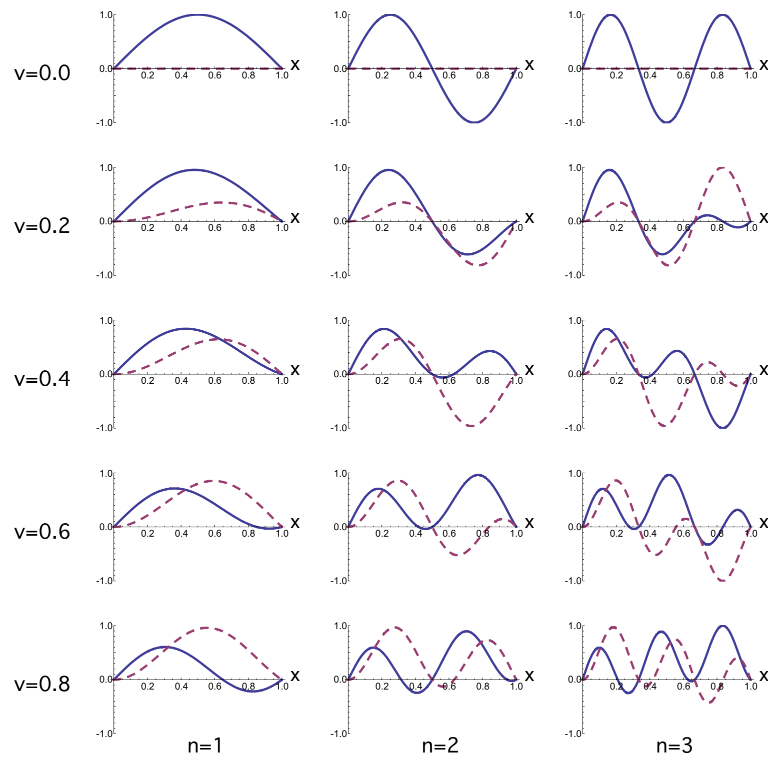

Figure 3.7: Mode shapes of real (real line) and imaginary (dashed line) modes of first three modes.

speed of the wire accompanied by the apparent damping effect. We illustrate the results of the free vibration response with sinusoidal initial conditions. Simulation and calculation of the results are plotted for analysis and discussions.

Although the eigensolutions are complex, the nth component of response, $u_n(x,t)$, in equation (2.27) is a real function to represent the physical system of damped axially moving wire. However, the eigenfunctions, $\psi_{1n}(x)$ and $\psi_{2n}(x)$, of the solutions are not pure real functions. They comprise a new set of complex functions which can represent the vibration response of damped axially moving wire with the eigenvalues and the initial conditions. The nth response of free vibration for an initial displacement of $\sin m\pi x$ and initial transverse velocity of zero can be calculated and plotted based on the analytical solution obtained in Chapter 2. The solution of each component of response in equation (2.27) is as following

$$
\begin{aligned}
u_n(x,t) = E_1\, \mathrm{e}^{-\frac{\eta t}{2}} \Bigg(& E_2 \cos\frac{v\omega x}{1-v^2}\, \sin n\pi x\, \cos\omega t \\
& + E_3 \cos\frac{v\omega x}{1-v^2}\, \sin n\pi x\, \sin\omega t + E_4 \sin\frac{v\omega x}{1-v^2}\, \sin n\pi x\, \cos\omega t \\
& + E_5 \sin\frac{v\omega x}{1-v^2}\, \sin n\pi x\, \sin\omega t \Bigg)
\end{aligned}
$$

where E_1, E_2, E_3, E_4, and E_5 are coefficients and can be represented in the following

equations

$$
\begin{aligned}
E_1 &= \left(4mn\pi^2 v\left(-1+v^2\right)^3\omega\right) \Big/ \left(4n^2\pi^2\left(-1+v^2\right)+\eta^2\right) \\
&\quad \Big[m^4\pi^4\left(-1+v^2\right)^4 + \left(n^2\pi^2\left(-1+v^2\right)^2 - v^2\omega^2\right)^2 \\
&\quad -2m^2\pi^2\left(-1+v^2\right)^2\left(n^2\pi^2\left(-1+v^2\right)^2+v^2\omega^2\right)\Big] \\
E_2 &= -E_5 \\
&= 2\eta\omega - \cos m\pi\,\cos n\pi\left(2\eta\omega\,\cos\frac{v\omega}{-1+v^2}\right. \\
&\quad \left. + \left(4m^2\pi^2\left(-1+v^2\right)+\eta^2\right)\sin\frac{v\omega}{-1+v^2}\right) \\
E_3 &= E_4 \\
&= 4m^2\pi^2\left(-1+v^2\right)+\eta^2-\cos m\pi\,\cos n\pi \\
&\quad \left(\left(4m^2\pi^2\left(-1+v^2\right)+\eta^2\right)\cos\frac{v\omega}{-1+v^2} - 2\eta\omega\,\sin\frac{v\omega}{-1+v^2}\right)
\end{aligned}
$$

The sum of all components, $u_n(x,0)$ at $t = 0$ for $n = 1$ to ∞, will be the initial displacement, $\sin m\pi x$. The results of simulation are presented in Figures 3.8 to 3.10. When $v = 0$, the nth component will dominate the free vibration response, and the other components will vanish when $n = m$. This is illustrated in Figures 3.8 to 3.10 for initial displacement of $\sin \pi x$, $\sin 2\pi x$, and $\sin 3\pi x$, respectively. We call those components which have shape with corresponding initial displacement the dominating components of response. However, the vibration of moving wire exhibits shrinking dominate components as the speed v increasing. With respect to different initial conditions, it is shown in Figures 3.8 to 3.10 that the components other than the dominating component (eg., u_1 is the dominating component for initial displacement $\sin \pi x$, u_2 is for $\sin 2\pi x$, $\ldots$etc.) have increased amplitude of oscillation when v becomes larger.

As the amplitudes of the components change with v, the dominating component shrinks which means that the vibration energy shifts from the dominating frequency to the others. Figures 3.8 to 3.10 show such shifting phenomena. The effect of such phenomena in Figures 3.9 and 3.10 is more pronounced. Though Figures 3.8 to 3.10 illustrates only the

first three components of response with initial displacement of $\sin \pi x$, $\sin 2\pi x$, and $\sin 3\pi x$, the observations presented here can be extended to higher order components.

3.4 Relevance to Slurry Wiresaw Systems

3.4.1 Reynolds number and drag force in wiresaw systems

For flow passing through an immersed body, the force due to friction drag is more than the pressure difference when Reynolds number $\mathrm{Re} < 1$. The drag coefficient is $C_D \cong \frac{7}{\mathrm{Re}}$ for a cylinder, the shape of wire [70] [1] . The Reynolds number can be formulated as

$$\mathrm{Re} = \frac{\rho_f D V_{tr}}{\mu} \tag{3.8}$$

where ρ_f and μ are the density and viscosity of fluid, D is the diameter of the wire, $V_{tr} = VU_X + U_T$ is the transverse velocity of the wire.

Polyethylene glycol is a water-soluble carrier for slurry, which has a density of $1.1 \sim 1.2\ \mathrm{g\,cm^{-3}}$. The density of silicon carbide is $3.21\ \mathrm{g\,cm^{-3}}$. Therefore, the density of slurry is $\rho_f = 1491 \sim 1763\ \mathrm{kg\,m^{-3}}$ for the mixing ratios of $0.75 \sim 1.25$ with kg of grit per liter of carrier. The viscosity is $\mu = 200 \sim 1000\ \mathrm{cP}$. In industry applications, different recipes may be used to optimize the slicing process, resulting in different range of parameters.

Since the slope of the wire, U_X, is small, we approximate the transverse speed of the wire as U_T, neglecting the term VU_X. The maximum U_T can be approximated as the product of vibration amplitude of the wire and natural frequency. The amplitude of vibration of the wire is assume to be $25 \sim 150\ \mu\mathrm{m}$ by subtracting wire diameter, $150 \sim 175\ \mu\mathrm{m}$, from the kerf loss, $200 \sim 300\ \mu\mathrm{m}$. The natural frequency of the first component is $2047 \sim 6781\ \mathrm{rad\,s^{-1}}$ with parameters $V = 10 \sim 15\ \mathrm{m\,s^{-1}}$, $\rho = 0.1876\ \mathrm{g\,m^{-1}}$, $P = 20 \sim 35\ \mathrm{N}$, $L = 0.2 \sim 0.5\ \mathrm{m}$ [97]. Therefore, the transverse speed of the wire is $0.0512 \sim 1.017\ \mathrm{m\,s^{-1}}$. The true transverse speed should be smaller than this range due to damping. With

[1] This is not the only equation of the the drag force in fluid flow for a cylinder at small Reynolds number. Other literature such as reference [85] has a different expression. However, the results of analysis are within the same order of magnitude.

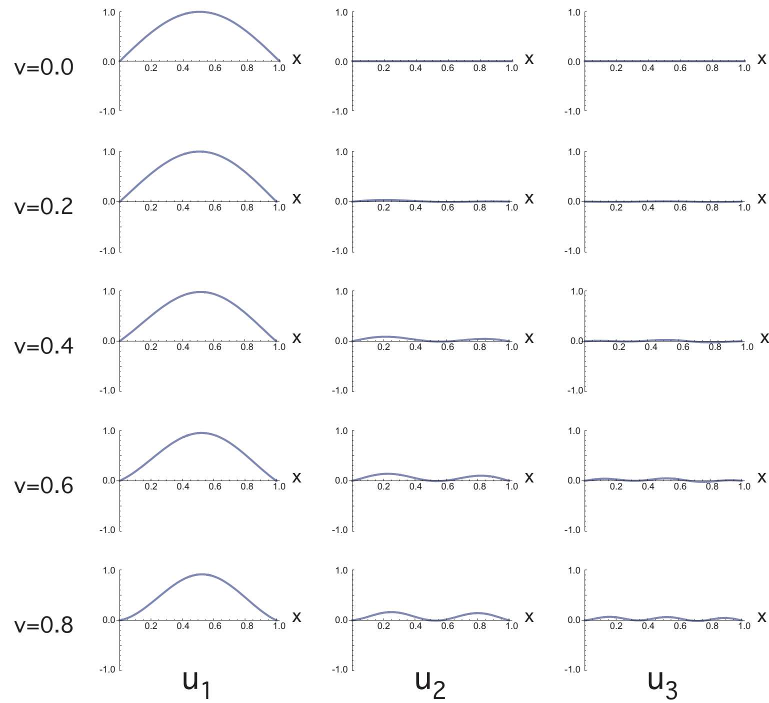

Figure 3.8: The variation of first three components of response with initial displacement $\sin(\pi x)$, initial velocity 0, and damping factor $\eta = 1$.

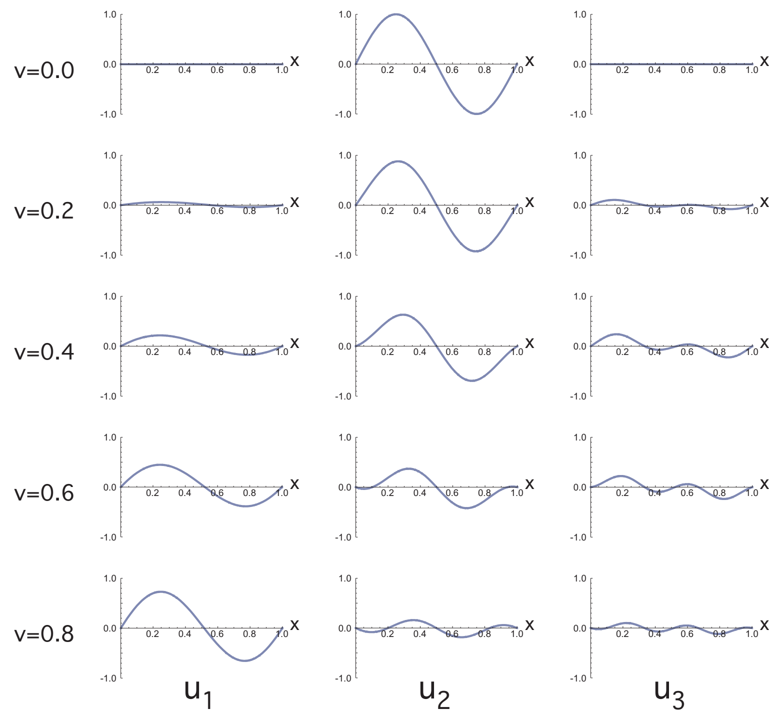

Figure 3.9: The variation of first three components of response with initial displacement $\sin(2\pi x)$, initial velocity 0, and damping factor $\eta = 1$.

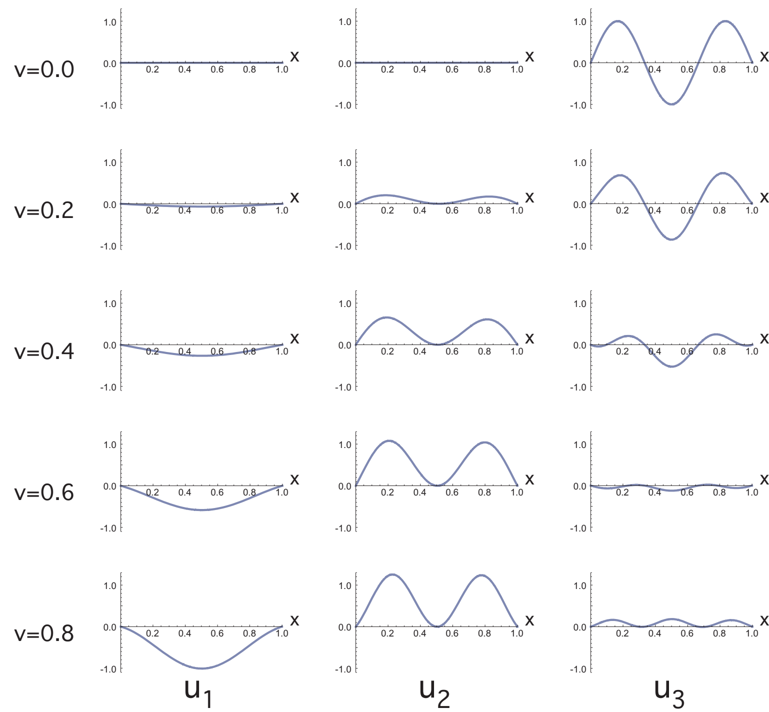

Figure 3.10: The variation of first three components of response with initial displacement $\sin(3\pi x)$, initial velocity 0, and damping factor $\eta = 1$.

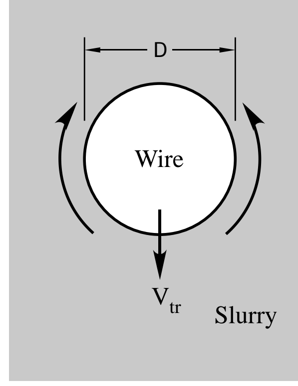

Figure 3.11: Wire motion in slurry with transverse velocity, V_{tr}

these parameters, the Reynolds number in equation (3.8) can be approximate as $0.0115 \sim 1.5688$. Although the range is not always smaller than one, it is still small enough. As a result, we use $C_D \cong \frac{7}{\mathrm{Re}}$ to evaluate the damping factor.

The function due to drag force is $f_D = C_D \frac{\rho_f V_{tr}^2 A}{2}$, where $A = DL$ is the projected area of a cylinder. Because $C_D \cong \frac{7}{\mathrm{Re}}$ and $\mathrm{Re} = \frac{\rho_f D V_{tr}}{\mu}$, the drag force for a cylinder is $f_D = 3.5\mu V_{tr} L$. The damping force per unit length becomes

$$F_\eta = \frac{f_D}{L} \cong 3.5\mu V_{tr}$$

It is also noted that $F_\eta = \eta_d V_{tr}$. Therefore, the damping factor, η_d, can be obtained as

$$\eta_d \cong 3.5\mu \tag{3.9}$$

3.4.2 Practical parameter study

Wiresaw is usually operated under high speed (typically $10 \sim 15\ \mathrm{m\,s^{-1}}$) and high tension ($20 \sim 35$ N). However, the actual non-dimensionalized speed of wire of a wiresaw is far below the critical speed because of its low mass density [97]. With typical process parameters of $V = 10 \sim 15\ \mathrm{m\,s^{-1}}$, $\rho = 0.1876\ \mathrm{g\,m^{-1}}$, $P = 20 \sim 35$ N, and $L = 0.2 \sim 0.5$ m, the non-dimensionalized speed is $v = 0.0232 \sim 0.0459$, much lower than the critical speed at $v = 1$. Therefore, we only have to consider the situation when $v \ll 1$ in wiresawing operations.

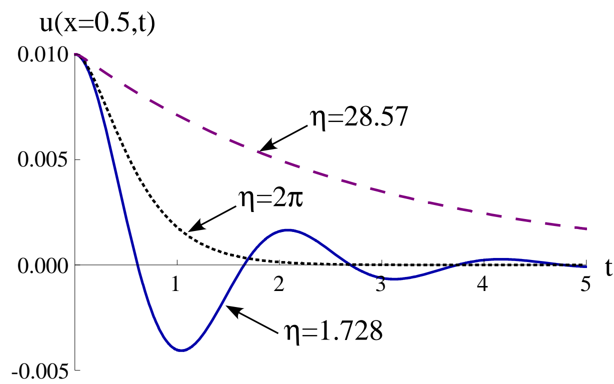

Figure 3.12: Free vibration response with initial displacement $0.01\sin\pi x$ and different damping factors $\eta = 1.728,\ 2\pi,$ and 28.57. The nondimensionalized velocity v is kept at 0.0306. The component n is from 1 to 10. The response at the middle of the wire becomes non-oscillatory when the damping factor $\eta \geq 2\pi$.

Here, we assume that the viscosity of slurry is $200 \sim 1000\,\mathrm{cP}$ [48]. Thus, the approximate range of the damping factor is $\eta_d = 0.7 \sim 3.5\,\mathrm{N\,s\,m^{-2}}$ according to Equation (3.9). The corresponding nondimensionalized damping factor is $\eta = 1.728 \sim 28.57$. Figure 3.12 illustrates the vibration response at the middle point of wire with the initial displacement of $a(x) = 0.01 \sin \pi x$ and no initial transverse velocity. The nondimensionalized velocity and damping factors are corresponding to the wiresaw system discussed earlier with $v = 0.0306$, $\eta = 1.728 \sim 28.57$, respectively. It shows that the typical vibration response of wire is well damped.

3.4.3 Damping ratios

In order to study the damping ratio in slurry wiresaw system, convert the dimensionless parameters into dimensionalized ones.

$$\zeta_\omega = \frac{\eta_d L}{2n\pi}\sqrt{\frac{1}{\rho P - \rho^2 V^2}} \tag{3.10}$$

$$\zeta_\theta = \eta_d L \sqrt{\frac{P}{4n^2\pi^2\rho\left(P - \rho V^2\right)^2 + \eta_d^2 L^2 \rho V^2}} \tag{3.11}$$

When the damping factor approaches infinity, ζ_ω will approach infinity; whereas ζ_θ approaches a constant value, $\sqrt{\frac{P}{\rho V^2}}$. If the first component of free vibration response, u_1, reaches critical damped condition, $\zeta_1 = 1$ can be substituted into equations (3.10) and (3.11) to obtain the damping factor, $\eta_d = 1.28\,\mathrm{N\,s\,m^{-2}}$. This damping factor is not high which is also because of the low density of the wire. Therefore, the damped vibration behavior of the wire in wiresaw system should perform plainly.

In Figure 3.13, 3.14, 3.15, and 3.16, the damping ratios, ζ_ω and ζ_θ, are plotted as a function of damping factor, η_d, in small range. Four parameters, axially moving speed V, tension P, length of wire L, and mass density of wire ρ, are compared in reasonable range of the slurry wiresaw system. All of the four figures show that ζ_ω and ζ_θ do not have obvious difference under small damping factor. The curves of damping ratios for different velocities, $v = 10$, 20, and 30 $\mathrm{m\,s^{-1}}$ are almost the same under small damping factor, η_d,

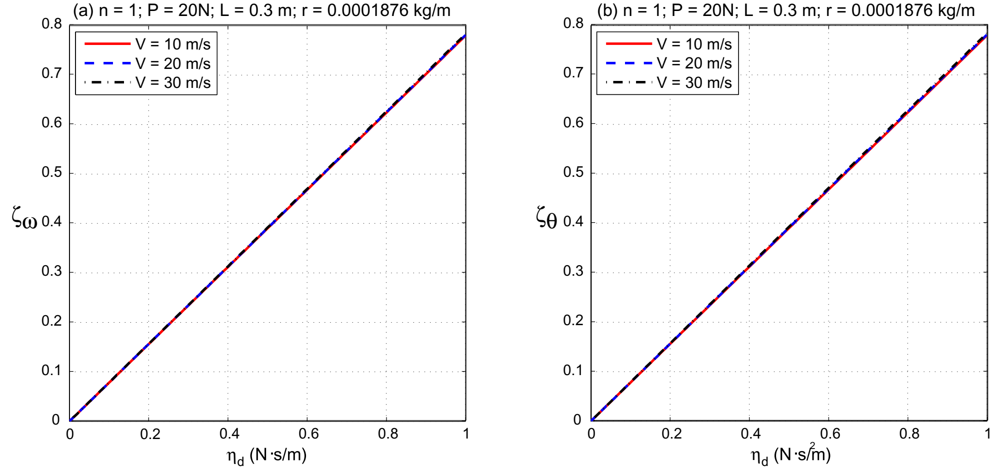

Figure 3.13: Damping ratios as functions of η_d with respective to the axially moving speed of wire in slurry wiresaw system.

as shown in Figure 3.13. The other three figures show higher damping ratio with lower tension, longer wire length, and lower density of the wire.

3.5 Summary

Two damping ratios are defined by the frequency and eigenvalue of damped axially moving wire, respectively. They are discussed and compared with respect to the nondimensionalized parameters v and η separately. The results present the apparent damping effect. In addition, a damping index, s, is also introduced to classify the damping behavior of each component of response of the system.

The mode shape and the nth component of vibration response are studied according to the closed-form solution. The results show that the imaginary modes and compoents of response except the dominating ones are excited with the increase of wire speed.

In a practical slurry-wiresaw system, the speed of the wire is significantly lower than the critical speed. The first component of the free vibration response can reach critical damped condition with quite a small damped factor. Consequently, the wiresaw system is well damped. Method to estimate realistic damping factors for the analysis of damped vi-

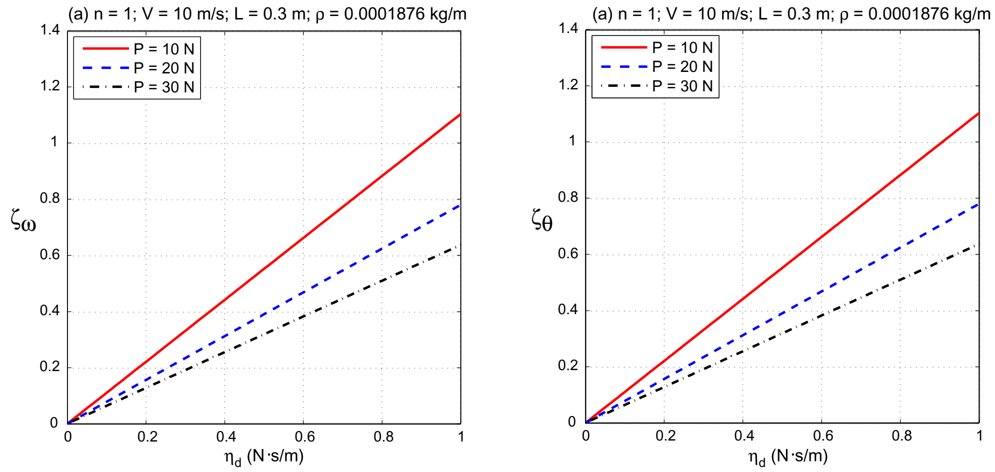

Figure 3.14: Damping ratios as functions of η_d with respective to the tension of wire in slurry wiresaw system.

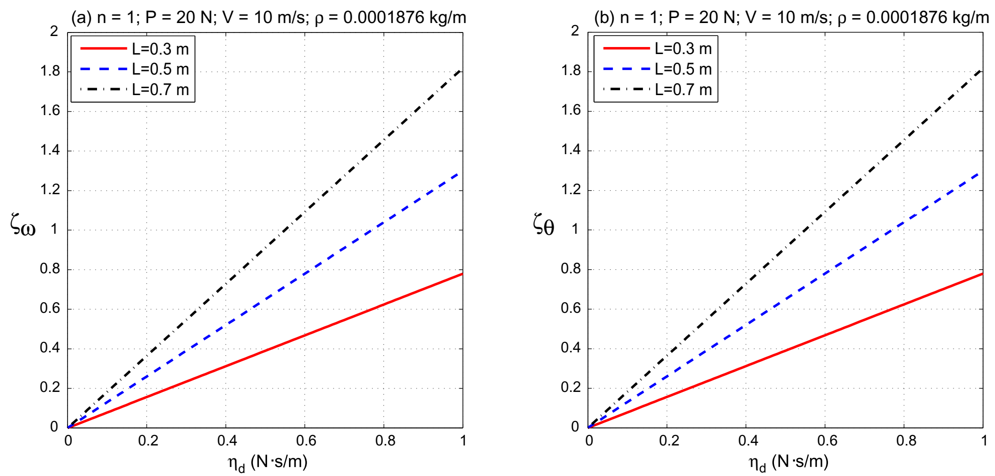

Figure 3.15: Damping ratios as functions of η_d with respective to the length of wire in slurry wiresaw system.

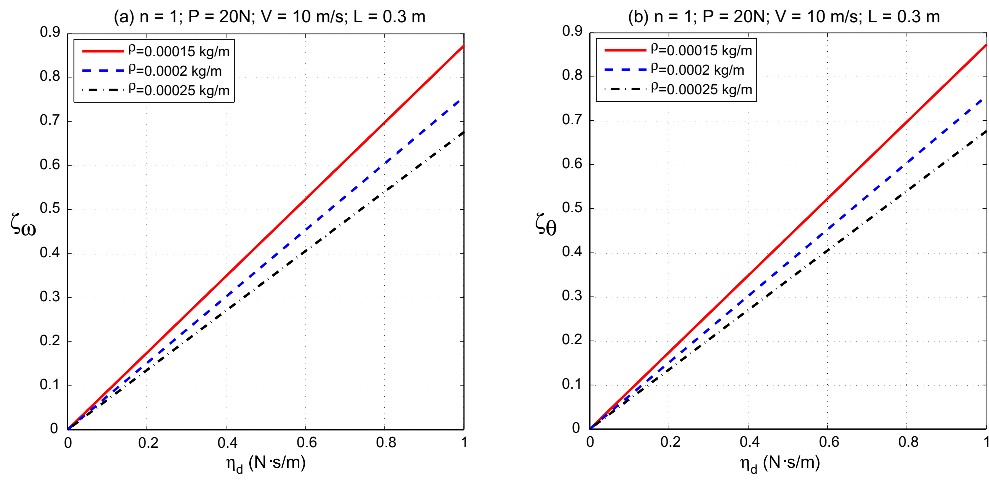

Figure 3.16: Damping ratios as functions of η_d with respective to the mass density of wire in slurry wiresaw system.

bration was presented using typical process parameters of a moving wire in slurry wiresaw systems. In parameter study, the results show that the damping ratio will increase of wire-saw system with lower tension, longer wire length, and lower density of the wire. In order to obtain more characteristics of damped axially moving wire system, the forced vibration response is necessary.

Chapter 4

Green's Function and Forced Vibration Response of Damped Axially Moving Wire

The Green's function of damped axially moving wire is first derived in this chapter. The corresponding frequency response with point excitation is also presented. The results show agreement with previous research on free vibration response and corresponding eigensolutions. The Green's function and frequency response presented in this chapter are essential for control theory and random vibration analysis.

4.1 Introduction

In the study of vibration response, forced vibration is fundamental to describe the response of the system subject to external excitation. Analyses of frequency response, random vibration analysis, and control theory require the knowledge of forced vibration response. In general, the study of forced vibration response of distributed systems is much more complicated than that of lumped-parameter systems. A distributed system involves spatial and temporal variables; therefore, the motion of each point on the system not only depends on the location, but also is a function of time as it vibrates.

To obtain the solution for the distributed system, the equation which describes the spatial relationship is necessary. The solution of modal analysis consists of eigenfuctions and eigenvalues, with the eigenfunctions illustrating the mode shapes of each mode of the

system. The Green's function is the impulse response. It contains not only the response as a function of time, but also describes the relative motion within the system [13, 14, 83].

Axially moving continua has been utilized in many mechanisms or machines such as belts, chains, and saws. During such operations, the surrounding media may give extra resistance which would reduce the oscillation. This resistance may be negligible in some cases. However, for the manufacturing processes such as a wire in slurry wiresaw system or a cable in water, the damping force has to be considered. The vibration responses of axially moving wire and beam without damping have been obtain by Wickert and Mote in 1990 [99]. Yang and Mote presented the Green's function of the axially moving string without damping [103]. The free vibration response of damped axially moving wire was obtain by Chung and Kao [23, 25], and the forced vibration response is still exclusive. Because the equation is non-self-adjoint, the classical modal analysis is not adequate to be employed to solve the forced vibration response.

In this chapter, we present the research results of the Green's function of a damped axially moving wire to obtain the forced vibration response. To our best knowledge, the Green's function derived in this chapter is the first analytical and closed-form solution for **damped** axially moving wire. This new result enables us to obtain forced vibration response of an axially moving wire in a damped environment, such as that in a modern slurry wiresaw [48].

The Green's function of a damped axially moving wire is derived in Section 4.2, followed by the standard form of equations in Section 4.3 and frequency response with point excitation in Section 4.4. The summary is in Section 4.5.

4.2 Green's Function

In Chapter 2, the equation of motion of damped axially moving wire has been introduced and non-dimensionalized as equation (2.14), which is

$$u_{tt} + 2vu_{xt} - (1 - v^2)u_{xx} + \eta v u_x + \eta u_t = f \tag{4.1}$$

The boundary conditions are $u(x,t) = 0$ at $x = 0$ and $x = 1$ [25]. Assume that the Green's function for the differential equation (4.1) is $g(x, \xi, t, \tau)$, which satisfies the following equation [13, 32, 88].

$$g_{tt} + 2vg_{xt} - (1 - v^2)g_{xx} + \eta v g_x + \eta g_t = \delta(x - \xi)\delta(t - \tau) \tag{4.2}$$

where $\delta(x-\xi)$ is a Dirac delta function, which implies that the external force is applied to an arbitrary position ξ within the range of x. Another Dirac delta function $\delta(t - \tau)$ represents an impulse applied at the time $t = \tau$. The boundary conditions are $g(x, \xi, t, \tau) = 0$ at $x = 0$ and $x = 1$. Since this system is stationary linear, which means that this system depends on the difference $(t - \tau)$, the Green's function can be represented in the form $g(x, \xi, t, \tau) = g(x, \xi, t - \tau)$ [13].

The Laplace transform of the Green's function with respect to $t - \tau$ is $\mathcal{L}\{g(x, \xi, t - \tau)\} = G(x, \xi, s)$, and which still satisfies the boundary conditions, $G(x, \xi, s) = 0$ at $x = 0$ and $x = 1$. Assume the initial displacement and initial velocity are zero. Take Laplace transform of the equation of motion (4.2) to obtain

$$s^2 G + 2vs\frac{\partial G}{\partial x} - (1 - v^2)\frac{\partial^2 G}{\partial x^2} + \eta v\frac{\partial G}{\partial x} + s\eta G = \delta(x - \xi)$$

The equation can be written as

$$\frac{\partial^2 G}{\partial x^2} - \frac{v(2s + \eta)}{1 - v^2}\frac{\partial G}{\partial x} - \frac{s^2 + s\eta}{1 - v^2}G = -\frac{\delta(x - \xi)}{1 - v^2} \tag{4.3}$$

When $x \neq \xi$, the right hand-side of the equation should be zero.

$$\frac{\partial^2 G}{\partial x^2} - \frac{v(2s + \eta)}{1 - v^2}\frac{\partial G}{\partial x} - \frac{s^2 + s\eta}{1 - v^2}G = 0, \quad \text{for} \begin{cases} 0 < x < \xi \\ \xi < x < 1 \end{cases} \tag{4.4}$$

Assuming that $G(x, \xi, s) = \mathrm{e}^{\kappa x}$, and substituting it into equation (4.4), we can obtain κ as a function of s.

$$\kappa(s) = \alpha(s) \pm \beta(s) \tag{4.5}$$

where

$$\alpha(s) = \frac{v(2s + \eta)}{2(1 - v^2)}, \text{ and } \beta(s) = \frac{\sqrt{4s^2 + 4s\eta + v^2\eta^2}}{2(1 - v^2)} \tag{4.6}$$

Comparing to the modal analysis, we find that s is actually the eigenvalue of this system and will be solved later. Therefore,

$$\begin{aligned} G^{-}(x,\xi,s) &= \mathrm{e}^{\alpha x}\left(A\mathrm{e}^{\beta x}+B\mathrm{e}^{-\beta x}\right) \quad \text{for } 0<x<\xi \\ G^{+}(x,\xi,s) &= \mathrm{e}^{\alpha x}\left(C\mathrm{e}^{\beta x}+D\mathrm{e}^{-\beta x}\right) \quad \text{for } \xi<x<1 \end{aligned}$$

To satisfy the boundary conditions, $G(x,\xi,s)=0$ at $x=0$ and $x=1$. The coefficients have the following relationships

$$B=-A, \text{ and } D=-C\mathrm{e}^{2\beta}$$

Hence,

$$\begin{aligned} G^{-}(x,\xi,s) &= A\mathrm{e}^{\alpha x}\left(\mathrm{e}^{\beta x}-\mathrm{e}^{-\beta x}\right) \quad \text{for } 0<x<\xi \\ G^{+}(x,\xi,s) &= C\mathrm{e}^{\alpha x}\left(\mathrm{e}^{\beta x}-\mathrm{e}^{2\beta}\mathrm{e}^{-\beta x}\right) \quad \text{for } \xi<x<1 \end{aligned}$$

The function $G(x,\xi,s)$ is continuous at $x=\xi$. Therefore,

$$A\mathrm{e}^{\alpha\xi}\left(\mathrm{e}^{\beta\xi}-\mathrm{e}^{-\beta\xi}\right)=C\mathrm{e}^{\alpha\xi}\left(\mathrm{e}^{\beta\xi}-\mathrm{e}^{2\beta}\mathrm{e}^{-\beta\xi}\right) \tag{4.7}$$

Integrate equation (4.3) with respect to x, and assume that the integral range is very small around ξ to obtain

$$\left.\frac{\partial G}{\partial x}\right|_{\xi^-}^{\xi^+}=-\frac{1}{1-v^2} \tag{4.8}$$

Substitute G^- and G^+ into the equation (4.8) to obtain

$$\begin{aligned} &C\alpha\mathrm{e}^{\alpha\xi}\left(\mathrm{e}^{\beta\xi}-\mathrm{e}^{2\beta}\mathrm{e}^{-\beta\xi}\right)+C\beta\mathrm{e}^{\alpha\xi}\left(\mathrm{e}^{\beta\xi}+\mathrm{e}^{2\beta}\mathrm{e}^{-\beta\xi}\right)-A\alpha\mathrm{e}^{\alpha\xi}\left(\mathrm{e}^{\beta\xi}-\mathrm{e}^{-\beta\xi}\right) \\ &-A\beta\mathrm{e}^{\alpha\xi}\left(\mathrm{e}^{\beta\xi}+\mathrm{e}^{-\beta\xi}\right)=-\frac{1}{1-v^2} \end{aligned} \tag{4.9}$$

According to equations (4.7) and (4.9), the coefficients A and C can now be solved as

$$\begin{aligned} A &= \frac{1}{1-v^2}\frac{\mathrm{e}^{\beta\xi}-\mathrm{e}^{2\beta}\mathrm{e}^{-\beta\xi}}{2\beta\mathrm{e}^{\alpha\xi}\left(1-\mathrm{e}^{2\beta}\right)} \\ C &= \frac{1}{1-v^2}\frac{\mathrm{e}^{\beta\xi}-\mathrm{e}^{-\beta\xi}}{2\beta\mathrm{e}^{\alpha\xi}\left(1-\mathrm{e}^{2\beta}\right)} \end{aligned}$$

We can now obtain the Laplace transform of the Green's function

$$G(x,\xi,s)=\begin{cases}\frac{1}{1-v^2}\frac{\mathrm{e}^{\beta\xi}-\mathrm{e}^{2\beta}\mathrm{e}^{-\beta\xi}}{2\beta\mathrm{e}^{\alpha\xi}\left(1-\mathrm{e}^{2\beta}\right)}\mathrm{e}^{\alpha x}\left(\mathrm{e}^{\beta x}-\mathrm{e}^{-\beta x}\right), & \text{for } 0<x<\xi\\ \frac{1}{1-v^2}\frac{\mathrm{e}^{\beta\xi}-\mathrm{e}^{-\beta\xi}}{2\beta\mathrm{e}^{\alpha\xi}\left(1-\mathrm{e}^{2\beta}\right)}\mathrm{e}^{\alpha x}\left(\mathrm{e}^{\beta x}-\mathrm{e}^{2\beta}\mathrm{e}^{-\beta x}\right), & \text{for } \xi<x<1\end{cases}$$

which can be rearranged and written as

$$G(x,\xi,s)=\begin{cases}\frac{1}{1-v^2}\mathrm{e}^{\alpha(x-\xi)}\frac{\sinh\beta(1-\xi)\sinh\beta x}{\beta\sinh\beta}, & \text{for } 0<x<\xi\\ \frac{1}{1-v^2}\mathrm{e}^{\alpha(x-\xi)}\frac{\sinh\beta(1-x)\sinh\beta\xi}{\beta\sinh\beta}, & \text{for } \xi<x<1\end{cases} \tag{4.10}$$

The solution of the inverse Laplace transform is

$$g(x,\xi,t-\tau)=\mathcal{L}^{-1}\{G(x,\xi,s)\}=\frac{1}{2\pi\mathrm{i}}\int_{\gamma-\mathrm{i}\infty}^{\gamma+\mathrm{i}\infty}G(x,\xi,s)\mathrm{e}^{s(t-\tau)}\mathrm{d}s \tag{4.11}$$

Since $\sinh\beta=0$ at $\beta=\pm\mathrm{i}n\pi$, the equation $G\mathrm{e}^{s(t-\tau)}$ has simple poles at

$$s_n=\frac{-\eta\pm\mathrm{i}\sqrt{\left[4n^2\pi^2(1-v^2)-\eta^2\right](1-v^2)}}{2}=-\frac{\eta}{2}\pm\mathrm{i}\omega_n,\ \ n=1,2,3,\ldots \tag{4.12}$$

These simple poles are the exact eigenvalues as shown in equations (2.23) and (2.24) in Chapter 2. Note that when $\beta\to 0$ as well as $s\to\frac{-\eta\pm\eta\sqrt{1-v^2}}{2}$, the limit of $G(x,\xi,s)\mathrm{e}^{s(t-\tau)}$ exist. Therefore, $\beta=0$ is not a pole for $G(x,\xi,s)\mathrm{e}^{s(t-\tau)}$, neither is it for $G(x,\xi,s)$ [104].

Applying the Residue Theory to solve the inverse Laplace transform [58].

$$\frac{1}{2\pi\mathrm{i}}\int_{\gamma-\mathrm{i}\infty}^{\gamma+\mathrm{i}\infty}G(x,\xi,s)\mathrm{e}^{s(t-\tau)}\mathrm{d}s=\mathrm{Res}[G(x,\xi,s)\mathrm{e}^{s(t-\tau)},s=-\frac{\eta}{2}\pm\mathrm{i}\omega_n] \tag{4.13}$$

The Green's function can be obtained by solving equation (4.13) as follows

$$\begin{aligned}g(x,\xi,t-\tau) &= \sum_{n=1}^{\infty}\left[\frac{(1-v^2)\mathrm{e}^{(-\frac{\eta}{2}+\mathrm{i}\omega_n)(t-\tau)}\mathrm{e}^{\alpha_n(x-\xi)}\sin n\pi\xi\sin n\pi x}{\mathrm{i}\omega_n}\right.\\ &\quad\left.-\frac{(1-v^2)\mathrm{e}^{(-\frac{\eta}{2}-\mathrm{i}\omega_n)(t-\tau)}\mathrm{e}^{-\alpha_n(x-\xi)}\sin n\pi\xi\sin n\pi x}{\mathrm{i}\omega_n}\right]H(t-\tau)\\ &= \sum_{n=1}^{\infty}\frac{2(1-v^2)\mathrm{e}^{-\frac{\eta}{2}(t-\tau)}}{\omega_n}\left[\cos\left(\omega_n(t-\tau)\right)\sin\left(\frac{v\omega_n}{1-v^2}(x-\xi)\right)\right.\\ &\quad\left.+\sin\left(\omega_n(t-\tau)\right)\cos\left(\frac{v\omega_n}{1-v^2}(x-\xi)\right)\right]\sin n\pi x\ \sin n\pi\xi\, H(t-\tau)\end{aligned} \tag{4.14}$$

where $\alpha_n = \frac{iv\omega_n}{1-v^2}$, and $H(t-\tau)$ is the Heaviside function. In the solution of the Green's function, the functions of x are the eigenfunctions, and the functions of ξ are the adjoint eigenfunctions.

The forced vibration response can now be obtained by the convolution integral of the Green's function, $g(x, \xi, t-\tau)$, in equation (4.14) and external force, $f(x, t)$, such as

$$u(x,t) = \int_0^t \int_0^1 g(x, \xi, t-\tau) f(\xi, \tau) d\xi d\tau \tag{4.15}$$

4.3 The Standard Form of Equations

The preceding differential equation requires the initial and boundary conditions to complete the question. However, the non-homogeneous initial and boundary conditions often complicate the process to solve such problem. The standard form of equations converts the non-homogeneous initial and boundary conditions into homogeneous ones, and the original initial and boundary conditions is replaced by extra terms in external force. Therefore, the Green's function obtained from the homogeneous initial and boundary conditions still works for the non-homogemeous conditions [13].

Suppose that a stationary linear differential equation is given as

$$\mathrm{L}(x,u) = a_0 u^{(n)} + a_1 u^{(n-1)} + \cdots + a_n u = f(x,t) \tag{4.16}$$

with initial conditions

$$u(x,t_0) = u_0(x),\ \frac{\partial u}{\partial t}(x,t_0) = u_1(x),\ \ldots,\ \frac{\partial^{n-1} u}{\partial^{n-1} t}(x,t_0) = u_{n-1}(x) \tag{4.17}$$

and boundary conditions

$$\Gamma_i(u) = g_i, \quad i = 1, 2, \ldots \tag{4.18}$$

Equations (4.16), (4.17), and (4.18) are a system of equations. This system can be converted into the standard form [13].

$$\mathrm{L}(x,u) = a_0 u^{(n)} + a_1 u^{(n-1)} + \cdots + a_n u = f(x,t) + f_I(x,t) + f_B(x,t) \tag{4.19}$$

with homogeneous initial conditions

$$u(x,t_0)=0,\ \frac{\partial u}{\partial t}(x,t_0)=0,\ \ldots,\ \frac{\partial^{n-1}u}{\partial^{n-1}t}(x,t_0)=0 \tag{4.20}$$

and homogeneous boundary conditions

$$\Gamma_i(u)=0,\quad i=1,2,\ldots \tag{4.21}$$

Equations (4.19), (4.20), and (4.21) are called a system of equations in standard form for a given problem. The non-homogeneous initinal and boundary conditions are carried into $f_I(x,t)$ and $f_B(x,t)$, respectively. The standardizing function actually comprise two components, standardizing function with respect to the initial conditions, $f_I(x,t)$, and standardizing function with respect to the boundary conditions, $f_B(x,t)$.

The Green's function, $g(x,\xi,t,\tau)$, for such system can be obtained by giving an impulse input, $\delta(x-\xi)\delta(t-\tau)$, to replace the right side of the differential equation (4.19). The solution $u(x,t)$ will be

$$u(x,t)=\int_{t_0}^{t}\int_{D} g(x,\xi,t,\tau)\left[f(\xi,\tau)+f_I(\xi,\tau)+f_B(\xi,\tau)\right]d\xi d\tau \tag{4.22}$$

where D is the domain of x and ξ.

Recall the equation of motion of the damped axially moving wire (4.1)

$$u_{tt}+2vu_{xt}-(1-v^2)u_{xx}+\eta v u_x+\eta u_t=f$$

with a prescribed initial conditions as those in the Example 2 in Section 2.5.2

$$u(x,0)=a(x)=0.01\sin\pi x,\ \text{and}\ u_t(x,0)=0 \tag{4.23}$$

and fixed boundary conditions

$$\Gamma_1(u)=u(0,t)=0,\ \text{and}\ \Gamma_2(u)=u(1,t)=0 \tag{4.24}$$

Since the boundary conditions are homogeneous, $f_B(x,t)=0$, only initial conditions have to be standardized. Applying the Laplace transform to equation (4.1) by incorporating the

initial conditions, we obtain

$$s^2\bar{u}(x,s) - su(x,0) - u_t(x,0) + 2v\left(s\bar{u}_x(x,s) - u_x(x,0)\right) - (1-v^2)\bar{u}_x x(x,s)$$
$$+\eta v\bar{u}_x(x,s) + \eta\left(s\bar{u}(x,s) - u(x,0)\right) = \bar{f}(x,s)$$

where $\bar{u}(x,s)$ is the Laplace transform of $u(x,t)$, and $\bar{f}(x,s)$ is the Laplace transform of $f(x,t)$. Moving the terms involving the initial conditions to the right-hand side of the equation, we have

$$s^2\bar{u}(x,s) + 2vs\bar{u}_x(x,s) - (1-v^2)\bar{u}_x x(x,s) + \eta v\bar{u}_x(x,s) + \eta s\bar{u}(x,s)$$
$$= \bar{f}(x,s) + su(x,0) + u_t(x,0) + 2vu_x(x,0) + \eta u(x,0)$$

Therefore, the Laplace transform of $f_I(x,t)$ is

$$\bar{f}_I(x,s) = su(x,0) + u_t(x,0) + 2vu_x(x,0) + \eta u(x,0)$$

The standardizing function $f_I(x,t)$ can be obtained by taking inverse Laplace transform of $\bar{f}_I(x,s)$.

$$f_I(x,t) = \delta_t(t)u(x,0) + \delta(t)\left(u_t(x,0) + 2vu_x(x,0) + \eta u(x,0)\right) \tag{4.25}$$

Substituting the standardizing function into equation (4.22) with the corresponding initial conditions given in equation (4.23), and zero external force, $f(x,t) = 0$, the free vibration response of a damped axially moving wire can be obtained in the following

$$\begin{aligned} u(x,t) &= \int_0^t \int_0^1 g(x,\xi,t,\tau) f_I(\xi,\tau) d\xi d\tau \\ &= 0.01 \int_0^t \int_0^1 g(x,\xi,t,\tau)\left[\delta_\tau(\tau)\sin\pi\xi + \delta(\tau)\left(2v\pi\cos\pi\xi + \eta\sin\pi\xi\right)\right] d\xi d\tau \\ &= -0.01 \int_0^1 g_\tau(x,\xi,t,0)\sin\pi\xi d\xi + 0.01 \int_0^1 g(x,\xi,t,0)\left(2v\pi\cos\pi\xi + \eta\sin\pi\xi\right) d\xi \end{aligned} \tag{4.26}$$

where the Green's function, $g(x,\xi,t,\tau)$, is presented in equation (4.14). The closed-form solution of equation (4.26) is given in Appendix B. Given $\eta = 1$ and $v = 0.3$, the free vibration response (4.26) is plotted in Figure 4.1, which matches with the results in Figure 2.4 of Section 2.5.2.

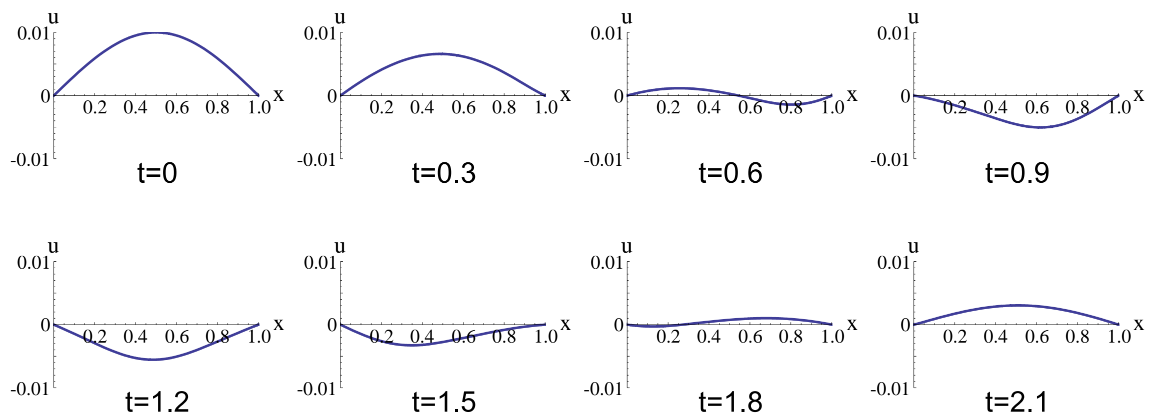

Figure 4.1: Plot of free vibration response in equation of a damped moving wire in equation (4.26) with $\eta = 1$ and $v = 0.3$. The initial displacement is $u(x, 0) = 0.01 \sin \pi x$, and the initial velocity is zero.

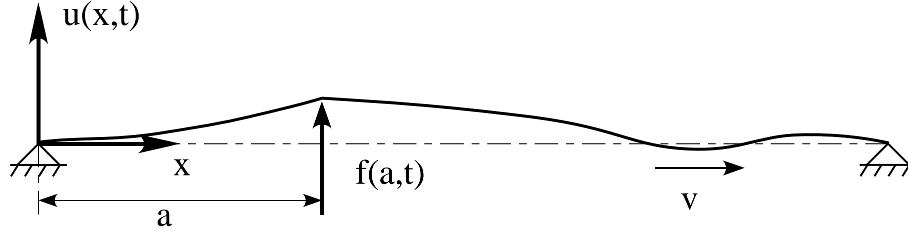

Figure 4.2: Schematic of wiresaw with point excitation

4.4 Frequency Response with Point Excitation

The frequency response with point excitation of the damped axially moving wire has been numerically studied in [24]. However, once the closed-form solution of the Green's function is derived in equation (4.14), it can be employed to obtain the frequency response analytically. In the following subsections, we present two methodologies to obtain the frequency response subject to a point harmonic excitation of $f(x,t) = \delta(x-a)\mathrm{e}^{\mathrm{i}\omega t}$, and compare the results obtained by the two independent methods.

4.4.1 Frequency response by the Green's function

Frequency response is very important in the analysis of vibration. It shows the responses and locations of the resonant frequencies and amplitudes of a system. In the study of control theory and random vibration analysis, frequency response and the spectral density are fundamental.

The Green's function was derived in Section 4.2, and the vibration response can be obtained by the integral equation (4.15), as follows

$$u(x,t) = \int_0^t \int_0^1 g(x,\xi,t-\tau) f(\xi,\tau) d\xi d\tau$$

In order to obtained the frequency response with point excitation, we assume a point harmonic excitation, $f(x,t) = \delta(x-a)\mathrm{e}^{\mathrm{i}\omega t}$, where a is the position to which external

excitation is applied as shown in Figure 4.2. The vibration response is

$$\begin{aligned}
u(x,t) &= \int_0^t \int_0^1 g(x,\xi,t-\tau)\delta(\xi-a)\mathrm{e}^{\mathrm{i}\omega\tau} d\xi d\tau \\
&= \sum_{n=1}^{\infty} \frac{1-v^2}{\mathrm{i}\omega_n} \left[\frac{\mathrm{e}^{\alpha_n(x-a)} \sin n\pi a \sin n\pi x}{\frac{\eta}{2}+\mathrm{i}(\omega-\omega_n)} - \frac{\mathrm{e}^{-\alpha_n(x-a)} \sin n\pi a \sin n\pi x}{\frac{\eta}{2}+\mathrm{i}(\omega+\omega_n)} \right] \mathrm{e}^{\mathrm{i}\omega t} \\
&\quad - \sum_{n=1}^{\infty} \frac{1-v^2}{\mathrm{i}\omega_n} \frac{\mathrm{e}^{\alpha_n(x-a)} \sin n\pi a \sin n\pi x}{\frac{\eta}{2}+\mathrm{i}(\omega-\omega_n)} \mathrm{e}^{(-\frac{\eta}{2}+\mathrm{i}\omega_n)t} \\
&\quad + \sum_{n=1}^{\infty} \frac{1-v^2}{\mathrm{i}\omega_n} \frac{\mathrm{e}^{-\alpha_n(x-a)} \sin n\pi a \sin n\pi x}{\frac{\eta}{2}+\mathrm{i}(\omega+\omega_n)} \mathrm{e}^{(-\frac{\eta}{2}-\mathrm{i}\omega_n)t} \qquad (4.27)
\end{aligned}$$

The transient response with the last two terms of summation decay with time and approach zero as time progresses. The decaying envelop is $\mathrm{e}^{-\frac{\eta}{2}t}$. The first summation term is the steady-state response, whose coefficient is

$$Z(x,a,\omega) = \sum_{n=1}^{\infty} \frac{1-v^2}{\mathrm{i}\omega_n} \left[\frac{\mathrm{e}^{\alpha_n(x-a)} \sin n\pi a \sin n\pi x}{\frac{\eta}{2}+\mathrm{i}(\omega-\omega_n)} - \frac{\mathrm{e}^{-\alpha_n(x-a)} \sin n\pi a \sin n\pi x}{\frac{\eta}{2}+\mathrm{i}(\omega+\omega_n)} \right] \qquad (4.28)$$

which is considered as the frequency response with point excitation. Figure 4.3 shows an example of the absolute value of equation (4.28) with respect to the excitation frequency ω.

4.4.2 Frequency response by the flexible influence function

Another method to solve the frequency response is the flexibility influence function [67]. To obtain the frequency response, assume $u(x,t) = Z(x,a,\omega)e^{i\omega t}$ and $f = \delta(x-a)\mathrm{e}^{i\omega t}$. where $Z(X,a,\omega)$ is the frequency response of the axially moving wire, a is the excitation point, ω is the frequency of the external force. Substitute these assumptions into equation (4.1), to obtain

$$(1-v^2)\frac{d^2Z}{dx^2} - (\eta v + 2\mathrm{i}v\omega)\frac{dZ}{dx} + (\omega^2 - \mathrm{i}\omega\eta)Z = -\delta(x-a) \qquad (4.29)$$

The impulse function, $\delta(x-a)$, of the equation is zero except at $x=a$. Thus, we have

$$\begin{aligned}
(1-v^2)\frac{d^2Z^-}{dx^2} - (\eta v + 2\mathrm{i}v\omega)\frac{dZ^-}{dx} + (\omega^2 - \mathrm{i}\omega\eta)Z^- &= 0 \qquad \text{for } 0 < x < a \\
(1-v^2)\frac{d^2Z^+}{dx^2} - (\eta v + 2\mathrm{i}v\omega)\frac{dZ^+}{dx} + (\omega^2 - \mathrm{i}\omega\eta)Z^+ &= 0 \qquad \text{for } a < x < 1
\end{aligned}$$

(a) Frequency response obtained by the Green's function

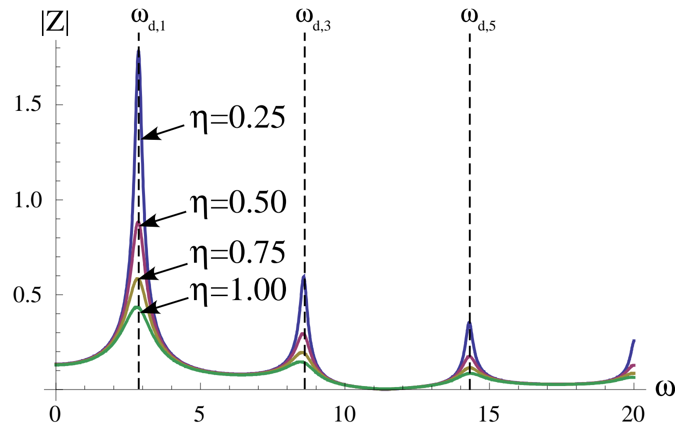

(b) Frequency response obtained by the flexibility influence method

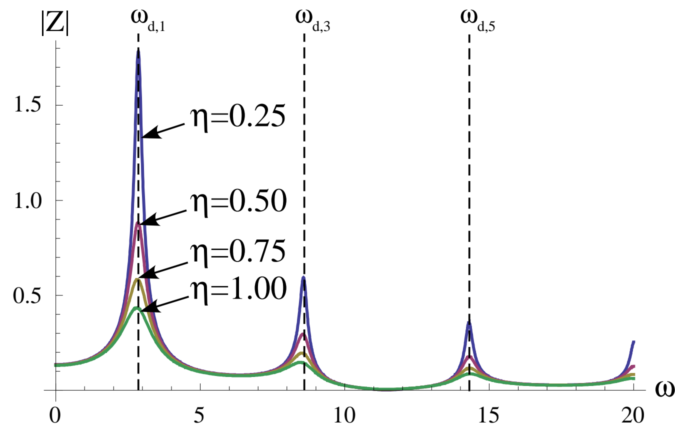

Figure 4.3: Absolute value of frequency response at $x = 0.25$ with point excitation at $a = 0.5$ and dimensionless velocity $v = 0.3$, which are obtained from (a) equation (4.28) and (b) equation (4.34).

Next, we assume $Z(x, a, \omega) = \mathrm{e}^{\lambda(\omega)x}$. Thus, the solutions of λ are the roots of

$$(1 - v^2)\lambda^2 - (2\mathrm{i}v\omega + \eta v)\lambda + (\omega^2 - \mathrm{i}\omega\eta) = 0$$

Therefore,

$$\lambda = \frac{2\mathrm{i}v\omega + \eta v \pm \sqrt{\eta^2 v^2 - 4\omega^2 + 4\mathrm{i}\omega\eta}}{2(1 - v^2)} = \alpha \pm \beta \tag{4.30}$$

The frequency response is obtained in the following

$$\begin{aligned} Z^-(x, a, \omega) &= \mathrm{e}^{\alpha x}\left(A\mathrm{e}^{\beta x} + B\mathrm{e}^{-\beta x}\right) \qquad \text{for } 0 < x < a \\ Z^+(x, a, \omega) &= \mathrm{e}^{\alpha x}\left(C\mathrm{e}^{\beta x} + D\mathrm{e}^{-\beta x}\right) \qquad \text{for } a < x < 1 \end{aligned}$$

Apply the boundary conditions, $Z^-(0, a, \omega) = 0$ and $Z^+(1, a, \omega) = 0$ to obtain $B = -A$ and $D = -C\mathrm{e}^{2\beta}$. Thus, we have

$$\begin{aligned} Z^-(x, a, \omega) &= A\mathrm{e}^{\alpha x}\left(\mathrm{e}^{\beta x} - \mathrm{e}^{-\beta x}\right) \qquad \text{for } 0 < x < a \\ Z^+(x, a, \omega) &= C\mathrm{e}^{\alpha x}\left(\mathrm{e}^{\beta x} - \mathrm{e}^{2\beta}\mathrm{e}^{-\beta x}\right) \qquad \text{for } a < x < 1 \end{aligned}$$

Since the string is continuous at $x = a$, we require $Z^-(x, a, \omega) = Z^+(x, a, \omega)$ at $x = a$. Consequently,

$$A\mathrm{e}^{\alpha a}\left(\mathrm{e}^{\beta a} - \mathrm{e}^{-\beta a}\right) = C\mathrm{e}^{\alpha a}\left(\mathrm{e}^{\beta a} - \mathrm{e}^{2\beta}\mathrm{e}^{-\beta a}\right) \tag{4.31}$$

In addition, the force equilibrium at $x = a$ renders

$$\left(1 - v^2\right)\left(\frac{dZ^+(x, a, \omega)}{dx} - \frac{dZ^-(x, a, \omega)}{dx}\right) = -1 \tag{4.32}$$

Therefore,

$$\begin{aligned} &C\left[\alpha\mathrm{e}^{\alpha a}\left(\mathrm{e}^{\beta a} - \mathrm{e}^{2\beta}\mathrm{e}^{-\beta a}\right) + \beta\mathrm{e}^{\alpha a}\left(\mathrm{e}^{\beta a} + \mathrm{e}^{2\beta}\mathrm{e}^{-\beta a}\right)\right] \\ &\quad -A\left[\alpha\mathrm{e}^{\alpha a}\left(\mathrm{e}^{\beta a} - \mathrm{e}^{-\beta a}\right) + \beta\mathrm{e}^{\alpha a}\left(\mathrm{e}^{\beta a} + \mathrm{e}^{-\beta a}\right)\right] = -\frac{1}{1 - v^2} \end{aligned} \tag{4.33}$$

The coefficients, A and C, can be obtained by solving the equations (4.31) and (4.33) as follows

$$\begin{aligned} A &= \frac{\mathrm{e}^{\beta a} - \mathrm{e}^{2\beta}\mathrm{e}^{-\beta a}}{2(1 - v^2)\beta(1 - \mathrm{e}^{2\beta})\mathrm{e}^{\alpha a}} \\ C &= \frac{\mathrm{e}^{\beta a} - \mathrm{e}^{-\beta a}}{2(1 - v^2)\beta(1 - \mathrm{e}^{2\beta})\mathrm{e}^{\alpha a}} \end{aligned}$$

Therefore, the frequency response of the damped axially moving wire is

$$Z(x,a,\omega)=\begin{cases}\frac{e^{\beta a}-e^{2\beta}e^{-\beta a}}{2(1-v^2)\beta(1-e^{2\beta})}e^{\alpha(x-a)}(e^{\beta x}-e^{-\beta x}), & \text{for} \quad 0<x<a\\ \frac{e^{\beta a}-e^{-\beta a}}{2(1-v^2)\beta(1-e^{2\beta})}e^{\alpha(x-a)}(e^{\beta x}-e^{2\beta}e^{-\beta x}), & \text{for} \quad a<x<1\end{cases}$$

which can be represented by $\sinh$ functions, and the frequency response can be simplified as

$$Z(x,a,\omega)=\begin{cases}\frac{e^{\alpha(x-a)}\sinh(1-a)\sinh x}{(1-v^2)\beta\sinh\beta}, & \text{for} \quad 0<x<a\\ \frac{e^{\alpha(x-a)}\sinh a\sinh(1-x)}{(1-v^2)\beta\sinh\beta}, & \text{for} \quad a<x<1\end{cases} \tag{4.34}$$

One result of equation (4.34) is plotted in Figure 4.3 with the prescribed parameters, and compared with the solution obtained by the Green's function in equation (4.28). The plots show consistent results between the two independent methods.

4.5 Summary

The Green's function for the damped axially moving wire is derived and presented in this chapter. The poles of the Green's function in the s-domain of Laplace transform are actually the eigenvalues. The Green's function is a combination of the eigenfunctions and adjoint eigenfunctions. Based on the Green's function, we present the **closed-form** solution of the forced vibration response of a damped axially moving wire, as well as the frequency response with a point harmonic excitation. The results of frequency response are compared with another method using the flexibility influence function, and show consistent results. The free vibration response can also be obtained by converting the original equations into the standard form. The results of this study of the analytical solution of the Green's function is very important in control theory and random vibration analysis for damped axially moving continua.

Chapter 5

Effect of Mixed Abrasive Grits in Lapping Process

Wafers made of materials such as silicon, III-V and II-VI compounds, and optoelectronic materials, require a high-degree of surface quality in order to increase the yield in micro-electronics fabrication to produce IC chips and devices. Measurements of wafer surface quality include: nanotopography, surface morphology, global planarization, total thickness variation (TTV) and warp. Due to the reduction of feature size in micro-electronics fabrication, the requirements of such properties become more and more stringent. To meet such requirements, the wafer manufacturing processes of brittle semiconductor materials, such as slicing, lapping, grinding, and polishing have been continually improved. In this chapter, the lapping process of wafer surface treatment is studied with experimental results of surface roughness and material removal rate. In order to improve the performance of lapping processes, effects of mixed abrasive grits in the slurry of the free abrasive machining (FAM) process are studied using a single-sided wafer-lapping machine. Under the same slurry density, experiments employing different mixing ratios of large and small abrasive grits, and various normal loadings on the wafer surface applied through a jig are conducted for parametric study. With various mixing ratios and loadings, observations and measurements of the total amount of material removed, material removal rate, surface roughness, and relative angular velocity are presented and discussed in this chapter. The experiments show that the $1:1$ mixing ratio of abrasives removes more material than other mixing ratios under the same conditions, with a slightly higher surface

roughness. Modeling of the mixed abrasive particle distributions correspondingly indicates that the roughness trend is due to the abrasive distribution size and the particle contact mechanics. The results of this study can provide a good reference for the FAM processes that practitioners use today by exploiting different mixing ratios and loadings of abrasive slurry in the manufacturing processes.

5.1 Introduction

With the development of larger wafers and smaller feature sizes in the semiconductor industry, the requirements for the wafer substrate are becoming more and more stringent for both cost and quality. Following Moore's law, the International Technology Roadmap of Semiconductors (ITRS) indicates that the 450 mm wafer will be in production in 2012 [46] to keep the trend of cost reduction. Many analyses and discussions start to focus on the next generation wafer size [19, 28, 37, 79, 87, 96]. With the agreement of Intel, Samsung Electronics, and TSMC at the 450 mm wafer manufacturing transition [43], the next increase of wafer size is inevitable. With such increase, it is more difficult to achieve the requirements of wafer surface quality such as global planarization. Therefore, the advance of the machining processes such as wiresawing, lapping, and grinding is important.

Lapping has been a standard surface finishing process for glass products and semiconductor wafers for a long time. It belongs to the free abrasive machining (FAM) process which is the same as slurry wiresaw slicing [5, 22, 107]. FAM is a three-body abrasion mechanism which is not desirable for the journal bearing because of wear [34, 84, 100]. However, it is the essential machining mechanism for lapping. Although most research attributes the brittle material removal of lapping to indentation cracking model [11, 12, 16, 52, 80], the actual situation is more complicated [15, 38, 57]. Aside from the mechanical properties of the workpiece and lapping plate, the distribution of abrasives, dynamic indentation cracking, motion of the abrasive grits and the ductile-regime machining [9] also complicate the analysis of lapping mechanism.

Lapping and grinding are both post-slicing wafer surface finishing processes. Because of their advantages and disadvantages, one or both of them are utilized in the manufacturing process [56, 77]. It is not clear which one will be favorable or employed in the 450 mm wafer industry. However, lapping was the one which can remove warp efficiently until the invention of simultaneous double-sided grinding [55, 77]. In this chapter, experimental study and modeling of surface roughness of mixed abrasive slurry in lapping provides the information on the influence of abrasive distribution on lapping.

Past research has emphasized the importance of abrasive size distribution in modeling; however, few studied the change of the distribution of the abrasive grit sizes. Bhagavat, Liberato, and Kao [7] are probably the first and the only ones to study such topic. Their results showed that the mixed abrasives (for example, mixing F-400 and F-600 SiC) have higher material removal rate than the single-sized abrasives (for example, only F-400 SiC abrasives). However, their experiments discussed one mixing ratio of the abrasives, and the concentration of mixed-abrasive slurries were different from that of the single-sized abrasives slurry. To study the influence of the change of abrasive distribution in lapping, experiments with different abrasive distributions and constant slurry concentration are necessary.

In this study, experiments were conducted by mixing two different sizes of silicon carbide powders: F-400 and F-600. Five different mixing ratios of the abrasives were employed, though, the ratio of the abrasives to the carrier (DI water) was kept the same. The results show that the 50% mixing ratio ($1:1$) of the two different abrasives have the highest material removal rate (MRR), with a slightly rougher surface finish. In addition, the material removal rate is nearly proportional to the normal loading. The surface roughness, however, depends on the distribution of mixed abrasive grits but not the total loading. This is comparable to results presented in the literature [12, 80]. A model of surface roughness based on particle contact depth was utilized to compare effects of different mixing ratios. This model considers the particle size effect on the active abrasive grits, the abrasive size

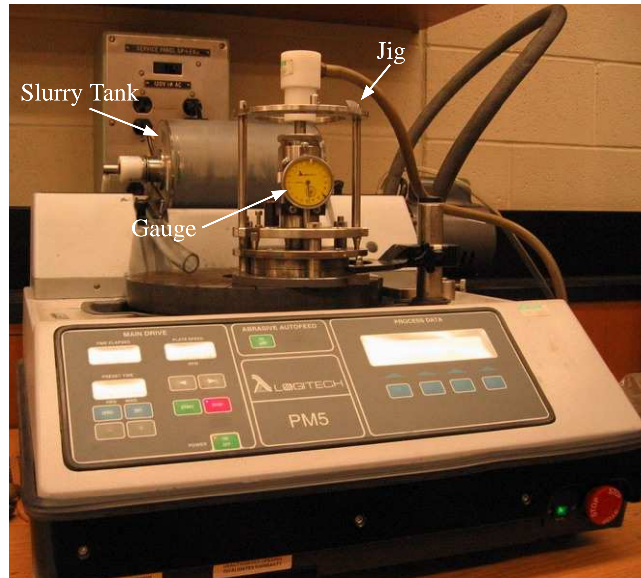

Figure 5.1: Logitech PM5 lapping machine, employed to conduct experiments in this study.

distributions, and applied load, to provide a correlation with the experiments using the process parameters.

5.2 Experimental Setup

Logitech PM5 one-sided lapping machine, as shown in Figure 5.1, was employed in this experimental study. A PP6GT jig was used to hold the silicon wafer which was mounted on glass plate by wax. The dial gauge mounted on the jig provides real-time measurement of the material removal depth during the lapping operation. In addition, the jig provides a constant normal load on the wafer during the machining process. All wafers used in the experiments are 3-inch $< 1\ 1\ 1 >$ silicon wafers.

Two different grades of silicon carbide powders, F-400 and F-600, were used in the experiments. The median sizes of F-400 and F-600 powders are $17.3\ \mu\text{m}$ and $9.3\ \mu\text{m}$, respectively [1] . Table 5.1 shows the FEPA **Grading Chart** of these two abrasive grits. Deionized (DI) water was chosen as the carrier fluid. In order to study the different distribution

[1] According to different measurement, there are different results for the distribution of abrasive grits [48]. In this study, we follow the FEPA grading chart.

Table 5.1: FEPA Grading Chart of F-400 and F-600 SiC powders (μm)

SiC powder	$D3\%$	$D50\%$	$D94\%$
Fepa F-400	32	17.3±1.5	8
Fepa F-600	19	9.3±1	3

of abrasives in slurry, the ratio of the weight of abrasives to the weight of carrier fluid, C, was kept at a constant value of 0.154. Five different ratios of the weight of F-400 powder, W_{400}, to the total weight of abrasives, W_{total}, were employed in the experiments to study the effect of different distribution of abrasives in lapping process. The ratios are $\frac{W_{400}}{W_{total}} = 0$, $\frac{1}{4}$, $\frac{1}{2}$, $\frac{3}{4}$, and 1.

During the experiments, the angular velocity of the cast iron lapping plate was kept at 70 RPM. The material removal depth and the angular velocity of the jig were recorded every five minutes. Every experiment lasted for 30 minutes. Two different loadings, 2.3 and 4.1 kg (5 and 9 pounds), were applied on the jig. Therefore, there were a total 10 different settings, five distribution of abrasives by two loadings. Six experiments were conducted under each setting of parameters.

After lapping, the wafer was cleaned by de-ionized water, and the wax was melted to remove silicon wafer from the glass plate. Surface morphology was examined with a Keyence optical microscope, and the surface roughness was measured with a XP2 diamond probe profilometer at eight randomly selected locations. Each scan of surface roughness is 2 mm in length, which is much larger than the size of fracture on the wafer surface.

5.3 Results and Analysis

5.3.1 Material removal depth

The reduction of the thickness of wafer during lapping process was measured in real-time by the dial gauge every five minutes, in order to record the history of the material removal rate under different loadings and distribution of abrasive grits. Figure 5.2 plots the

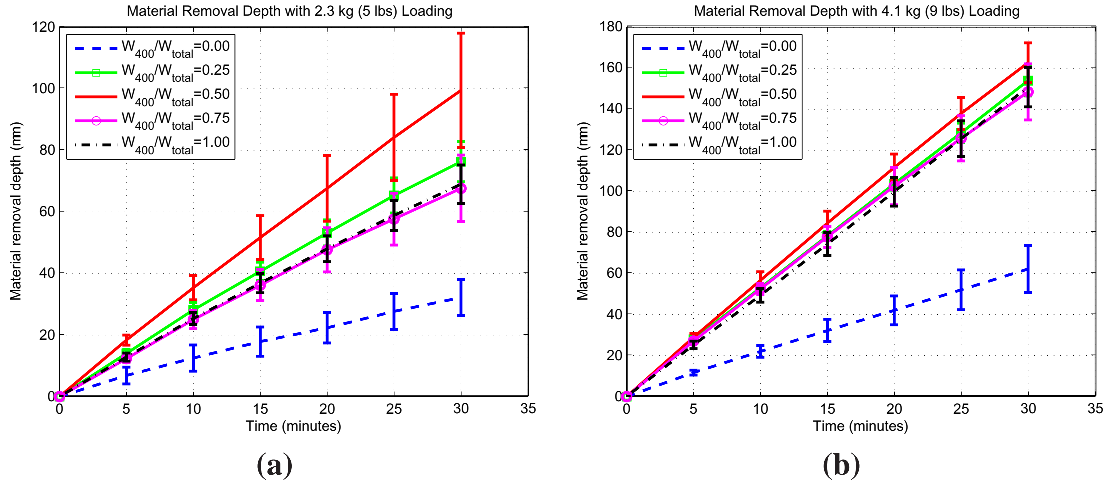

Figure 5.2: Depth of the material removal with (a) 2.3-kg and (b) 4.1-kg loadings in lapping.

results of experiments.

There are two important observations in the two figures. First, when $\frac{W_{400}}{W_{total}} = 0.5$, it has the highest material removal rate regardless of the loading being 2.3 or 4.1 kg. When $\frac{W_{400}}{W_{total}} = 0$, with only the F-600 grits in the slurry, the material removal rate is always the lowest. The other three distribution ratios of abrasives have similar material removal rates. However, the material removal rate with 50% mixing ratio at the loading of 4.1 kg is not more prominent than the others compared with the case with the loading of 2.3 kg. The contrast can be observed from Figure 5.2. Furthermore, the material removal rate is always higher under 4.1 kg loading with the same mixing ratio of abrasive grits, as expected.

5.3.2 Angular velocity of the jig

The angular velocity of the jig is a passive parameter of the lapping experiments and can not be controlled independent of the speed of the lapping plate. The results were also recorded every five minutes during the experiments and plotted in Figure 5.3 to show the history of the angular speed of the jig.

The figures show that the angular velocities of the jig vary within a small range. The

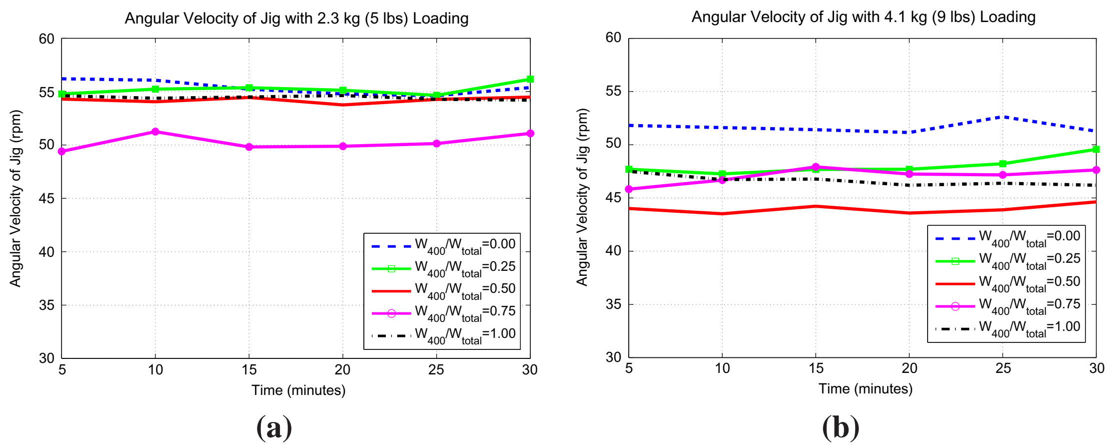

Figure 5.3: Angular velocity of jig with the (a) 2.3-kg and (b) 4.1-kg loadings during lapping.

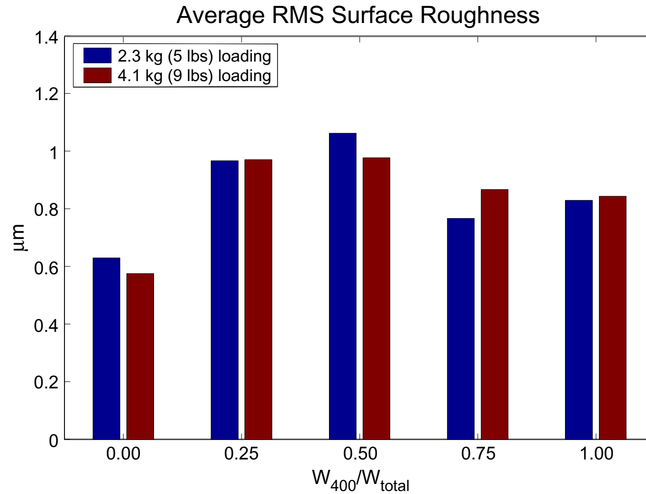

Figure 5.4: Average RMS surface roughness after lapping. The unit is in micron.

jig has higher angular velocity under the lower loading of $2.3\ \mathrm{kg}$ than that under the higher loading. This means that the relative angular velocity between the jig and the lapping plate, which has a constant angular velocity of 70 RPM during the experiments, is lower at the $2.3\ \mathrm{kg}$ loading. However, there is no significant correlation between the angular velocity of the jig and the other parameters, such as material removal rate or surface roughness.

5.3.3 Surface roughness

One purpose of lapping is to flatten the wafer after slicing for better surface quality. Although the chemical-mechanical polishing is the final process to achieve the mirror-like wafer surface finish, the surface topography after lapping is very important. Figure 5.4 shows the average root-mean-square (RMS) surface roughness after lapping, measured by the XP2 profilometer with a diamond probe. The figure shows that the surface roughness does not correlate significantly to the increase of loading, as presented in the literature [12, 80]. However, the different ratios of the mixed abrasive grits result in different surface roughness, with the half-half mixed abrasive slurry having the highest surface roughness under the same loading.

Comparing to Figure 5.2, we found that the higher material removal rate in the ma-

chining operation usually is accompanied by a higher surface roughness. This is intuitive. The results here illustrate that the change of the distribution of abrasive grits will affect the performance of material removal rate and the surface roughness.

5.3.4 Surface morphology

The surfaces of lapped wafers were examined by optical microscope. All surfaces show the typical surface morphology of lapped wafers. Features and evidence of fractures, cracks, indentation marks, and scratches can be seen on the lapped surface under the microscope. These surface features show the complicated machining mechanisms to shape the surface. Figure 5.5 shows typical surface morphology of silicon wafers under different setting of parameters conducted in experiments in this study.

5.4 Surface Roughness Model for Mixed Abrasive Lapping[2]

The roughness resulting from the mixed abrasive lapping process is modeled by the roughness contribution resulting from each abrasive powder in the mixed distribution. This is accomplished by a rule of mixtures of the mass percentage of each abrasive constituent in the slurry. By modeling the roughness in this manner, each abrasive particle size can be considered separately, though the contact interaction effect of each particle size on the other will be considered within individual models. Take the roughness generated by the F-400 and F-600 abrasives on the silicon substrate as R_s^{400} and R_s^{600}, respectively, then combining in a rule of mixtures yields the relationship for the total silicon substrate roughness,

$$R_s = \chi R_s^{400} + (1 - \chi) R_s^{600} \tag{5.1}$$

where the weight percent ratio is $\chi = W_{400}/(W_{400} + W_{600})$.

[2] This section is contributed by Professor Chad S. Korach [26] in the Department of Mechanical Engineering, State University of New York at Stony Brook.

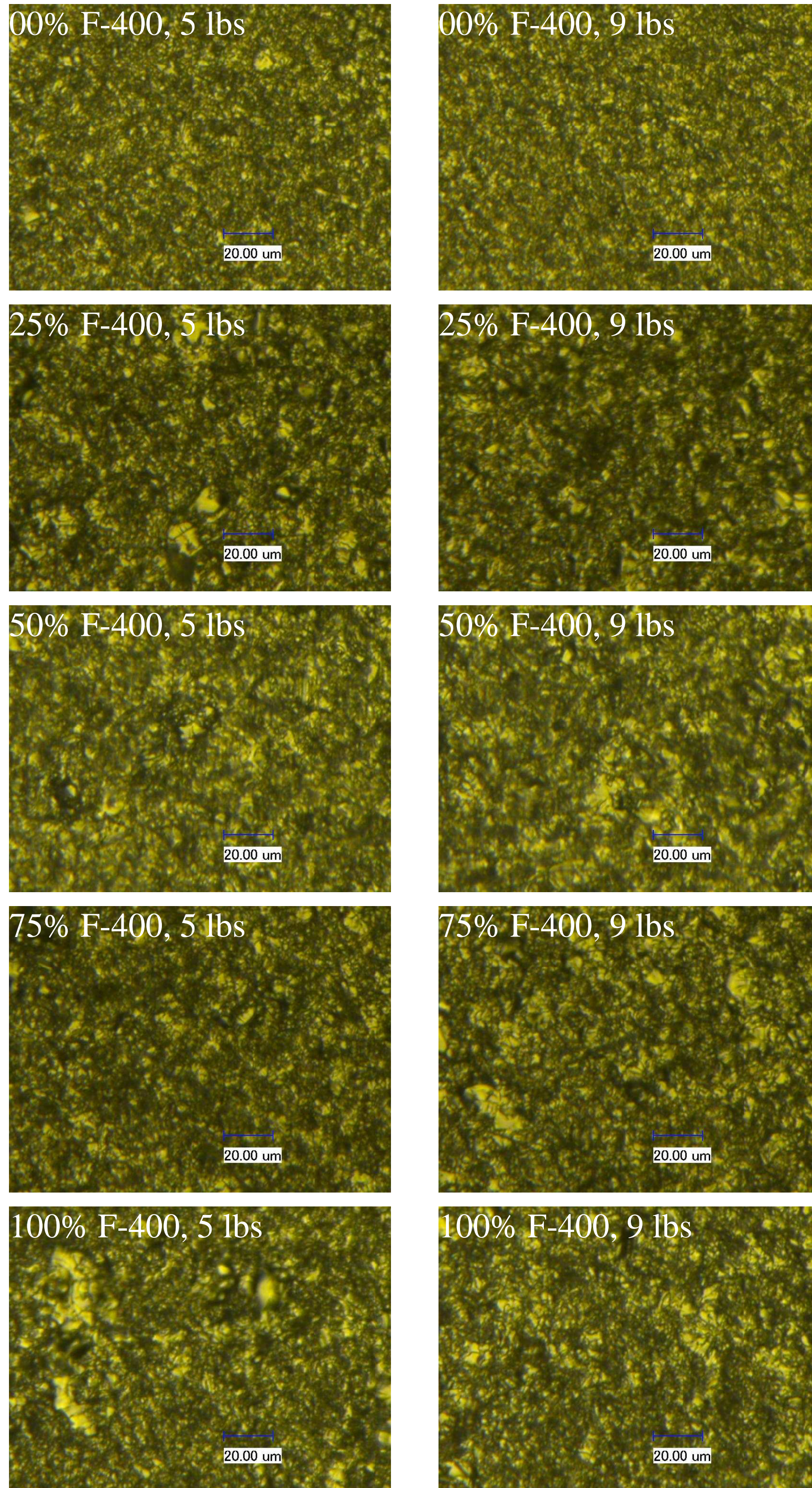

Figure 5.5: Typical surface morphology of lapped wafer surface. The scale bar is 20 μm.

To model the roughness of the lapping process, the mechanics between abrasive particles and the silicon substrate are modeled where a constant load applied to a spherical particle penetrates the surface. Abrasive removal of material is assumed as the dominate material removal mechanism. The general equation for the roughness is based on the penetration depth of an abrasive particle into the silicon substrate. The framework has been presented by Brown et al. [10] and later by Cook [27], and has been applied to glass polishing, superpolishing of metals, and ductile grinding of brittle materials. Here, we extend the model framework to consider mixed abrasive distribution effects on the resulting substrate roughness from mixed abrasive lapping. If a concentration of k spherical abrasive particles (with diameter of ϕ) are in contact with a nominal pressure per particle (p), the roughness for a specific distribution (R_s^i) is represented by the surface penetration,

$$R_s^i = \frac{3\phi}{4}\left(\frac{p}{2kE_r}\right)^{2/3} \tag{5.2}$$

where p is the nominal pressure of the wafer-platen interface and is determined by dividing the applied load by the nominal wafer area (76.2 mm diameter wafer), and i indicates the abrasive powder (either F-400 or F-600). The reduced modulus of the contact (E_r) is given by

$$\frac{1}{E_r} = \frac{1-\nu_p^2}{E_p} + \frac{1-\nu_s^2}{E_s} \tag{5.3}$$

where E_s is the Si(111) substrate elastic modulus (=190 GPa) with Poisson ratio of $\nu_s = 0.26$, and the abrasive particle, SiC, elastic modulus is $E_p = 415$ GPa, with $\nu_p = 0.16$. These values yield a reduced modulus of the contact of $E_r = 138$ GPa. Since the slurry is a mixed abrasive slurry, each particle size will contribute to the overall contact and hence roughness of the substrate. Equation (5.2) is applied to both particle sizes, F-400 and F-600, taking into consideration the contributions separately. The diameters are taken as one standard deviation from the mean, 15.8 and 10.3 μm for F-400 and F-600, respectively. From Eq. (5.2), the contact is governed by the concentration factor k, where as k becomes small, the roughness increases, due to an increase in the per particle contact load.

The interaction between the F-400 and F-600 particles will affect the resulting individual abrasive powder roughness on the silicon substrate. For a single abrasive case, the general relationship in Eq. (5.2) shows that as particle concentration decreases there will be a subsequent increase in roughness, due to the per particle load increase, which increases surface penetration. The model predicts a singularity in roughness as $k \rightarrow 0$, where in reality there will be a geometric limit to the roughness based on the particle size and the contact with the substrate and platen, which is one-half the particle diameter, or $R_{s,limit} = 0.5\phi$. For the abrasive particles (either F-400 or F-600), this limit would occur at $k = 5.86 \times 10^{-8}$ for $P = 40.1$ N (4.1 kg), and $k = 3.25 \times 10^{-8}$ for $P = 22.3$ N (2.27 kg). Though, the limiting value of roughness for the particle distributions is never reached for the mixed abrasive cases, due to the pressure of the second particle distribution in the slurry. For the F-400 case there would be a contact interaction effect beginning at a critical concentration of the F-600 particles, where large diameter particles present in the F-600 distribution begin to make contact. This phenomenon occurs up to a limit based on the F-600 particles reaching full concentration and hence limiting the F-400 particle surface penetration. The penetration limit of the F-400 particles is determined by considering the maximum penetration of the F-600 particles at full concentration in addition to the difference between the F-400 and F-600 particle radius, and is given by

$$R_S^{400}|_{limit} = \frac{3\phi_{600}}{4}\left(\frac{p}{2k_{max}E_r}\right)^{2/3} + \frac{1}{2}\left(\phi_{400} - \phi_{600}\right) \tag{5.4}$$

In the case of the F-600 particles, the resulting roughness is affected by the F-400 particle concentration, which as it increases will effectively replace the F-600 particle contacts, limiting the F-600 particles to only the largest in the distribution to contribute to the penetration.

The model for the F-400 roughness contribution during mixed abrasive lapping is

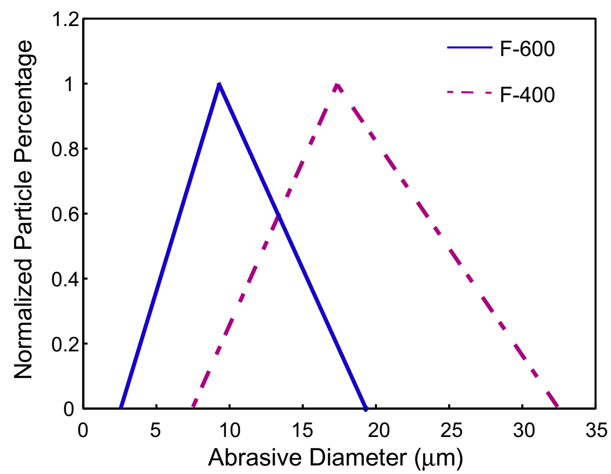

Figure 5.6: Normalized linear distributions for FEPA F-400 and F-600 SiC powders, based on data in Table 5.1. The slope of the F-600 powder from the mean size to the maximum size is calculated as $-0.1\%/\mu\mathrm{m}$. The tail portion of the F-600 distribution from $15.8\mu m$ to the maximum is 7.3% of the total distribution volume.

written as,

$$R_s^{400} = \frac{3\phi_{400}}{4}\left(\frac{p}{2k_{400}E_r}\right)^{2/3}, \qquad k^* \leq k_{400} \leq k_{max} \tag{5.5}$$

$$R_s^{400} = \frac{3\phi_{400}^{eff}}{4}\left(\frac{p}{2(k_{400}+\beta)E_r}\right)^{2/3}, \qquad 0 \leq k_{400} \leq k^* \tag{5.6}$$

The concentration k^* represents the critical point where F-600 particles of large enough diameter will begin to contribute to the load bearing and is represented by,

$$k^* = k_{max} \cdot \chi|_{\%cr} \tag{5.7}$$

where $\chi|_{\%cr}$ is a percentage based on the F-600 particle distribution shape (Fig. 5.6). Assuming a normalized linear particle distribution with a maximum at 9.3 μm and a value of 19 μm at 3% of the distribution, the slope of this linear distribution in Fig. 5.6 between these two points is found to be $-0.1\%/\mu$m. A critical particle diameter (15.8 μm) is assumed for the F-600 distribution, above which will contribute to the contact. This value is based on the F-400 particle distribution, and is determined by taking one standard deviation from the F-400 distribution mean value, i.e. $17.3 - 1.5$ $\mu\text{m} = 15.8$ μm. When the number of F-600 particles greater than 15.8 μm is equivalent to 10% ($\%cr$) of the total number of particle contacts (combined with the F-400 particles) a critical $\chi|_{\%cr}$ can be determined by,

$$\frac{(1-\chi)\alpha}{(1-\chi)\alpha + \chi} = \%cr \tag{5.8}$$

where χ can vary between 0 and 1, and α is the ratio of the number of critical F-600 particles that could be in contact. The ratio α is determined by the slope above of the F-600 distribution and the intersection of the lower value of the F-400 distribution mean (15.8 μm) and the F-600 distribution, which occurs at $\alpha = 7.3\%$. The value of $\%cr = 10\%$ is an assumption and states that 10% of the F-600 particles which have a diameter size larger than 15.8 μm will contribute to the contact. It was found that the result of $\chi|_{\%cr}$ within the experimentally measured range of the mixing ratios had small variations in $\%cr$ around 10%. Equation (5.8) yields a value of $\chi|_{\%cr} = 0.4$. Thus, from Eq. (5.7), $k^* = 0.4k_{max}$,

for the F-400 and F-600 mixed abrasive slurry. Between concentrations $k = 0$ to k^*, the R_s^{400} values follow Eq. (5.6). Since the maximum penetration of the F-400 distribution is given by Eq. (5.4), the roughness from the F-400 particle distribution will fall on a curve between $R_s^{400}|_{limit}$ and $R_s^{400}|_{k=k^*}$; the latter, which is the intercept with the R_s^{400} model between $k^* < k < k_{max}$, can be determined by Eq. (5.5) when $k = k^*$. Thus, the roughness between $0 < k < k^*$ is bound by the physical particle size limitation of the average F-400 particle and the critical concentration where the F-600 particles begin to make a significant contribution to the load bearing, affecting the F-600 penetration depth. The R_s^{400} model in Eq. (5.6) is fit between these two points where ϕ_{400}^{eff} and β are constants. Physically, ϕ_{400}^{eff} represents the effective change in the particle diameter with the introduction of the F-600 particles, which will affect the penetration depth. The constant can be solved by

$$\phi_{400}^{eff} = \frac{4}{3} R_s^{400}|_{limit} \left(\frac{2\beta E_r}{p} \right)^{2/3} \tag{5.9}$$

where $R_s^{400}|_{limit}$ is given by Eq. (5.4), and β represents a shift in the concentration to take into consideration the addition of the F-600 particles on the load bearing. The constant β can be computed by

$$\beta = 0.4 k_{max} \left[\frac{R_s^{400}|_{k^*}}{R_s^{400}|_{limit}} \right]^{3/2} \left(1 - \left[\frac{R_s^{400}|_{k^*}}{R_s^{400}|_{limit}} \right]^{3/2} \right)^{-1} \tag{5.10}$$

which is a function of the maximum concentration factor (k_{max}) and the pressure, p. Combining the model in Eqs. (5.4), (5.5), (5.6), (5.9), and (5.10) piecewise continuously, there is a decrease in the F-400 roughness (R_s^{400}) from a maximum value at $k_{400} = 0$ to k^* and minimizing at k_{max} (Fig. 5.7). The decrease in R_s^{400} with increasing concentration k_{400} is expected; as the load per particle decreases, the particle penetration will then decrease. The critical concentration value is generated due to the particle distribution overlap and proximity of the average particle sizes. As the distribution overlap decreases to zero, i.e. the distributions separate, the critical point k^* will move towards $k_{400} = 0$. This is a direct result of the reduced interaction between the larger F-600 particles and the F-400 distribution penetration depth. In fact, when the distributions move closer, i.e. an increase in

the overlap due to a small separation between the mean values, the maximum depth limit (Eq. (5.4)) which occurs at the low concentrations of F-400 will decrease; though k^* will increase due to a larger distribution overlap.

The model for the F-600 roughness contribution during mixed abrasive lapping is written as

$$R_s^{600} = \frac{3\phi_{600}^{eff}}{4}\left(\frac{p}{2k_{max}E_r}\right)^{2/3}, 0 \leq k_{600} \leq k_{max} \tag{5.11}$$

where k_{600} is the volume concentration of the F-600 particles. Here, ϕ_{600}^{eff} is the effective particle diameter of the F-600 distribution and physically represents the effective increase in the particle size due to the introduction of F-400 load bearing particles. The particle concentration is held constant at k_{max}, since as k_{600} decreases, the F-600 particles will be replaced by the larger F-400 particles, keeping the concentration of particles in contact approximately constant. The F-400 interaction effect on the particle diameter is modeled to increase in a linear manner, therefore ϕ_{600}^{eff} is represented by

$$\phi_{600}^{eff} = (1-\chi)\phi_{600} + \chi\phi_{400} \tag{5.12}$$

where $\phi_{600}^{eff} \rightarrow \phi_{400}$ as the percentage of F-400 increases, since the F-600 particles will not be the dominate contacts as $k_{600} \rightarrow 0$ and will effectively be limited by the F-400 particle size on the particle penetration depth, and hence roughness. Thus $R_s^{600}|_{k=0} \rightarrow R_s^{400}|_{k=k_{max}}$ is a logical conclusion of the model (Fig. 5.7). The effect of the F-400 particle interaction on R_s^{600} will cause a decrease in the roughness parameter over the result of R_s^{600}, and provide an upper bound at the F-600 low concentrations. The F-600 distribution roughness increases as the concentration k_{600} decreases (Fig. 5.7) up to a limit from the minimum value where $k_{600} = k_{max}$. As the abrasive distributions become similar, i.e. the overlap decreases, R_s^{600} will have bounding values at high and low concentrations of similar magnitude and become in essence constant or have an extremely shallow slope. This represents the insensitivity the roughness of the smaller abrasive would have due to domination by the larger abrasive in the load bearing contacts. Though, as the distribution overlap decreases, an effect on R_s^{400} as described above will occur simultaneously due to

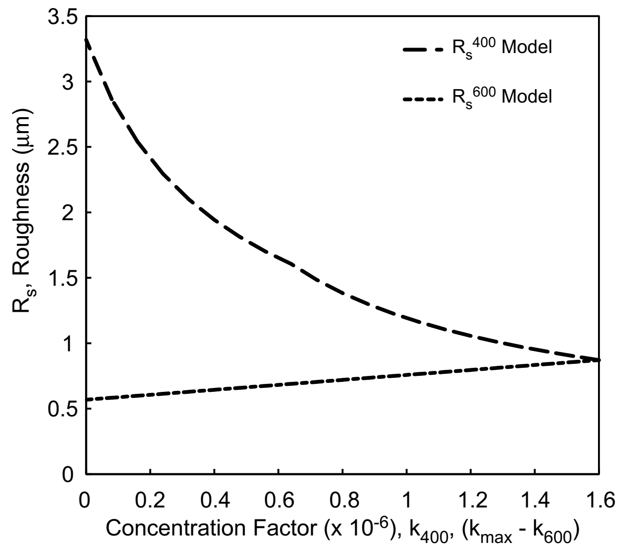

Figure 5.7: Plot of individual roughness contributions from the F-400 and F-600 roughness models, as a function of the concentration factor k. For R_s^{400} , k is defined by k_{400}, though for R_s^{600}, k is defined by $(k_{max} - k_{600})$ to plot on the same axis. As abrasive concentration decreases (decrease in k) the roughness decreases for the models of both powders. F-400 is affected by the interaction of the F-600 abrasives beginning at a critical concentration $k^* = 0.4k_{max}$, and is the reason for the change in slope of the F-400 roughness curve at $k = 0.64 \times 10^{-6}$.

Table 5.2: Values of model parameters used to generate model results in Figure 5.9

Parameter	Symbol	Value	
		$P = 2.3\,\text{kg}$	$P = 4.1\,\text{kg}$
F-400 Diameter (μm)	ϕ_{400}	15.8	
F-600 Diameter (μm)	ϕ_{600}	10.3	
Pressure (kPa)	p	4.9	8.8
Reduced Modulus (GPa)	E_r	138	
Maximum Concentration	k_{max}	8.5×10^{-7}	1.6×10^{-6}
Interaction Critical Weight Ratio	$\chi\|_{\%cr}$	0.4	

the changes in abrasive distribution interaction. The two distributions become homogenous as the particle diameters become similar.

The total roughness given by Eq. (5.1) follows a rule of mixtures based on the mass percentage of the slurry particles for each distribution multiplied by the distribution roughness modeled in Eqs. (5.5), (5.6), and (5.11). The rule of mixtures assumption provides an approximate representation of the roughness, since it is determining an average over a surface, similar to a roughness average calculation. The percent of active abrasive particles, n, is defined by $n = k_{max}/(C/(\rho_{H_2O}/\rho_{SiC}))$, where C is the mass percent of abrasive in the slurry, which was held constant at 15.4%, and ρ_{SiC} is the SiC powder density ($= 3.16$ g/cm^3), and is the relationship used to calculate k_{max}. The active abrasive percentage is taken as a model parameter which is fit to the experimental data. The percentage of active abrasives is the only parameter which is variable to the experimental data and the shape of the model curve is generated solely on the assumptions made and described in the model formulation. Table 5.2 presents the necessary model parameter values to compute the results found in the following section.

5.5 Discussion

In the following sections, we study the relationship among the parameters of the loading, material removal rate, and surface roughness. We found that the abrasive distri-

Table 5.3: The average material removal rate ($\mu\mathrm{m}/\mathrm{min}$) under differing loadings and mixing ratios

	$\frac{W_{400}}{W_{total}} = 0$	0.25	0.50	0.75	1
2.3 kg (5 lbs)	1.072	2.544	3.317	2.256	2.300
4.1 kg (9 lbs)	2.072	5.133	5.422	4.950	5.028

bution has significant contribution to the outcomes of lapping operation, as shown in the previous sections. In this section, the normal loading, material removal rate, and surface roughness will be compared to each other with different abrasive mixing ratios. Results of the surface roughness will be explained in the context of the mixed abrasive roughness model.

5.5.1 Loading versus material removal rate

In Figure 5.2, the material removal depth of the wafers in lapping is nearly linear with respect of time during the operation. Therefore, the average material removal rate (MRR) is defined as the total removal depth divided by the operation time, 30 minutes, as listed in Table 5.3.

The results in Table 5.3 show that higher total loading will result in higher MRR, and the larger abrasive grits will produce higher MRR, as expected. However, the highest MRR happens at the 50% mixing ratio of abrasive grits (Fig. 5.8). This is consistent with the results presented in Bhavagat et. al [7], although the slurry concentrations were not kept at constant for the mixed and single-sized abrasive slurry in that work. In addition, the increase of material removal rate from the single larger abrasive to the 50% mixed ratio abrasive grits is 44% at the loading of 2.3 kg. However, this increase of material removal rate is only 7.8% at the higher loading of 4.1 kg. This means that the mixed abrasive slurry does not significantly affect the material removal rate under higher loadings. The reason could be due to the breakage of abrasives being more severe at higher loading, resulting in similar abrasive distribution during machining. However, compared to lower loading,

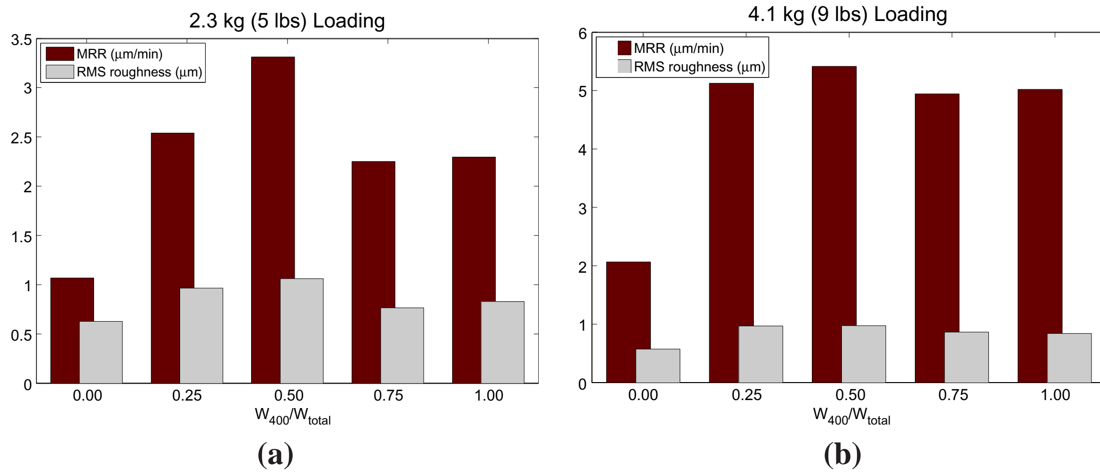

Figure 5.8: Comparison of material removal rate and RMS surface roughness at (a) 2.3-kg and (b) 4.1-kg loadings.

Table 5.4: The average RMS surface roughness (μm) under differing loadings and mixing ratios

	$\frac{W_{400}}{W_{total}} = 0$	0.25	0.50	0.75	1
2.3 kg (5 lbs)	0.6313	0.9688	1.0646	0.7688	0.8318
4.1 kg (9 lbs)	0.5771	0.9729	0.9792	0.8688	0.8458

the higher loading always results in higher material removal rate with the same abrasive mixing ratio.

5.5.2 Loading versus surface roughness

Table 5.4 shows the root-mean-square surface roughness value of the wafer surfaces after lapping. From the results, we find that the surface roughness is not dependent on the loading which has been discussed [12, 80]. Normally, abrasive grits with smaller mean size produce a smoother surface, and larger abrasives produce a rougher surface finish. In the case of mixed abrasive grits, however, it is obvious that the 50% abrasive mixing ratio produces the surface with the highest roughness. In addition, the abrasive distribution affects the surface roughness. Based on the observation from experiments, the surface roughness of wafers lapped by the mixed abrasives is similar quantitatively to the roughness produced by the slurry with single large abrasives. With higher loading at 4.1 kg, the surface roughnesses with mixed abrasive ratios 0.25, 0.5, and 0.75 have less variation (see Figure 5.4), as compared with the variation under lighter loading. This variation is also observed in the material removal rates in Figure 5.8. Figure 5.9(b) shows a comparison between the model curve (based on Eqs. (5.1), (5.5), (5.6), (5.11)) and the experimental roughness measured for a load of 4.1 kg. Here, $n = 3.29 \times 10^{-5}$ and is on a similar order to active particle percentages found by other lapping models [16]. Starting at a low concentration of F-400 (and large concentration F-600) the model predicts a roughness which rises to a maxiumum value at $\sim 40\% k_{max}$ and decreases at a lower rate to a roughness value associated with a high concentration of F-400 and low concentration of F-600 particles. The peak occurs

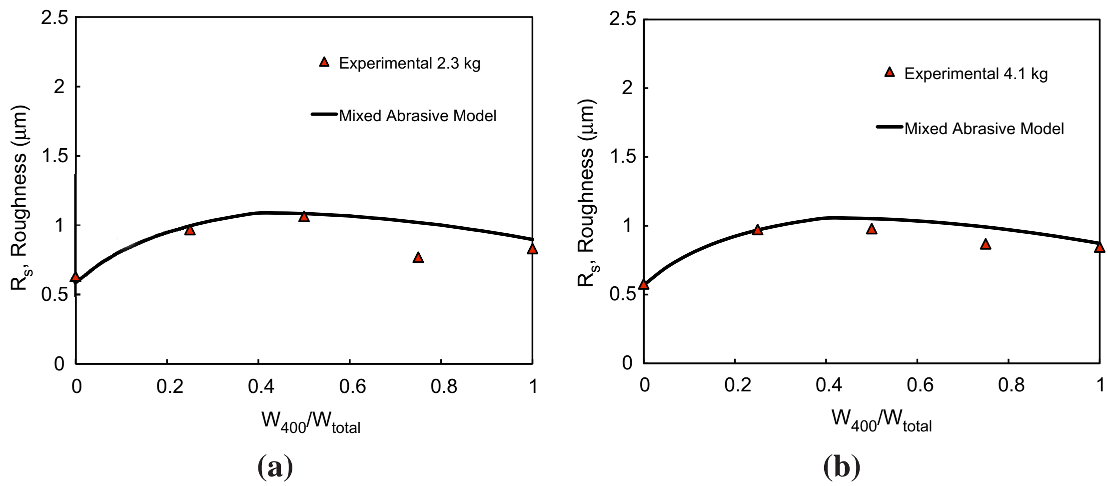

Figure 5.9: Plot of the mixed abrasive model and the experiemntally measured roughness as a function of F-400 particle concentration for (a) 2.3-kg and (b) 4.1-kg cases.

Table 5.5: The ratio between the material removal rate and the RMS surface roughness (unit: $1/\text{min}$)

	$\frac{W_{400}}{W_{total}} = 0$	0.25	0.50	0.75	1
2.3 kg (5 lbs)	1.6981	2.6259	3.1157	2.9344	2.7651
4.1 kg (9 lbs)	3.5904	5.2760	5.5372	5.6975	5.9447

due to the individual distributions having the opposite effect on roughness as a function of the concentration. As the normal load is changed, the roughness is found to have a small increase (Fig. 5.9 (a)) for a decreasing load (from 4.1 to 2.3 kg), resulting in a change in the active abrasive percentage from 3.29×10^{-5} to 1.75×10^{-5} after fitting with the experimental data. The decrease in the active abrasives occurs due to fewer large particles in the distribution becoming trapped between the platen and wafer resulting in less particles actively contributing to roughness generation by sliding contact. With fewer active particles, the load bearing on the active particles increases, which increases the particle penetration, and hence the roughness parameter. The slurry with single small abrasives seems to have much lower surface roughness comparing to those mixed with big abrasives.

5.5.3 Material removal rate versus surface roughness

Figure 5.8 shows material removal rate and surface roughness in the same figure at different loadings, respectively. From the results of this study, it is obvious that the mixed abrasives with the ratio of $\frac{W_{400}}{W_{total}} = 0.5$ has the highest material removal rate, and also with the highest surface roughness. The slurry with only F-600 abrasive grits has the lowest material removal rate, but the best surface quality. These two figures also show that higher material removal rate comes with the consequence of higher surface roughness in the free abrasive machining process under the same loading.

Table 5.5 shows the ratios of the material removal rate to the RMS surface roughness. In this table, the single small abrasive slurry has the smallest ratio, as expected. The difference between all the others is under 18%. It follows that the single smaller abrasive slurry,

Table 5.6: The increases of material removal rate (MRR) and RMS surface roughness from pure F-600 and F-400 to $1:1$ mixed abrasive slurries

		MRR	Roughness
2.3 kg	F-600 v.s. Mixed($1:1$)	209%	69%
	F-400 v.s. Mixed	44%	28%
4.1 kg	F-600 v.s. Mixed	62%	70%
	F-400 v.s. Mixed	7.8%	15%

F-600, has a different ratio of MRR to surface roughness from the other mixed abrasive slurries.

The material removal rate follows for the most part a Prestonian relationship [81], where the MRR is proportional to the applied pressure, or load. What the Prestonian relationship does not consider is the interaction of the mixed abrasive particle distributions. Here, the MRR follows a near identical trend as was observed for the wafer surface roughness after lapping. Choi et al. [20] observed similar changes in the MRR as a function of particle size. Though those authors were only considering a single abrasive distribution, for increasing particle diameter a higher MRR was observed. This is effectively the relationship observed in Fig. 5.8, where as a higher concentration of F-400 particles are added, the MRR increases. The continued increase of the MRR, which begins to decrease (Fig. 5.8a) or actually level-off (Fig. 5.8b) after the $1:1$ mixing ratio can be caused by the initiation of rolling-sliding contact with an increase in the percent solids, i.e. particle concentration [20]. The roughness model presented in this chapter predicts a larger number of active abrasives for the higher load (4.1 kg) case, which will in turn create more contact points for material removal to occur, leading to an increased MRR at higher loads.

The main objectives of wafer lapping is to remove the layer of subsurface damage due to slicing and global planarization. It is of interest in the lapping process to have large MRR to save process time. Slight increase in surface roughness can be taken care of in the subsequent polishing processes, as long as further subsurface damage is not introduced. From Table 5.6, we found that MRR is increased with $1:1$ mixing ratio, especially for

the $2.3\,\mathrm{kg}$ loading. This increase of MRR observed in experiments is explained by the proposed model through the interation of abrasive grits of two different sizes.

Overall, the mixed abrasive slurry performs in a similar manner to the single larger abrasive grit in both material removal and surface roughness. The slurry with the single smaller abrasive, on the other hand, performs differently from the others, indicating that any addition of F-400 particles will alter the material removal rate. Furthermore, the $1:1$ mixing ratio removed more material, but resulted in a slightly higher surface roughness, due to interaction between two grades of abrasive grits.

5.6 Summary

In this study, two different sizes of abrasive grits, F-400 and F-600, are mixed in five different ratios to conduct an experimental study of the use of mixed abrasive slurry in lapping processes. The results show that the mixed abrasives with the ratio of $\frac{W_{400}}{W_{total}} = 0.5$ has the highest material removal rate, accompanied by a slightly higher surface roughness. Higher loading always results in higher material removal rate regardless of the abrasive mixing ratios following a Prestonian relationship for material removal. However, the surface roughness does not correlate to the normal loading in a significant way. Although the reduction of surface roughness is one of the main purposes in lapping, the removal of subsurface damage is also important by quickly and efficiently taking down the layer of material with certain subsurface depth. The results in this study show a potential way of increasing the material removal rate for the coarse lapping process.

Although higher material removal rate usually comes at a cost of larger wafer surface roughness, when lapping at the same load, we have identified a way to increase MRR in lapping by $1:1$ mixing ratio of two grades of abrasive grits without extensively affecting the surface finish. The surface roughness and material removal rate were found to be dependent on the mixed abrasive grits. The interaction of different sizes of abrasive result in the surface roughness and material removal achieving maximums at the $1:1$ mixing ratio.

The interaction effect was integrated into a contact-based model that was able to explain the trends as a function of mixing ratios and applied load.

Lapping is a complicated machining process. Although much research has been conducted to understand the mechanisms of machining, many factors such as abrasive size effect and mixed distributions remain unknown [57] in the lapping process, and will be topics of future study. Nevertheless, it is observed from the results presented in this chapter that the change of distribution of abrasive grits will influence the material removal rate, surface roughness, and relative angular velocity between the jig and rotating lapping platform.

Chapter 6

Wafer Surface Polishing by Carbon Nanotube Brush

The purpose of the study in this chapter is to study the feasibility of surface polishing of brittle materials by carbon nanotube (CNT) brush. Preliminary experiments were conducted. Silicon and Lithium Niobate were both machined and observed under SEM and AFM after machining. Although the experiments were preliminary, the results provide a potential prototype of CNT-brushing on brittle materials and show the potential of this kind of tool.

6.1 Ductile-Regime Machining

During the machining of brittle materials, it is well accepted that the model of subsurface cracks caused by abrasive indentation, which was first proposed by Lawn [52], is the major reason of material removal [11, 12, 16]. Nonetheless, research showed that brittle materials can change its phase under high pressure, which is called High Pressure Phase Transformation (HPPT) [35]. Accordingly, it is possible to machine brittle materials under ductile regime with small depth of cut [9, 15]. In this situation, the relatively brittle materials can be machined like ductile materials and subject to ductile machining by shear. To investigate this phenomenon, a lot of research has been done during the last 20 years [72]. Different brittle materials, such as silicon [69, 73, 86, 102], silicon nitride [51], and silicon carbide [74, 75], were studied. Most of these studies were done by a single-point diamond

turning (SPDT) tool, which is an effective cutting tool for the ductile-regime machining of brittle material. However, an obvious disadvantage of this tool is that it will take an enormous amount of time to machine a large surface area such as silicon wafers. Therefore, the idea of using CNT brush as cutting tool is investigated as an alternative for ductile machining of wafer surface.

6.2 Experimental Setup

6.2.1 Fabrication of CNT brush

There are three main methods to grow CNTs: (i) arc discharge, (ii) laser ablation, and (iii) chemical vapor deposition (CVD) techniques. CVD is the only method to produce large CNT forest. The CNT forests used in this experiment are made by the CVD method.

Figure 6.1 illustrates the fabrication process of CNT brush. CNT forest was transfered from the original silicon substrate surface to the base of the tool which can be silicon wafer or steel. Epoxy glue was chosen as adhesive because it would not shrink after being dried, and will not cause the CNT forest to deform. Figure 6.2 shows the size of a CNT brush compared to a penny.

6.2.2 Experimental devices

Two devices were used for the experiments. The first one is a combination of a single-axis moving platform and a jig which can control the depth of cut up to 10 μm, as showed in Figure 6.3. Workpiece is mounted on the platform while the CNT brush is on the jig. The cutting speed is managed by hand. In order to measure the initial contact of CNT brush and the workpiece surface, a thin layer of gold was deposited on the surface of the workpiece. Since carbon nanotube is conductive, a close-loop circuit would be formed when the CNT makes contact with the layer of gold on the surface of the wafer. The depth of cut will be controlled manually from the point of initial contact.

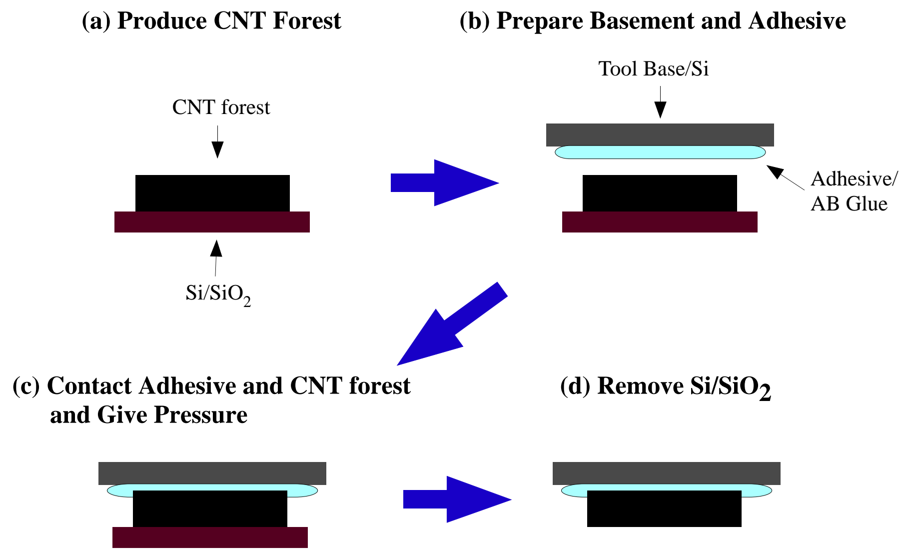

Figure 6.1: Fabrication of CNT brush by growing vertically aligned CNTs.

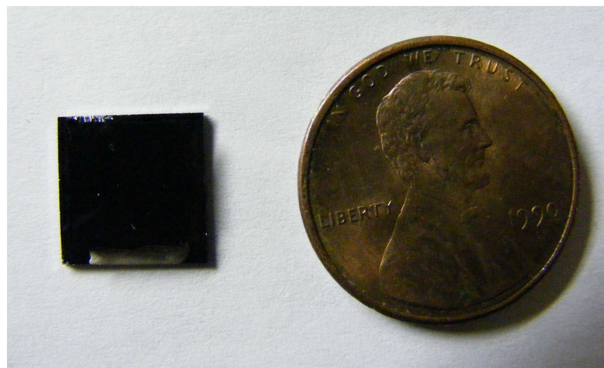

(a)

(b)

Figure 6.2: CNT brush compared to a penny

In order to achieve the smaller depth of cut, an Atomic Forced Microscope (AFM) was modified to conduct the experiment, as showed in Figure 6.4. The step of this AFM in z-direction (vertical direction) can be as precise as 400 nm. An acrylic jig was designed to replace the original delicate component in the AFM. A hard disk drive was used as the platform on which the workpiece was mounted by wax. The angular speed of the hard disk is 4500 rpm. The cutting speed can be calculated by the distance from machining position to the center of the spindle axis of the hard disk. In order to avoid the initial contact problem, the depth of cut was increased gradually during the machining process.

6.3 Results of Experiments

In the following sections, the results of experiments using different wafer substrates are discussed.

6.3.1 Polished silicon wafer

The polished silicon was brushed by the tool shown in Figure 6.3. Because the platform was controlled by hand, the cutting speed was roughly $0.5 \sim 1$ m/s. Scratches were found when the depth of cut was over 50 μm, which was much larger than the ductile-regime machining conducted by SPDT. These may be due to the buckling deformation of CNT forest, and the alignment of CNT forest during machining shown in Figure 6.5. Figures 6.6 and 6.7 show the wafer surface after machining. Experiments were also conducted under the modified AFM machine. However, there was no obvious machined mark on the workpiece.

6.3.2 Lapped silicon wafer

In order to control the depth of cut more precisely, the modified AFM was used to machine a lapped silicon wafer. The preliminary experiment showed no tool marks on the

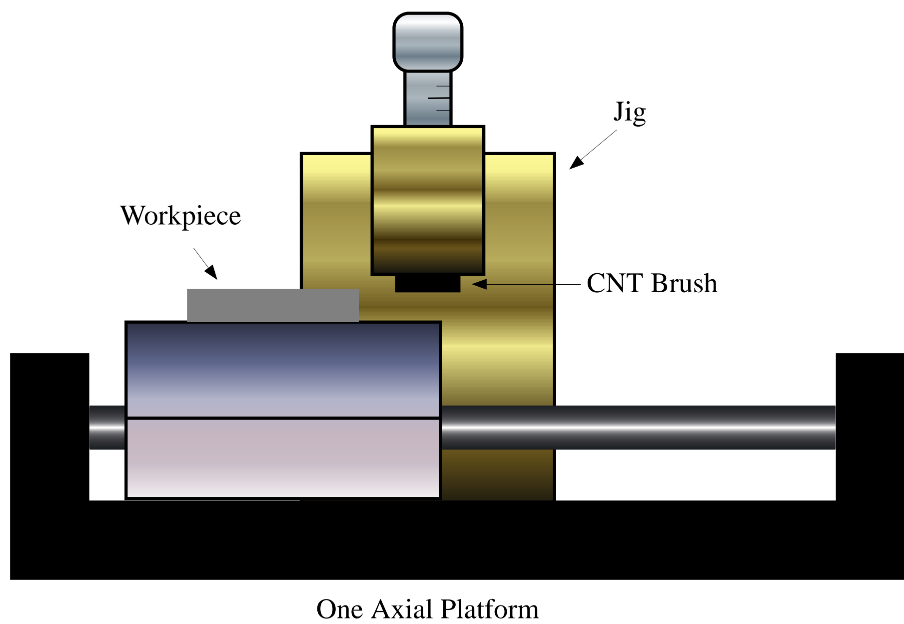

Figure 6.3: Manual operating single-axis platform

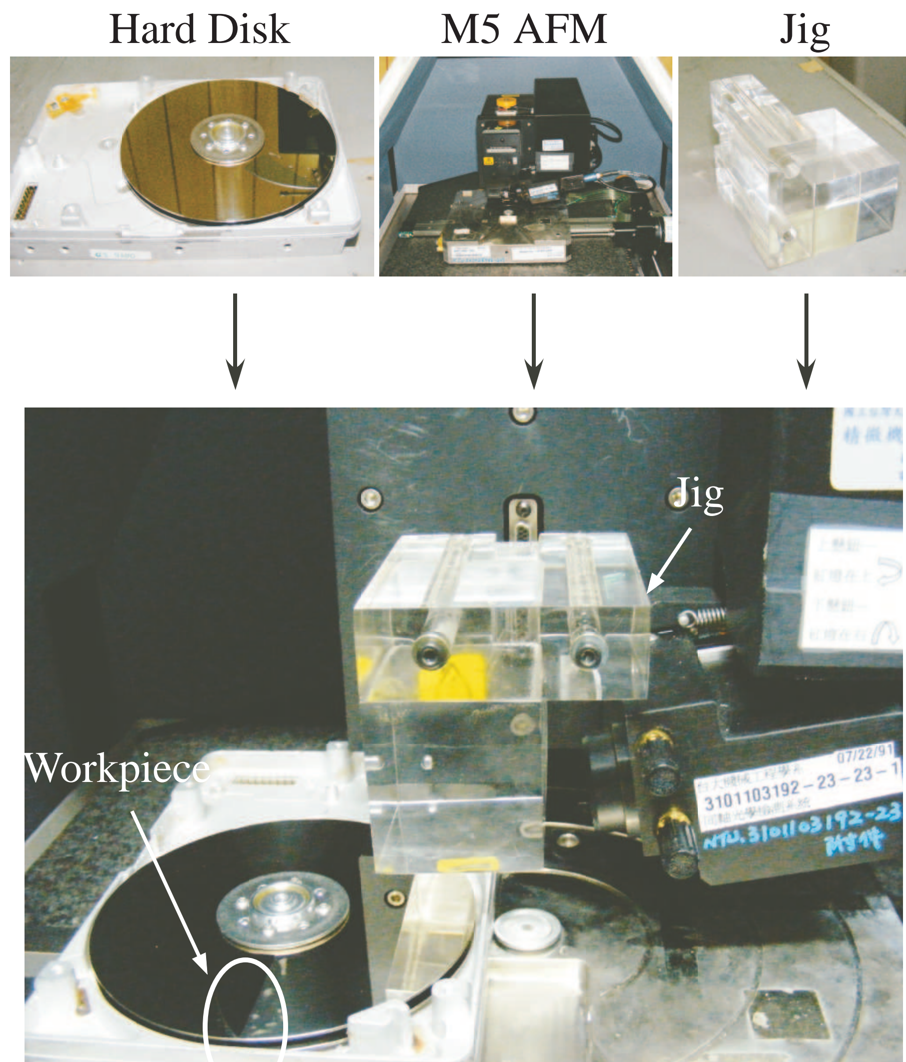

Figure 6.4: Modified AFM as machining device.

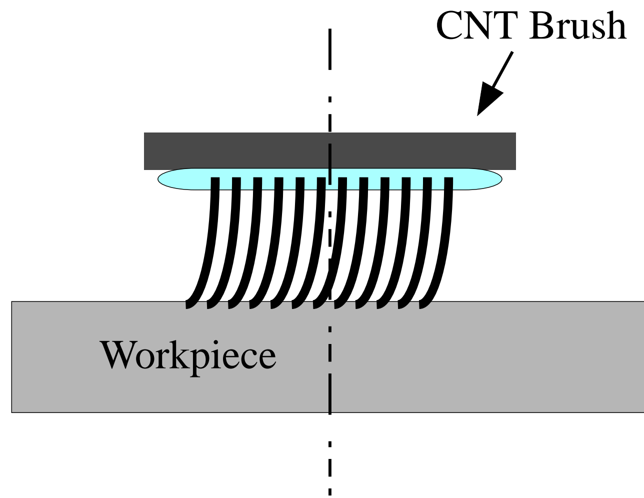

Figure 6.5: CNT forest deformation during machining.

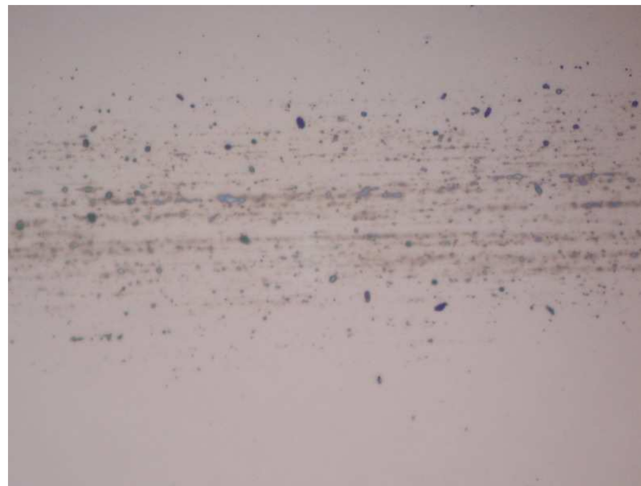

Figure 6.6: Polished silicon wafer surface after CNT brushing, observed by an optical microscope.

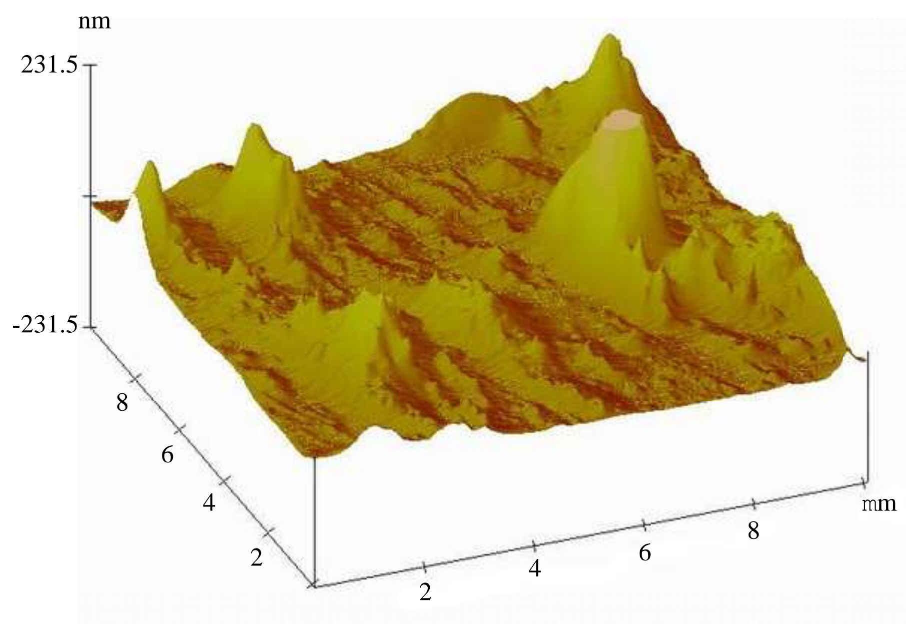

Figure 6.7: Polished silicon wafer surface after CNT brushing, observed by an atomic force microscope.

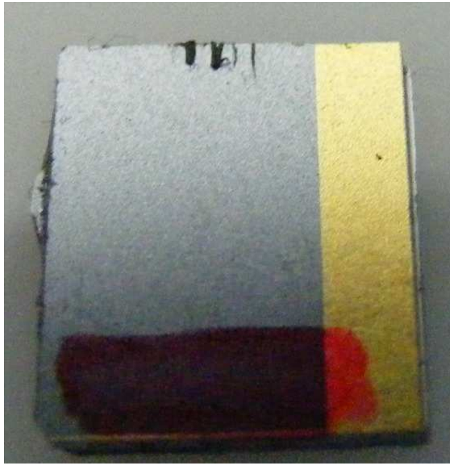

Figure 6.8: Lapped silicon wafer surface after CNT brushing.

workpiece surface, but only the residual carbon nanotubes. Figure 6.8 shows the residual of CNTs. Figure 6.9 shows the observation under a Scanning Electron Microscope (SEM).

6.3.3 Lithium niobate

Lithium Niobate is a brittle material used in opto-electronic device fabrication. It is softer than silicon, and is expected to be easier for machining. Modified AFM was utilized to machine Lithium Niobate with CNT brush. The cutting speed was in the range of 1.5 $\sim$ 3 m/s. The depth of cut was increased by a total of 100 $\sim$ 200 μm in 5 seconds during machining. After machining, there were residual CNTs on the workpiece surface. However, the tool marks can be clearly observed after cleaning the workpiece by ultrasonic cleaner, as shown in Figure 6.10. Figures 6.11 and 6.12 show the machined and original surface under AFM, respectively. The tool marks also can be easily distinguished.

6.4 Discussions

Ductile machining is a process of material removal without causing subsurface cracks. From the experimental results in the previous sections, it seems that the CNT brush can be used for ductile machining. However, there are some concerns here. First, the tool mark

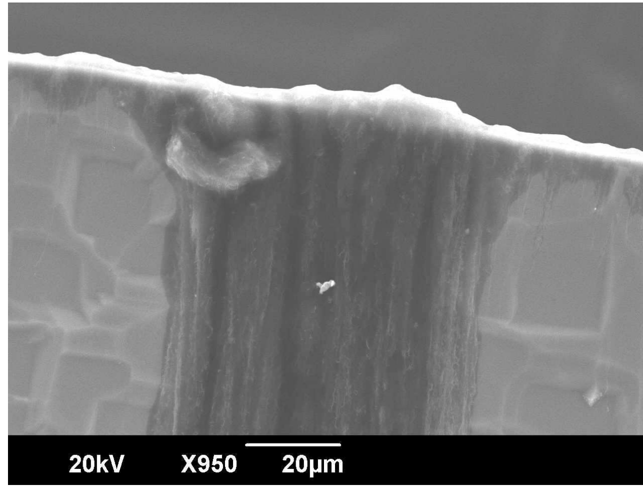

Figure 6.9: Lapped silicon wafer surface after CNT brushing, observed by SEM.

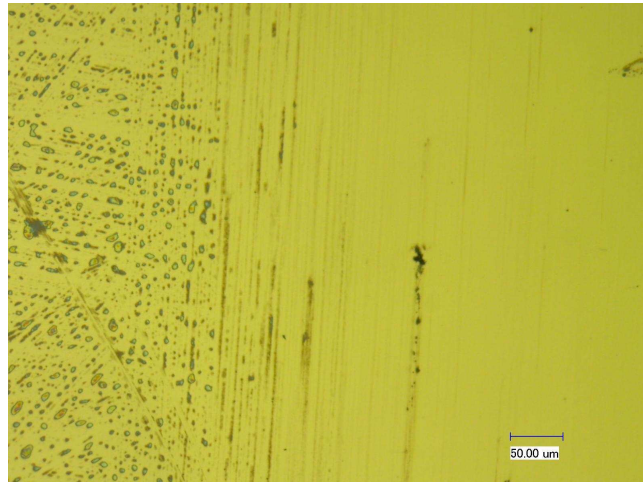

Figure 6.10: Lithium Niobate surface after CNT brushing, observed by an optical microscope.

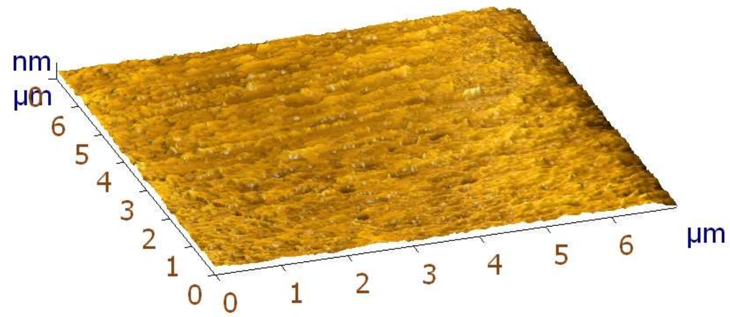

Figure 6.11: The tool marks on the Lithium Niobate surface after CNT brushing, observed by AFM.

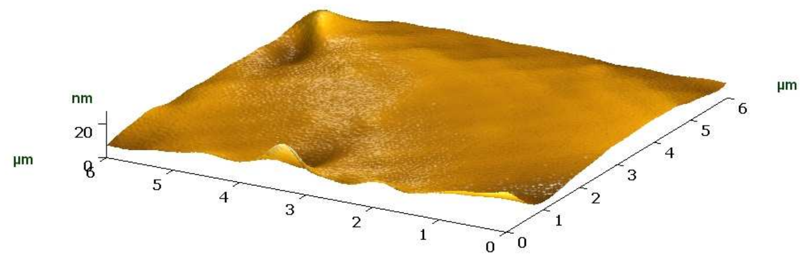

Figure 6.12: The original Lithium Niobate surface, observed by AFM.

shows the evidence of machining, but it can not be confirmed that if the material is indeed removed or just deformed. Secondly, the residual CNTs after machining may be an issue for the environment. Third, the existence or lacks of subsurface damages need to be examined.

The CNT brush was also observed after the machining process. The CNT brush was found to buckle and deform during the machining. That can be a reason why the higher depth of cut is necessary to machine the material than that in the Single Point Diamond Turning, which accomplishes ductile-regime machining under 1 μm. Figure 6.13 shows the wrinkle and buckling of CNT brush after machining.

There were suspected chips due to ductile machining observed on the CNT brush surface as shown in Figure 6.14. These "chips" need to be confirmed by the Energy-Dispersive X-ray Spectroscopy (EDX or EDS).

6.5 Summary

In this chapter, preliminary experiments of ductile machining using CNT brushes on brittle materials are presented. The results show the potential of polishing brittle material surface by CNT brush, especially for Lithium Niobate. Ductile-regime machining needs a very high-precision operation, including machining parameters such as the depth of cut, cutting velocity, and rake angle. To further study the feasibility of ductile machining on the surface of silicon wafers, more experiments with precise machine tools are necessary.

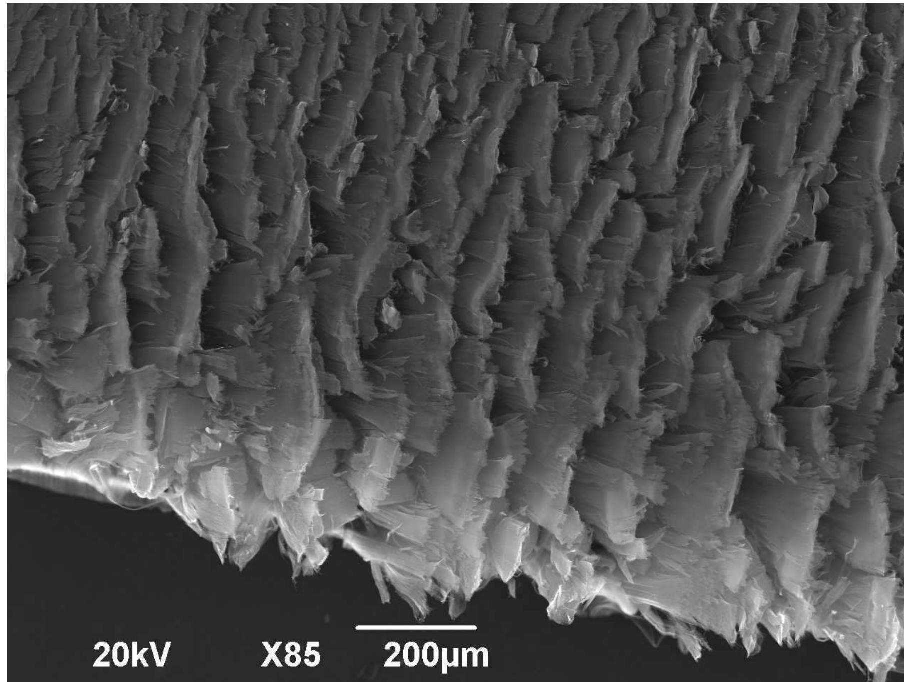

Figure 6.13: Wrinkle on CNT forest after machining

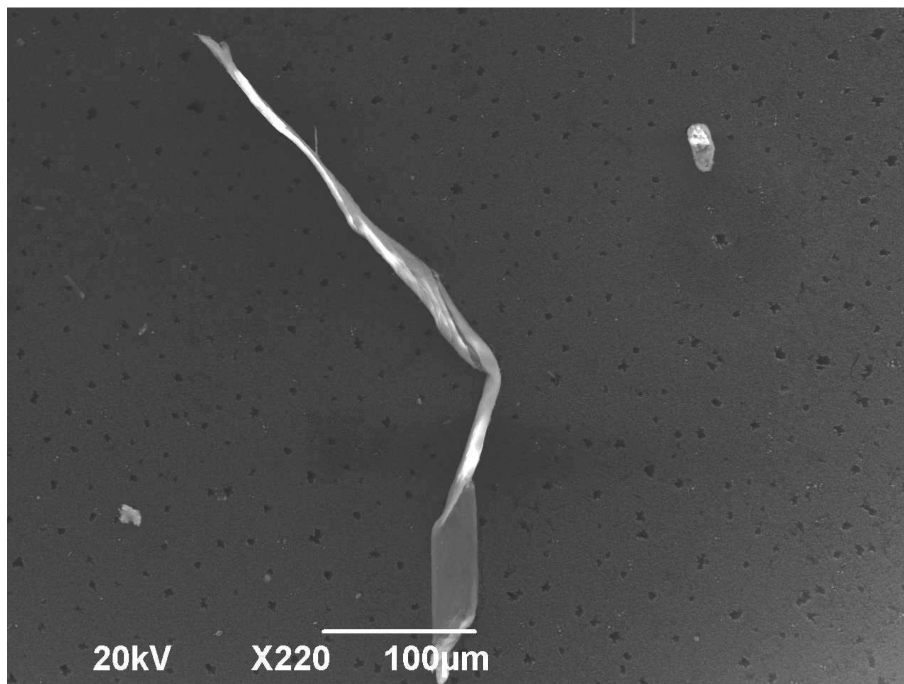

Figure 6.14: Suspected Lithium Niobate chip on the surface of a CNT brush

Chapter 7

Conclusions and Future Work

In this dissertation, wafer manufacturing processes were studied. The research topics include vibration response of the wire in slurry wiresaw system, effect of mixed abrasive grits in lapping process, and wafer surface finishing by carbon nanotube brush. Based on the topics, the conclusions and future work will be given in the following.

7.1 Vibration Response of the Wire in Slurry Wiresaw System

7.1.1 Conclusion

The closed-form solutions of free and forced vibration responses of damped axially moving wire have been solved in Chapter 2 and Chapter 4, respectively. The free vibration response was obtained by the classical modal analysis. The corresponding eigenvalues, eigenfunctions, and orthogonality were also derived. The analysis of the damped behavior was presented in Chapter 3. The damping ratios, ζ_ω and ζ_θ, and damping index, s, were defined. The results also showed that the increase of wire speed will increase the damping ratio, which is called "apparent damping effect". The mode shapes were affected by the wire speeds. The imaginary parts of the mode shapes are excited with the increase of wire speed. A brief estimation of the damping factor in slurry wiresaw system was provided, as well as the corresponding analysis with respect to realistic and relevant parameters.

Because of the non-self-adjoint property, the forced vibration response has to be solved by Green's function, as presented in Chapter 4. The poles of the Green's function in the s-domain of Laplace transform are actually the eigenvalues, and the results show that the Green's function is a combination of the eigenfunctions and adjoint eigenfunctions. By the method of the standard form, the free vibration response can also be derived by using the Green's function. The results showed agreement with those in Chapter 2. With the solution of forced vibration response, the frequency response with a point excitation is also obtained.

7.1.2 Future work

In this dissertation, the research of slurry wiresaw system focused on the theoretical study on the vibration responses of the wire. However, a practical application to improve the wiresaw performance is the main purpose of this study. Based on the research results presented, the following future work is proposed:

- Active and passive control of damped axially moving wire
- Effect of vibration on the surface and subsurface quality

7.1.2.1 Active and passive control of damped axially moving wire

The Laplace transform of the Green's function is actually the transfer function, which is utilized in the feedback control under s-domain [13]. The advantage of using the Green's function is that the closed-form solution includes all the modes, and the method of approximation or truncation is not necessary. In addition, with point sensing and point actuation, as shown in Figure 7.1, the feedback control law can be achieved [13]. In Figure 7.1, $G(x, \xi, s)$ is the transfer function (Laplace transform of the Green's function) of the system, $\bar{f}(x, s)$ is the input, $\bar{u}(x, s)$ is the output, a is the position of the sensor, b is the position of the actuator, and $K(s)$ is the feedback control law which needs to be designed.

The transfer function $W(x,\xi,s)$ of the closed control system is

$$W(x,\xi,s) = G(x,\xi,s) + \frac{G(x,b,s)G(a,\xi,s)K(x)}{1 - G(a,b,s)K(s)}$$

Yang and Mote applied the Green's function on the control of axially moving string without damping [103–105]. However, the modern optimal or robust control theory should be able to be employed to design a more appropriate control law. In addition, a passive control was developed by employing journal bearing for axially moving string [90, 91]. All of these approaches can be considered to reduced the vibration response of the wire in slurry wiresaw systems.

7.1.2.2 The effect of vibration on the surface and subsurface quality

During slicing process, the motion of the wire drives the free abrasive grits to move and to impact against the workpiece, as shown in Figure 7.2. The damage in transverse direction is necessary to slice the ingot. However, the damage in lateral direction will result in undesirable surface roughness and subsurface damage. In addition, wiresawing introduces other surface topography such as wire marks and waviness which were not found in conventional ID saw. Therefore, the dynamics of the wire motion could have potential influence on the the surface and subsurface quality.

Research shows that the vibration amplitude of the wire of modern slurry wiresaw can be up to 50 μm with no slurry and no workpiece [62]. The oscillation is due to the geometric tolerance of the roller grooves and other disturbances. In an actual slicing operation, the energy of vibration is expected to result in damages on the wafer surface when the wire travels in the cutting tunnel. The dynamics of **intermittent motion** has been studied for oilwell drillstrings [21, 108–110] and mechanical joints with clearances [30, 31, 50]. Further study is required for modern wiresaw system.

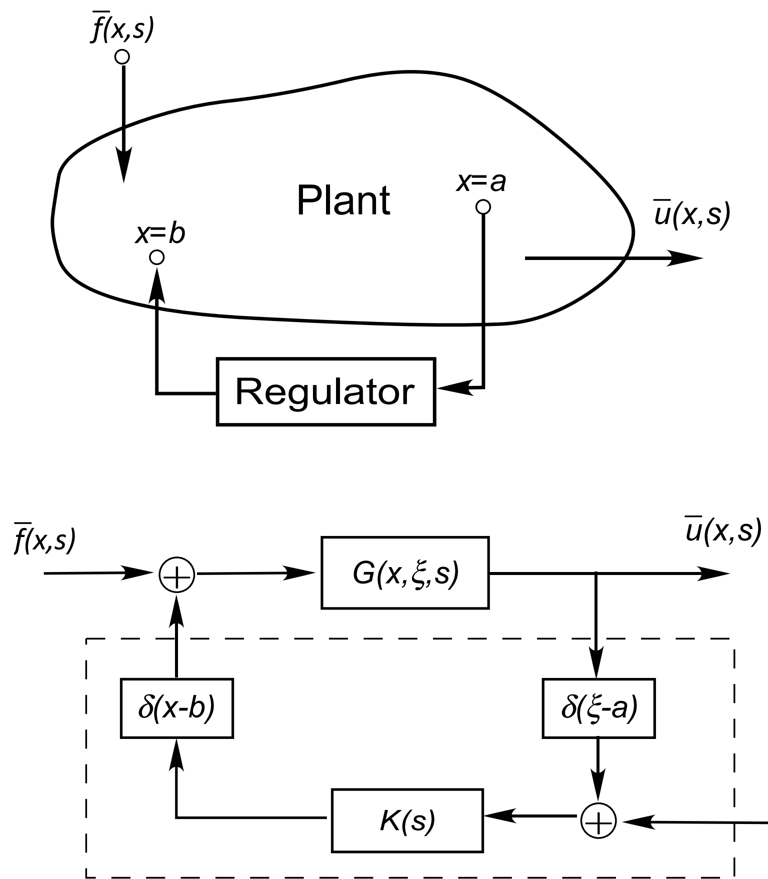

Figure 7.1: Feedback control of distributed system with point sensing and point actuation [13]

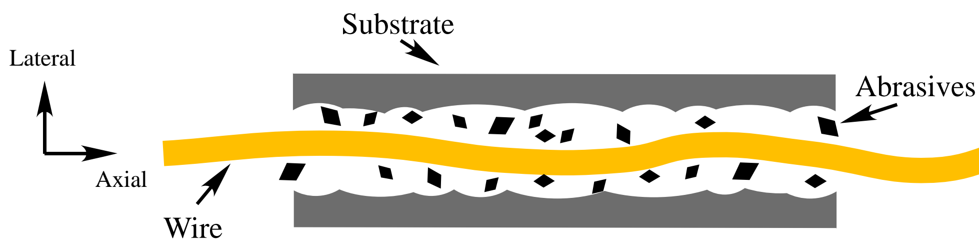

Figure 7.2: Schematic of wire and free abrasives in slurry wiresaw system

7.2 Effect of Mixed Abrasive Grits in Lapping Process

7.2.1 Conclusion

In this study, two different sizes of abrasive grits, F-400 and F-600, were mixed in five different ratios to conduct an experimental study for the use of mixed abrasive slurry in lapping process. The results show that the $1:1$ mixing ratio of abrasive grits has the highest material removal rate, accompanied by a slightly higher surface roughness. Higher loading always results in higher material removal rate regardless of the abrasive mixing ratios, following a Prestonian relationship for material removal. However, the surface roughness does not correlate with the normal loading in a significant way. The interaction effect was integrated into a contact-based model that was able to explain the trends as a function of mixing ratios and applied loads.

Although the reduction of surface roughness is one of the main purposes in lapping, the removal of subsurface damage is also important by quickly and efficiently taking down the layer of material with certain subsurface depth. The results in this study show a potential way of increasing the material removal rate for the coarse (first) lapping process, before the fine (finishing) lapping process.

7.2.2 Future work

The study of mixed abrasive effect shows interesting results; however, it also aroused more questions in the free abrasive machining process and tribology. In Chapter 5, the mean sizes of F-400 and F-600 SiC grits are about the ratio of $2:1$ (17.3 μm to 9.3 μm). It will be interesting to investigate mixing of grit sizes with different ratios of their mean sizes. On the other hand, it is expected that the surface morphology would be more homogeneous if the deviation of the size distribution is limited. Another interesting research can be mixing two different kinds of abrasive grits such as Boron Carbide and Silicon Carbide. Boron

Carbide is an expensive material, which are utilized for machining harder material such as sapphire. If the mixed abrasives could have similar performance as single Boron Carbide abrasives, the machining cost will be reduced.

The subsurface damage is another issue which was not discussed in this dissertation. The subsurface damages can affect the yield of the end products. Therefore, a good flattening process should be able to reduce the layer of subsurface damages introduced by the slicing process. Either lapping or grinding can introduce the subsurface damages. However, these damages should not exceed those from slicing process, and will be removed by polishing.

7.3 Wafer Surface Finishing by Carbon Nanotube Brush

7.3.1 Conclusion

The utilization of CNT brush on finishing wafer surface was studied and presented in Chapter 6. The results show promising method to perform ductile machining on brittle materials using the CNT brush. However, more experiments and modeling are required, along with better machine tool and CNT brush design, in order to further study this technique.

7.3.2 Future work

Based on the results presented in Chapter 6, further improvement of the experimental process and machine is required to obtain better outcomes. The following consideration is necessary.

(1) Increase the stiffness of CNT brushes to conduct experimental study of their effectiveness.

(2) Design a better and more accurate machine tool.

Bibliography

[1] Semi draft document 3089: Guide for reporting wafer nanotopography.

[2] Y. Abe, T. Hamasaki, K.-I. Ishikawa, and H. Suwabe. Development and slicing performance of high accuracy multi-wire saw: Effect of table feed accuracy and thermal deformation of frame on slicing accuracy. In *Proceedings of ASPE 22nd Annual Meeting*, Dallas, Texas, October 14-19 2007. ASPE.

[3] Y. Abe, K.-I. Ishikawa, and H. Suwabe. Effects of thermal deformation of multi-wire saw's wire guides and ingot on slicing accuracy. *Key Engineering Materials*, 389-390:442 – 447, 2009.

[4] M. Bhagavat, V. Prasad, and I. Kao. Elasto-hydrodynamic interaction in the free abrasive wafer slicing using a wiresaw: Modeling and finite element analysis. *Journal of Tribology*, 122(2):394–404, April 2000.

[5] S. Bhagavat and I. Kao. Ultra-low load multiple indentation response of materials: In purview of wiresaw slicing and other free abrasive machining (FAM) processes. *International Journal of Machine Tools and Manufacture*, 46(5):531–541, 2006.

[6] S. Bhagavat and I. Kao. A finite element analysis of temperature variation in silicon wafers during wiresaw slicing. *International Journal of Machine Tools and Manufacture*, 48/1:95–106, 2007.

[7] S. Bhagavat, J. Liberato, and I. Kao. Effects of mixed abrasive slurries on free abrasive machining processes. In *Proceedings of the 2005 ASPE Conference*. ASPE, October 2005.

[8] S. Bhagavat, J. C. Liberato, C. Chung, and I. Kao. Effects of mixed abrasive grits in slurries on free abrasive machining (fam) processes. *International Journal of Machine Tools & Manufacture*, 50:843 – 847, 2010.

[9] T. Bifano, T. Dow, and R. Scattergood. Ductile-regime grinding: A new technology for machining of brittle materials. *Journal of Engineering for Industry*, 113:184–189, 1991.

[10] N. J. Brown, P. C. Baker, and R. T. Maney. Optical polishing of metals. In *Proceedings of SPIE*, volume 306, pages 42–57, 1981.

[11] M. Buijs and K. K. Houten. A model for lapping of glass. *Journal of Materials Science*, 28:3014–3020, 1993.

[12] M. Buijs and K. K. Houten. Three-body abrasion of brittle materials as studied by lapping. *Wear*, 166:237–245, 1993.

[13] A. G. Butkovskiy. *Structural Theory of Distributed Systems*. Ellis Horwood Limited, West Sussex, England, 1983.

[14] A. G. Butkovskiy and L. M. Pustyl'nikov. *Characteristics of Distributed-parameter Systems: Handbook of Equations of Mathematical Physics and Distributed-parameter Systems*. Kluwer Academic Publishers, Dordrecht, The Netherlands, 1993.

[15] Y. P. Chang, M. Hashimura, and D. A. Dornfeld. An investigation of material removal mechanisms in lapping with grain size transition. *Journal of Manufacturing Science and Engineering*, 122:413–419, 2000.

[16] R. Chauhan, Y. Ahn, S. Chandrasekar, and T. N. Farris. Role of indentation fracture in free abrasive machining of ceramics. *Wear*, 162-164:246–257, 1993.

[17] J.-S. Chen. Natural frequencies and stability of an axially-traveling string in contact with a stationary load system. *Journal of Vibration and Acoustics*, 119:152 – 157, 1997.

[18] L. Chen. Analysis and control of transverse vibrations of axially moving strings. *Applied Mechanics Reviews*, 58(1-6):91 – 115, 2005.

[19] C. Chien, J. K. Wang, T. Chang, and W. Wu. Economic analysis of 450mm wafer migration. In *IEEE International Symposium on Semiconductor Manufacturing Conference Proceedings, 2007 International Symposium on Semiconductor Manufacturing, ISSM - Conference Proceedings*, pages 283–286, 2007.

[20] W. Choi, J. Abiade, S.-M. Lee, and R.K. Singh. Effects of slurry particles on silicon dioxide cmp. *Journal of the Electrochemical Society*, 151(8):G512–G522, 2004.

[21] A. P. Christoforou and A. S. Yigit. Dynamic modelling of rotating drillstrings with borehole interactions. *Journal of Sound and Vibration*, 206(2):243 –260, 1997.

[22] C. Chung and I. Kao. Comparison of free abrasive machining processes in wafer manufacturing. In *Proceedings of International Manufacturing Science and Engineering Conference (MSEC 2008)*, number ASME Paper number MSEC2008-72253. ASME, October 2008.

[23] C. Chung and I. Kao. Damped vibration response at different speeds of wire in slurry wiresaw manufacturing operations. In *Proceedings of International Manufacturing Science and Engineering Conference (MSEC 2008)*, number ASME Paper number MSEC2008-72213. ASME, October 2008.

[24] C. Chung and I. Kao. Numerical studies on the frequency response of vibration of damped axially moving wire. In *Proceedings of International Design Engineering Technical Conferences (IDETC2009)*, number ASME Paper number DETC2009-86880. ASME, August-September 2009.

[25] C. Chung and I. Kao. Modeling of axially moving wire with damping: Eigenfunctions, orthogonality and applications in slurry wiresaws. *submitted to Journal of Sound and Vibration*, 2010.

[26] C. Chung, C. S. Korach, and I. Kao. Experimental study and modeling of lapping using abrasive grits with mixed sizes in free abrasive machining (fam). *submitted to Jouranl of Manufacturing Science and Engineering, Transactions of the ASME*, 2010.

[27] L. M. Cook. Chemical processes in glass polishing. *Journal of Non-Crystalline Solids*, 120:152–171, 1990.

[28] J. Draina, D. Fandel, J. Ferrell, and S. Kramer. Lessons learned from the 300mm transition. *ECS Transactions*, 2(2):135–154, 2006. Silicon Materials Science and Technology X.

[29] M. S. Dresselhaus, G. Dresslhaus, and Ph. Avouris. *Carbon Nanotubes: Synthesis, Structure, Properties, and Applications*. Springer, 2001.

[30] S. Dubowsky and F. Freudenstein. Dynamic analysis of mechanical systems with clearances-1. *Journal of Engineering for Industry, Transactions of the ASME*, 93(1):305–309, 1971.

[31] S. Dubowsky and F. Freudenstein. Dynamic analysis of mechanical systems with clearances-2. *Journal of Engineering for Industry, Transactions of the ASME*, 93(1):310–316, 1971.

[32] D. G. Duffy. *Green's Functions with Applications Studies in Advanced Mathematics*. CRC Press LLC, Boca Raton, Florida, 2001.

[33] H. F. Erk. Challenges in wafering processes for semiconductor and solar wafers. In *ECS Transactions - ISTC/CSTIC 2009 (CISTC)*, volume 18, pages 969 – 981, Shanghai, China, March 2009.

[34] L. Fang, X. L. Kong, J. Y. Su, and Q. D. Zhou. Movement patterns of abrasive particles in three-body abrasive. *Wear*, 162-164:782–789, 1993.

[35] Y. Gogotsi and V. Domnich, editors. *High-Pressure Surface Science and Engineering*. IoP(Institute of Physics), UK, 2004.

[36] Michael D. Greenberg. *Advanced Engineering Mathematics*. Prentice-Hall International, Inc., 1998.

[37] A. Hand. Ismi updates goals, challenges of 450 mm wafers. *Semiconductor International*, 30(1):24, January 2007.

[38] U. Heisel and J. Avroutine. Process analysis for the evaluation of the surface formation and removal rate in lapping. *CIRP Annals - Manufacturing Technology*, 50(1):229–232, 2001.

[39] Hologenix. Wafer geometry characteristics. Website. http://www.hologenix.com/Wafer-Geo-Characteristics.pdf.

[40] F. Y. Huang and C. D. Mote. On the translating damping caused by a thin viscous fluid layer between a translating string and a translating rigid surface. *Journal of Sound and Vibration*, 181(2):251 – 260, 1995.

[41] P. K. Huang. Nano-brushing using carbon nanotube forest. Master thesis, Graduate Institute of Mechanical Engineering, National Taiwan University, Taiwan, July 2007.

[42] D. J. Inman. *Vibration with Control*. Wiley, 2006.

[43] Intel News Release. Intel, Samsung Electronics, TSMC reach agreement for 450mm wafer manufacturing transition. Website, May 2008. http://www.intel.com/pressroom/archive/releases/20080505corp.htm?iid=SEARCH.

[44] K.-I. Ishikawa, H. Suwabe, and S. Itoh. Study on slurry actions in slicing groove and slicing characteristics at multi-wire saw. In *Proceedings of ASPE 18th Annual Meeting*, Porland, Oregon, 2003. ASPE.

[45] K.-I. Ishikawa, H. Suwabe, S. Itoh, and M. Uneda. A basic study on the behavior of slurry action at multi-wire saw. *Key Engineering Materials*, 238-239:89 – 92, 2003.

[46] ITRS. International technology roadmap for semiconductors 2005 edition. Website, 2005. http://www.itrs.net/.

[47] ITRS. International technology roadmap for semiconductors, 2008 update front end processes. Website, 2008. http://www.itrs.net/Links/2008ITRS/Home2008.htm.

[48] I. Kao. Technology and research of slurry wiresaw manufacturing systems in wafer slicing with free abrasive machining. *the International Journal of Advanced Manufacturing Systems*, 7(2):7–20, 2004.

[49] I. Kao, C. Chung, and R. Rodriguez. *Modern Wafer Manufacturing and Slicing of Crystalline Ingots to Wafers Using Modern Wiresaw*. Springer Publisher, 2010. Book Chapter in Springer Handbook of Crystal Growth edited by G. Dhanaraj, K. Byrappa, V. Prasad, and M. Dudley.

[50] Y. A. Khulief and A. A. Shabana. Dynamic analysis of constrained system of rigid and flexible bodies with intermittent motion. *Journal of Mechanisms, Transmissions, and Automation in Design, Transactions of the ASME*, 108:38 – 45, 1986.

[51] T. G. Kumbera, H. P. Cherukuri, J. A. Patten, C. J. Brand, and T. D. Marusich. Numerical simulations of ductile machining of silicon nitride with a cutting tool of define geometry. *Machining Science and Technology*, 5(3):341–352, 2001.

[52] B. Lawn. *Fracture of Brittle Solids – Second Edition*. Cambridge University Press, Cambridge, United Kingdom, 1993. ISBN: 0521409721.

[53] K.-Y. Lee and A. A. Renshaw. Solution of the moving mass problem using complex eigenfunction expansions. *Journal of Applied Mechanics*, 67:823 – 827, 2000.

[54] J. Li, I. Kao, and V. Prasad. Modeling stresses of contacts in wiresaw slicing of polycrystalline and crystalline ingots: Application to silicon wafer production. *Journal of Electronic Packaging*, 120(2):123–128, June 1998.

[55] Z.C. Li, Z.J. Pei, and Graham R. Fisher. Simultaneous double side grinding of silicon wafers: a literature review. *International Journal of Machine Tools and Manufacture*, 46:1449–1458, 2006.

[56] W. Liu, Z. J. Pei, and X. J. Xin. Finite element analysis for grinding and lapping of wire-sawn silicon wafers. *Journal of Materials Processing Technology*, 129(1-3):2–9, 2002.

[57] I. D. Marinescu, E. Uhlmann, and T. K. Doi, editors. *Handbook of Lapping and Polishing*. CRC Press, Florida, USA, 2007.

[58] J. H. Mathews and R. W. Howell. *Complex Analysis for Mathematics and Engineering*. Jones & Bartlett Learning, 5th edition, 2006.

[59] L. Meirovitch. A new method of solution of the eigenvalue problem for gyroscopic systems. *AIAA Journal*, 12:1337 – 1342, 1974.

[60] L. Meirovitch. A modal analysis for the response of linear gyroscopic systems. *ASME Journal of Applied Mechanics*, 42:446 – 450, 1975.

[61] L. Meirovitch. *Principles and Techniques of Vibrations*. Prentice Hall, 1st edition, 1997.

[62] M. Mizuno, T. Iyama, S. Kikuchi, and B. Zhang. Development of a device for measuring the transverse motion of a saw-wire. *Journal of Manufacturing Science and Engineering, Transactions of the ASME*, 128:826 – 834, August 2006.

[63] H. J. Moller. Basic mechanisms and models of multi-wire sawing. *Advanced Engineering Materials*, 6(7):501–513, 2004.

[64] H. J. Moller. Wafering of silicon crystals. *Phys. Stat. Sol.*, (a) 203(4):659–669, 2006.

[65] C. D. Mote. Dynamic stability of axially moving materials. *Shock and Vibration Digest*, 4(4):2 – 11, 1972.

[66] P. M. Nasch and R. Sumi. Meeting current and future wafering challenges. *Solid State Technology*, 52(3):32+34–36, March 2009.

[67] D. E. Newland. *An Introduction to Random Vibrations, Spectral & Wavelet Analysis*. Dover Publications, Mineola, New York, 3rd edition, 2005.

[68] T. Ng and R. Nallathamby. Optical evaluation of ingot fixity in semiconductor wafer slicing. *Optics and Laser Technology*, 36(8):641–645, 2004.

[69] B. P. O'Conner, E. R. Marsh, and J. A. Couey. On the effect of crystallographic orientation on ductile material removal in silicon. *Predision Engineering*, 29:124–132, 2005.

[70] T. C. Papanastasiou. *Applied Fluid Mechanics*. Prentice-Hall, 1994.

[71] R. G. Parker. Supercritical speed stability of the trivial equilibrium of an axially-moving string on an elastic foundation. *Journal of Sound and Vibration*, 221:205 – 219, 1999.

[72] J. Patten, H. Cherukuri, and J. Yan. *Ductile regime machining of semiconductors and ceramics*. IoP(Institute of Physics), 2004. Book Chapter in High Pressure Surface Science and Engineering edited by Y. Gogotsi and Y. Domnich.

[73] J. Patten and W. Gao. Extereme negative rake angle technique for single point diamond nano-cutting of silicon. *Journal of the International Societies for Precision Engineering and Nanotechnology*, 25:165–167, 2001.

[74] J. Patten, W. Gao, and K. Yasuto. Ductile regime nanomachining of single-crystal silicon carbide. *Journal of Manufacturing Science and Engineering, Transactions of the ASME*, 127:522–532, August 2005.

[75] J. A. Patten, J. Jacob, B. Bhattacharya, and A. Grevstad. Comparison between numerical simulations and experiments for single point diamond turning of silicon carbide. *Transactions of the North American Manufacturing Research Institution of SME*, 35:89–96, 2007.

[76] Z. Pei, G. Fisher, M. Bhagavat, and S. Kassir. A grinding-based manufacturing method for silicon wafers: an experimental investigation. *International Journal of Machine Tools and Manufacture*, 45(10):1140–1151, 2005.

[77] Z.J. Pei, G. R. Fisher, and J. Liu. Grinding of silicon wafers: A review from historical perspectives. *International Journal of Machine Tools and Manufacture*, 48:1297–1307, 2008.

[78] N. C. Perkins. Linear dynamics of a translating string on an elastic foundation. *Journal of Vibration and Acoustics*, 112:2–7, 1990.

[79] J. S. Pettinato and D. Pillai. Technology decisions to minimize 450-mm wafer size transition risk. *IEEE Transactions on Semiconductor Manufacturing*, 18(4):501–509, November 2005.

[80] K. Phillips, G. M. Crimes, and T. R. Wilshaw. On the mechanism of material removal by free abrasive grinding of glass and fused silica. *Wear*, 41:327–350, 1977.

[81] F. W. Preston. The theory and design of plate glass polishing machines. *Journal of the Socity of Glass Technology*, 11:214–256, 1927. Silicon Materials Science and Technology X.

[82] A. A. Renshaw. Modal decoupling of systems decribed by three linear operators. *Journal of Applied Mechanics*, 64:238 – 240, 1997.

[83] G. F. Roach. *Green's Functions*. Cambridge University Press, Cambridge, United Kingdom, 2nd edition, 1982.

[84] A. Ronen and S. Malkin. Wear mechanisms of statically loaded hydrodynamic bearings by contaminant abrasive particles. *Wear*, 68:371–389, 1981.

[85] F. S. Sherman. *Viscous Flow*. McGraw-Hill, 1990.

[86] T. Shibata, S. Fuji, E. Makino, and M. Ikeda. Ductile-regime turning mechanism of single-crystal silicon. *Precision Engineering*, 18:129–137, 1996.

[87] P. Singer. Is the industry ready for 450 mm wafers? *Semiconductor International*, 28(3):15, 2005.

[88] I. Stakgold. *Green's Functions and Boundary Value Problems*. Wiley, New York, 2nd edition, 1998.

[89] H. Suwabe, K.-I. Ishikawa, and A. Kitajima. A basic study on slurry actions and slicing characteristics of multi-wire saw. In *Proceedings of ASPE 16th Annual Meeting*, Crystal City, Virginia, November 10-15 2001. ASPE.

[90] C. A. Tan and C. D. Mote. Analysis of a hydrodynamic bearing under transverse vibration of an axially moving band. *Journal of Tribology, Transactions of the ASME*, 112:514–523, July 1990.

[91] C. A. Tan, B. Yang, and C. D. Mote. On the vibration of a translating string coupled to hydrodynamic bearings. *Journal of Vibration and Acoustics*, pages 337–345, 1990.

[92] C. A. Tan and S. Ying. Dynamic analysis of the axially moving string based on wave propagation. *Journal of Vibration and Acoustics*, pages 394–400, 1997.

[93] C. A. Tan and L. Zhang. Dynamic characteristics of a constrained string translating across an elastic foundation. *Journal of Vibration and Acoustics*, 116:318 – 325, 1994.

[94] J. A. Wickert V. Kartik. Vibration and guiding of moving media with edge weave imperfections. *Journal of Sound and Vibration*, 291:419 – 436, 2006.

[95] Y. Wang, X. Liu, and L. Huang. Eigenvalue and stability analysis for axially moving strings in transverse vibrations. In *2005 International Conference Physics and Control*, pages 194–201, Saint Petersburg, Russia, August 24-26 2005.

[96] M. Watanabe and S. Kramer. 450 mm silicon: An opportunity and wafer scaling. *Electrochemical Society Interface*, 15(4):28–31, 2006.

[97] S. Wei and I. Kao. Vibration analysis of wire and frequency response in the modern wiresaw manufacturing process. *Journal of Sound and Vibration*, 231(5):1383–1395, 2000.

[98] J. A. Wickert. Response solutions for the vibration of a traveling string on an elastic foundation. *Journal of Vibration and Acoustics*, 116:137 – 139, 1994.

[99] J. A. Wickert and C. D. Mote. Classical vibration analysis of axially moving continua. *ASME Journal of Applied Mechanics*, 57:738 – 744, 1990.

[100] J. A. Williams and A. M. Hyncica. Mechanisms of abrasive wear in lubricated contacts. *Wear*, 152:57–74, 1992.

[101] T. Yamada, M. Fukunaga, T. Ichikawa, K. Furno, K. Makino, and A. Yokoyama. Prediction of warping in silicon wafer slicing with wire saw. *Theoretical and Applied Mechanics*, 51:251–258, 2002.

[102] J. Yan, K. Syoji, T. Kuriyagawa, and H. Suzuki. Ductile regime turning at large tool feed. *Journal of Materials Processing Technology*, 121:363–372, 2002.

[103] B. Yang and C. D. Mote. Active vibration control of the axially moving string in the s domain. *Journal of Applied Mechanics, Transactions of the ASME*, 58:189 – 196, 1991.

[104] B. Yang and C. D. Mote. Frequency-domain vibration control of distributed gyroscopic systems. *journal of Dynamic Systems, Measurement, and Control, Transactions of the ASME*, 113(1):18–25, March 1991.

[105] B. Yang and C. D. Mote. On time delay in noncolocated control of flexible mechanical systems. *journal of Dynamic Systems, Measurement, and Control, Transactions of the ASME*, 114:409–415, September 1992.

[106] B. Yang and C. A. Tan. Transfer functions of one-dimensional distributed parameter systems. *Journal of Applied Mechanics*, 59:1009 – 1014, 1992.

[107] F. Yang and I. Kao. Free abrasive machining in slicing brittle materials with wiresaw. *Journal of Electronic Packaging*, 123:254–259, 2001.

[108] A. S. Yigit and A. P. Christoforou. Coupled axial and transverse vibrations of oilwell drillstrings. *Journal of Sound and Vibration*, 195(4):617 – 627, 1996.

[109] A. S. Yigit and A. P. Christoforou. Coupled torsional and bending vibrations of drillstrings subject to impact with friction. *Journal of Sound and Vibration*, 215(1):167 – 181, 1998.

[110] A. S. Yigit and A. P. Christoforou. The efficacy of the momentum balance method in transverse impact problems. *Journal of Vibration and Acoustics*, 120:47 – 53, 1998.

[111] L. Zhu and I. Kao. Galerkin-based modal analysis on the vibration of wire-slurry system in wafer slicing using wiresaw. *Journal of Sound and Vibration*, 283(3-5):589–620, May 2005.

[112] W. D. Zhu and Y. Chen. Forced response of translating media with variable length and tension: Application to high-speed elevators. *J. Multi-body Dynamics*, 219:35 – 53, 2005. Proc. IMechE Part K.

[113] W. D. Zhu and Y. Chen. Theoretical and experimental investigation of elevator cable dynamics and control. *Journal of Vibration and Acoustics*, 128:66 – 78, 2006.

Appendix A

Derivation of the Coefficients in Equations (2.46) and (2.47) in Free Vibration Response

As other distributed systems, the free vibration response can be obtained according to the orthogonality and initial conditions. Recall equation (2.27)

$$u(x,t) = \sum_{n=1}^{\infty} \left[D_{1n}\psi_{1n}(x)\mathrm{e}^{\lambda_{1n}t} + D_{2n}\psi_{2n}(x)\mathrm{e}^{\lambda_{2n}t} \right]$$

and the orthogonal relationship (2.42)

$$\left(\frac{\eta^2}{4} + \omega_n\omega_m\right) M_{mn} - \frac{\eta}{2}C_{mn} + K_{mn} = \delta_{mn}R \tag{A.1}$$

If the initial displacement of the wire is $a(x)$ and the initial velocity is $b(x)$, we have

$$u(x,0) = \sum_{n=1}^{\infty} \left[D_{1n}\psi_{1n}(x) + D_{2n}\psi_{2n}(x) \right] = a(x) \tag{A.2}$$

$$u_t(x,0) = \sum_{n=1}^{\infty} \left[D_{1n}\left(-\frac{\eta}{2} + \mathrm{i}\omega_{1n}\right)\psi_{1n}(x) + D_{2n}\left(-\frac{\eta}{2} + \mathrm{i}\omega_{2n}\right)\psi_{2n}(x) \right] = b(x) \tag{A.3}$$

Applying the differential operator K in equation (2.15) to equation (A.2), then multiplying by ψ_{1m}^* and integrating from 0 to 1, we can obtain

$$\sum_{n=1}^{\infty} \left[D_{1n}\int_0^1 \psi_{1m}^*\mathrm{K}\left[\psi_{1n}\right]dx + D_{2n}\int_0^1 \psi_{1m}^*\mathrm{K}\left[\psi_{2n}\right]dx \right] = \int_0^1 \psi_{1m}^*\mathrm{K}\left[a(x)\right]dx$$

which can be represented as

$$\sum_{n=1}^{\infty} \left[D_{1n}K_{1m1n} + D_{2n}K_{1m2n} \right] = \int_0^1 \psi_{1m}^*\mathrm{K}\left[a(x)\right]dx \tag{A.4}$$

The same representation can be obtained for differential operators M and C, as follows

$$\sum_{n=1}^{\infty}\left[D_{1n}M_{1m1n}+D_{2n}M_{1m2n}\right]=\int_0^1 \psi_{1m}^{*}\mathrm{M}\left[a(x)\right]dx \tag{A.5}$$

$$\sum_{n=1}^{\infty}\left[D_{1n}C_{1m1n}+D_{2n}C_{1m2n}\right]=\int_0^1 \psi_{1m}^{*}\mathrm{C}\left[a(x)\right]dx \tag{A.6}$$

Next, we apply differential operator M to equation (A.3), then multiply by ψ_{1m}^{*} and integrate from 0 to 1 to obtain

$$\sum_{n=1}^{\infty}\left[D_{1n}\left(-\frac{\eta}{2}+\mathrm{i}\omega_{1n}\right)M_{1m1n}+D_{2n}\left(-\frac{\eta}{2}+\mathrm{i}\omega_{2n}\right)M_{1m2n}\right]=\int_0^1 \psi_{1m}^{*}\mathrm{M}\left[b(x)\right]dx \tag{A.7}$$

Multiply equation (A.5) by $\frac{\eta}{2}$ and add to equation (A.7), and then premultiplied both sides of the equal sign by $(-\mathrm{i}\omega_{1m})$ to obtain

$$\begin{aligned}&\sum_{n=1}^{\infty}\left[D_{1n}\omega_{1m}\omega_{1n}M_{1m1n}+D_{2n}\omega_{1m}\omega_{2n}M_{1m2n}\right]\\&=-\mathrm{i}\omega_{1m}\left(\int_0^1 \psi_{1m}^{*}\mathrm{M}\left[b(x)\right]dx+\frac{\eta}{2}\int_0^1 \psi_{1m}^{*}\mathrm{M}\left[a(x)\right]dx\right)\end{aligned} \tag{A.8}$$

In order to solve for the coefficients, the above equations have to be reorganized to meet the orthogonal relationship (A.1). Therefore, we multiply equation (A.5) by $\frac{\eta^2}{4}$, multiply equation (A.6) by $-\frac{\eta}{2}$, and add them up with equations (A.4) and (A.8) to obtain

$$\begin{aligned}&\sum_{n=1}^{\infty}\Bigg\{D_{1n}\left[\left(\frac{\eta^2}{4}+\omega_{1m}\omega_{1n}\right)M_{1m1n}-\frac{\eta}{2}C_{1m1n}+K_{1m1n}\right]\\&\quad+D_{2n}\left[\left(\frac{\eta^2}{4}+\omega_{1m}\omega_{2n}\right)M_{1m2n}-\frac{\eta}{2}C_{1m2n}+K_{1m2n}\right]\Bigg\}\\&=\frac{\eta^2}{4}\int_0^1 \psi_{1m}^{*}\mathrm{M}\left[a(x)\right]dx-\mathrm{i}\omega_{1m}\left(\int_0^1 \psi_{1m}^{*}\mathrm{M}\left[b(x)\right]dx+\frac{\eta}{2}\int_0^1 \psi_{1m}^{*}\mathrm{M}\left[a(x)\right]dx\right)\\&\quad-\frac{\eta}{2}\int_0^1 \psi_{1m}^{*}\mathrm{C}\left[a(x)\right]dx+\int_0^1 \psi_{1m}^{*}\mathrm{K}\left[a(x)\right]dx\end{aligned} \tag{A.9}$$

Assume $1m=1n$. According to the orthogonal relationship (A.1), the coefficient D_{2n} will disappear because $1n\neq 2n$. The coefficient D_{1n} can be obtained as in equation

(2.46).

$$D_{1n} = \left(\frac{\eta^2}{4} \int_0^1 \psi_{1n}^* \mathrm{M}\left[a(x)\right] dx - \mathrm{i}\omega_{1n} \left(\int_0^1 \psi_{1n}^* \mathrm{M}\left[b(x)\right] dx + \frac{\eta}{2} \int_0^1 \psi_{1n}^* \mathrm{M}\left[a(x)\right] dx \right) \right. \\ \left. - \frac{\eta}{2} \int_0^1 \psi_{1n}^* \mathrm{C}\left[a(x)\right] dx + \int_0^1 \psi_{1n}^* \mathrm{K}\left[a(x)\right] dx \right) \Big/ R \tag{2.46}$$

where $R = n^2\pi^2 \left(1 - v^2\right) - \frac{\eta^2}{4}$ is defined in Section 2.4. The term D_{2n} can be solved using the same strategy,

$$D_{2n} = \left(\frac{\eta^2}{4} \int_0^1 \psi_{2n}^* \mathrm{M}\left[a(x)\right] dx - \mathrm{i}\omega_{2n} \left(\int_0^1 \psi_{2n}^* \mathrm{M}\left[b(x)\right] dx + \frac{\eta}{2} \int_0^1 \psi_{2n}^* \mathrm{M}\left[a(x)\right] dx \right) \right. \\ \left. - \frac{\eta}{2} \int_0^1 \psi_{2n}^* \mathrm{C}\left[a(x)\right] dx + \int_0^1 \psi_{2n}^* \mathrm{K}\left[a(x)\right] dx \right) \Big/ R \tag{2.47}$$

Appendix B

Closed-Form Solution of Equation (4.26)

in the following

Recall equation (4.26) in Section 4.3.

$$u(x,t) = -0.01\int_0^1 g_\tau(x,\xi,t,0)\sin\pi\xi d\xi + 0.01\int_0^1 g(x,\xi,t,0)\left(2v\pi\cos\pi\xi + \eta\sin\pi\xi\right)d\xi$$

The integral result of equation (4.26) is presented in this appendix as follows.

$$u(x,t) = \sum_{n=1}^{\infty} u_n(x,t) = \sum_{n=1}^{\infty} \frac{2n\pi^2(1-v^2)\mathrm{e}^{-\frac{\eta}{2}t}}{\omega_n}\frac{N_n}{D_n}$$

where

$$\begin{aligned} N_n \;=\; & \big[\left(\gamma_n\eta + \left(\gamma_n\eta\cos(\gamma_n) + 2\left(\pi^2 v - \pi^2 n^2 v + v\gamma_n^2 + \gamma_n\omega_n\right)\sin(\gamma_n)\right)\cos(n\pi)\right)\cos(\gamma_n x + \omega_n t) \\ & -\left(2\left(\pi^2 v - \pi^2 n^2 v + v\gamma_n^2 + \gamma_n\omega_n\right) + \left(2\left(\pi^2 v - \pi^2 n^2 v + v\gamma_n^2 + \gamma_n\omega_n\right)\cos(\gamma_n)\right.\right. \\ & \left.\left.-\gamma_n\eta\sin(\gamma_n)\right)\cos(n\pi)\right)\sin(\gamma_n x + \omega_n t)\big]\sin(n\pi x) \end{aligned}$$

and

$$D_n = \pi^4 - 2n^2\pi^4 + n^4\pi^4 - 2\pi^2\gamma_n^2 - 2n^2\pi^2\gamma_n^2 + \gamma_n^4$$

The symbol $\gamma_n = \frac{v\omega_n}{1-v^2}$, and ω_n is the frequency of vibration which is defined as

$$\omega_n = \frac{\sqrt{\left[4n^2\pi^2(1-v^2) - \eta^2\right](1-v^2)}}{2}$$

Appendix C

Nomenclature for Chapters 2, 3, and 4

$a(x)$	Initial displacement of the wire
A, B, D, E	Various coefficients in the derivation of vibration response
$b(x)$	Initial transverse velocity of the wire
C	Damping differential operator, $\mathrm{C} = \eta$
$\mathcal{D}$	Differential operator
$\mathcal{D}^*$	Adjoint differential operator corresponding to $\mathcal{D}$
f	Nondimensional external excitation
f_B	Standardizing function with respect to the boundary conditions
f_I	Standardizing function with respect to the initial conditions
F	Dimensional external excitation, which has the unit of $\mathrm{N\,m^{-1}}$
F_d	Damping force, the product of damping factor and velocity of the wire
$g(x, \xi, t, \tau)$	The Green's function
G	Gyroscopic differential operator, where $\mathrm{G} = 2v\frac{\partial}{\partial x}$
$G(x, \xi, s)$	Laplace transform of the Green's function
H	Circulatory differential operator, where $\mathrm{H} = \eta v\frac{\partial}{\partial x}$
K	Stiffness differential operator, where $\mathrm{K} = -(1 - v^2)\frac{\partial^2}{\partial x^2}$
L	The length of the wire, which has the unit of m
$\mathcal{L}$	Lapalce transform
$\mathcal{L}^{-1}$	Inverse Lapalce transform

M	Inertial differential operator, where $\mathrm{M} = I$
P	Tension of the wire, which has unit N
R	Value defined in equations (2.42), (2.43), and (2.44)
s	Damping index, defined in equation (3.2)
t	Nondimensional time
T	Time, which has the unit of s (second)
$u(x,t)$	Nondimensional response of free vibration of damped axially moving wire
$u_n(x,t)$	The nth component of response, $u(x,t)$
$U(X,T)$	Transverse displacement, also the response of free vibration of damped axially moving wire
v	Nondimensionalized axial speed of the wire
V	Dimensional axial speed of the wire, which has the unit of $\mathrm{m\,s^{-1}}$
x	Nondimensionalized horizontal axis
X	Horizontal axis
$Z(x,a,\omega)$	Frequency response with a point excitation at position a
ζ_ω	Damping ratio defined by the frequency of vibration
ζ_θ	Damping ratio defined by the complex eigenvalues
η	Nondimensionalized damping factor
η_d	Damping factor, which has the unit of $\mathrm{N\,s\,m^{-2}}$
λ_{1n}	Eigenvalues, which will be $\left(-\frac{\eta}{2} + i\omega_{1n}\right)$ when it is complex
λ_{2n}	Conjugate eigenvalues, which will be $\left(-\frac{\eta}{2} + i\omega_{2n}\right)$ when it is complex
ρ	The mass density per length of the wire, which has the unit of $\mathrm{kg\,m^{-1}}$
$\psi(x)$	Eigenfunction as defined in equations (2.16), (2.18), and (2.20)
$\psi_{1n}(x)$	Eigenfunctions corresponding to λ_{1n}
$\psi^*_{1n}(x)$	Adjoint eigenfunctions corresponding to $\psi_{1n}(x)$
$\psi_{2n}(x)$	Eigenfunctions corresponding to λ_{2n}
$\psi^*_{2n}(x)$	Adjoint eigenfunctions corresponding to $\psi_{2n}(x)$

$\bar{\psi}_m^*$	Complex conjugate of adjoint eigenfunction ψ_m^*
$\omega_{d,n}$	Frequency of damped vibration response corresponding to the nth component of response, $u_n(x,t)$
ω_{1n}	Frequency associated with λ_{1n}, equal to $\omega_{d,n}$
ω_{2n}	Frequency associated with λ_{2n}, equal to $-\omega_{d,n}$

Appendix D

Nomenclature for Chapter 5

R_s	Total surface roughness
R_s^{400}	Roughness due to F-600 particle distribution
R_s^{600}	Roughness due to F-400 particle distribution
χ	Weight percent ratio of F-400
ϕ	Particle diameter
p	Nominal pressure per particle
k	Concentration of particles in contact
k_{max}	Maximum particle concentration factor
E_r	Reduced modulus
$R_{s,limit}$	Geometric limit to roughness
$R_s^{400}\|_{limit}$	Penetration depth limit of F-400 particles
ϕ_{400}	Diameter of F-400 particles
ϕ_{600}	Diameter of F-600 particles
ϕ_{400}^{eff}	Effective diameter parameter of F-400 particles
ϕ_{600}^{eff}	Effective diameter parameter of F-600 particles
β	Shift in F-400 particle concentration
k_{400}	Concentration of the F-400 particles
k_{600}	Concentration of the F-600 particles
k^*	Critical concentration of F-600 particles in R_s^{400}

$\chi\|_{\%cr}$	Weight percent ratio of F-400 at a given particle percentage related to interaction effect
$\%cr$	Ratio of F-600 particles for $\phi_{600} > 15.8\ \mu m$ to the total number of particles in contact
α	Ratio of the number of critical F-600 particles which could be in contact
n	Percentage of load-bearing abrasive particles